NAVAL POSTGRADUATE SCHOOL
Monterey, California

DISSERTATION

NUMERICAL AND EXPERIMENTAL ANALYSIS OF THE PERFORMANCE OF STAGGERED SHORT PIN-FIN HEAT EXCHANGERS

by

Leonard J. Hamilton

June 2003

Dissertation Supervisor: Ashok Gopinath

Approved for public release; distribution is unlimited

THIS PAGE INTENTIONALLY LEFT BLANK

REPORT DOCUMENTATION PAGE			Form Approved OMB No. 0704-0188
Public reporting burden for this collection of information is estimated to average 1 hour per response, including the time for reviewing instruction, searching existing data sources, gathering and maintaining the data needed, and completing and reviewing the collection of information. Send comments regarding this burden estimate or any other aspect of this collection of information, including suggestions for reducing this burden, to Washington headquarters Services, Directorate for Information Operations and Reports, 1215 Jefferson Davis Highway, Suite 1204, Arlington, VA 22202-4302, and to the Office of Management and Budget, Paperwork Reduction Project (0704-0188) Washington DC 20503.			
1. AGENCY USE ONLY *(Leave blank)*	**2. REPORT DATE** June 2003	**3. REPORT TYPE AND DATES COVERED** Dissertation	
4. TITLE AND SUBTITLE: Numerical and Experimental Analysis of the Performance of Staggered Short Pin-Fin Heat Exchangers			**5. FUNDING NUMBERS**
6. AUTHOR(S) CDR Leonard J. Hamilton, USN			
7. PERFORMING ORGANIZATION NAME(S) AND ADDRESS(ES) Naval Postgraduate School Monterey, CA 93943-5000			**8. PERFORMING ORGANIZATION REPORT NUMBER**
9. SPONSORING / MONITORING AGENCY NAME(S) AND ADDRESS(ES) N/A			**10. SPONSORING / MONITORING AGENCY REPORT NUMBER**
11. SUPPLEMENTARY NOTES The views expressed in this thesis are those of the author and do not reflect the official policy or position of the Department of Defense or the U.S. Government.			
12a. DISTRIBUTION / AVAILABILITY STATEMENT **Approved for public release; distribution is unlimited**			**12b. DISTRIBUTION CODE**

13. ABSTRACT ***(maximum 200 words)***

A three dimensional finite element based numerical model was used to analyze the heat transfer characteristics of various staggered short pin-fin array heat exchangers. The simulation was validated against data from an experimental rig as well as historical data and then used to estimate the heat transfer coefficient and pressure drop for a wide range of Reynolds numbers for circular and airfoil-shaped pin fins. Circular pin configuration variations included changes in pin spacing, axial pitch and pin height ratio. Airfoil pin variations also included changes in length and aspect ratio. Correlations for Nusselt number and friction factor were developed. Using established performance metrics, optimum configurations for both pin shapes were determined. The optimum airfoil pin array was shown to match the heat transfer rates obtained by the optimum circular pin configuration while incurring less than one third the specific fluid friction power loss. The results from this study would be of direct value in the design of a shroud enclosed heat exchanger concept being proposed for turbine blade cooling, or for cooling of high power electronic components, or in other high heat flux dissipation applications requiring a low-profile, high area-density based micro-heat exchanger design.

14. SUBJECT TERMS Numerical Analysis, Heat Transfer, Pin-fin Heat Exchanger, Turbine Blade Cooling, Electronic Component Cooling			**15. NUMBER OF PAGES** 187
			16. PRICE CODE
17. SECURITY CLASSIFICATION OF REPORT Unclassified	**18. SECURITY CLASSIFICATION OF THIS PAGE** Unclassified	**19. SECURITY CLASSIFICATION OF ABSTRACT** Unclassified	**20. LIMITATION OF ABSTRACT** UL

NSN 7540-01-280-5500 Standard Form 298 (Rev. 2-89)
Prescribed by ANSI Std. 239-18

THIS PAGE INTENTIONALLY LEFT BLANK

Approved for public release; distribution is unlimited

NUMERICAL AND EXPERIMENTAL ANALYSIS OF THE PERFORMANCE OF STAGGERED SHORT PIN-FIN HEAT EXCHANGERS

Leonard J. Hamilton
Commander, United States Navy
B.S., United States Naval Academy, 1984
M.S., University of Maryland, College Park, 1984

Submitted in partial fulfillment of the
requirements for the degree of

DOCTOR OF PHILOSOPHY IN MECHANICAL ENGINEERING

from the

NAVAL POSTGRADUATE SCHOOL
June 2003

Author: _____
Leonard J. Hamilton

Approved by:

_____	_____
Ashok Gopinath Associate Professor of Mechanical Engineering Dissertation Supervisor	Garth Hobson Professor of Aeronautics and Astronautics
_____	_____
Terry McNelley Professor of Mechanical Engineering	Knox Millsaps Professor of Mechanical Engineering
_____	
Raymond Shreeve Professor of Aeronautics and Astronautics	

Approved by: _____
Young W. Kwon, Chairman, Department of Mechanical Engineering

Approved by: _____
Carson K. Eoyang, Associate Provost for Academic Affairs

THIS PAGE INTENTIONALLY LEFT BLANK

ABSTRACT

A three dimensional finite element based numerical model was used to analyze the heat transfer characteristics of various staggered short pin-fin array heat exchangers. The simulation was validated against data from an experimental rig as well as historical data and then used to estimate the heat transfer coefficient and pressure drop for a wide range of Reynolds numbers for circular and airfoil-shaped pin fins. Circular pin configuration variations included changes in pin spacing, axial pitch and pin height ratio. Airfoil pin variations also included changes in length and aspect ratio. Correlations for Nusselt number and friction factor were developed. Using established performance metrics, optimum configurations for both pin shapes were determined. The optimum airfoil pin array was shown to match the heat transfer rates obtained by the optimum circular pin configuration while incurring less than one third the specific fluid friction power loss. The results from this study would be of direct value in the design of a shroud enclosed heat exchanger concept being proposed for turbine blade cooling, or for cooling of high power electronic components, or in other high heat flux dissipation applications requiring a low-profile, high area-density based micro-heat exchanger design.

THIS PAGE INTENTIONALLY LEFT BLANK

TABLE OF CONTENTS

THIS PAGE INTENTIONALLY LEFT BLANK

LIST OF FIGURES

LIST OF TABLES

THIS PAGE INTENTIONALLY LEFT BLANK

NOMENCLATURE

A	area [m^2]
$\overline{A}$	average array flow area [m^2]
A_f	friction factor correlation amplification factor
A_N	Nusselt number correlation amplification factor
AR	Airfoil aspect ratio, D_x / D_y
B	friction factor correlation variable
C_N	Nusselt number power function correlation coefficient
C_F	Friction factor power function correlation coefficient
Cp	specific heat capacity [J/kgK]
D	pin-fin diameter [m]
D_h	hydraulic diameter [m]
D_X	Airfoil-shaped pin major diameter [m]
D_Y	Airfoil-shaped pin minor diameter [m]
E	fluid friction power per unit area [W/m^2]
f	friction factor
h	heat transfer coefficient [W/m^2K]
H	pin height [m]
k	thermal conductivity [W/mK]
Kn	Knudsen number, λ / D_h
k_t	turbulent kinetic energy [m^2/s^2]
L	array length [m]
LR	airfoil length ratio, D_X / X
m	Nusselt number power function correlation exponent
$\dot{m}$	mass flow rate [kg/s]
Ma	mach number

n	Friction factor power function correlation exponent
N	number of pin-fin rows
Nu	Nusselt number
P	pressure [Pa]
Q	heat transfer rate [W]
Re	Reynolds number
S	spanwise spacing between pin centers [m]
T	temperature [K]
ΔT_{lm}	log mean temperature difference [K]
U	flow velocity [m/s]
V	volume [m^3]
$\dot{\forall}$	Volumetric flow rate [m^3/s]
w	measurement uncertainty
x	streamwise coordinate direction
X	streamwise spacing between centers [m]
y	spanwise coordinate direction
z	pin axis coordinate direction
α	Heat transfer area density (cm^2/cm^3)
ε	turbulence dissipation rate [m^2/s^3]
λ	mean free path [m]
ρ	density [kg/m^3]
μ	dynamic viscosity [Pa s]

ACKNOWLEDGMENTS

Throughout the course of this research, there have been several people who deserve special mention and my heartfelt appreciation. First, I would like to thank my advisor, Professor Ashok Gopinath, for his guidance during this project. His insight and forward thinking were instrumental in ensuring that my research stayed on the right track. I especially thank him for encouraging me to present various conference papers generated during the course of this study. I would also like to thank Professors Hobson, McNelley, Millsaps, and Shreeve for their time and willingness to serve on my committee. Special thanks go to U.S. Navy Lieutenants Derek Adametz and Eric Lind who participated in the early stages of development of the numerical model and to Lieutenant David Ramthun, USN who was instrumental in designing and assembling the experimental test rig.

This research would not have been possible without generous funding from the Naval Air Systems Command and the Space and Naval Warfare Systems Center. Another source of critical resources was the Naval Postgraduate School Department of Mechanical Engineering computer lab. To these organizations I am truly grateful.

Finally, and most importantly, I would like to thank my beautiful wife and four wonderful children who supported me all the way. Their love, understanding and words of encouragement provided me with confidence and motivation. Without their help, none of this would have been possible. It is in this spirit of gratitude that I dedicate this work to them.

THIS PAGE INTENTIONALLY LEFT BLANK

EXECUTIVE SUMMARY

Motivated by the growing trend towards the development of miniaturized heat exchangers for large heat flux applications, a comprehensive study was carried out of the flow and heat transfer characteristics of staggered pin-fin array heat exchangers of various configurations. The primary thrust of this work was based on a fully three dimensional finite element based numerical model of the heat exchangers. The critical length scale of the heat exchanger that allows scaled up versions of the problem to be studied was identified and verified. For a limited set of configurations, the numerical data were validated against experimental data obtained from a modular rig that was designed to cover various scenarios. These data were used to predict the heat transfer coefficient and pressure drop for a wide range of Reynolds numbers for circular and airfoil shaped fins. Circular pin configuration variations included changes in pin spacing, axial pitch and pin height ratio. Airfoil pin variations also included changes in length and aspect ratio. Working correlations for Nusselt number and friction factor were developed. Using established performance metrics, optimum configurations for both pin shapes were determined. The optimum airfoil pin array was shown to match the heat transfer rates obtained by the optimum circular pin configuration while incurring less than one third the specific fluid friction power loss. The results from this study would be of direct value in the design of a shroud enclosed heat exchanger concept being proposed for turbine blade cooling, or for cooling of high power electronic components, or in other high heat flux dissipation applications requiring a low-profile, high area-density based micro-heat exchanger design.

THIS PAGE INTENTIONALLY LEFT BLANK

I. INTRODUCTION

A. BACKGROUND/MOTIVATION

Historically, short pin-fin arrays have played an important role in enhancing heat dissipation, particularly for turbine blade cooling. Their ability to dissipate heat effectively has enabled blade designers to meet the rigorous demands for higher turbine inlet temperatures. The requirement for increased specific thrust from future engine designs will serve to demand even more performance from any turbine blade cooling scheme.

Commonly, pin-fin arrays are made up of banks of solid pins that span the end walls of an internal flow passage or duct. The array is usually configured with cylindrical pins in either a staggered or in-line arrangement with the coolant flowing perpendicular to the pin axes. Typical array dimensions are pin diameter (*D*), pin height (*H*), streamwise pin spacing (*X*) and spanwise pin spacing (*S*) as shown in Figure 1. Pins can either be long with *H/D* greater than about 10, or short with *H/D* on the order of unity. Turbine blade cooling arrays fall into the latter category and form the subject of this study.

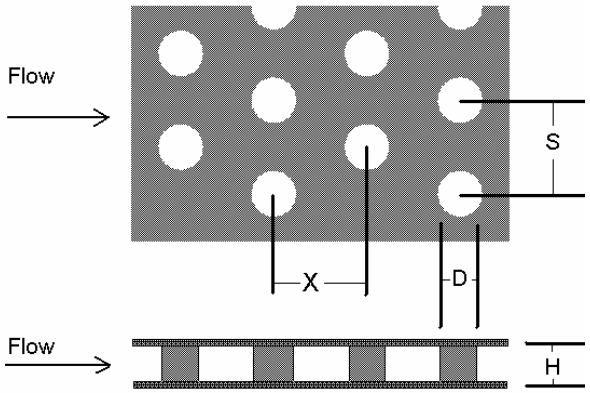

Figure 1 Schematic of a staggered pin-fin array

Currently turbine blade designers employ these pin-fin arrays mainly in the trailing edge of the blade as shown in Figure 2. Due to manufacturing constraints, ribbed channels and impingement cooling cannot be accommodated in these narrow regions (Ref. 1). One proposed concept for enhanced turbine blade cooling involves mounting microscale pin fin arrays on the blade surface and covering them with a thin metal skin.

Cooling air would circulate from within the blade, through these shrouded arrays and exit at various points for film-cooling as shown in Figure 3.

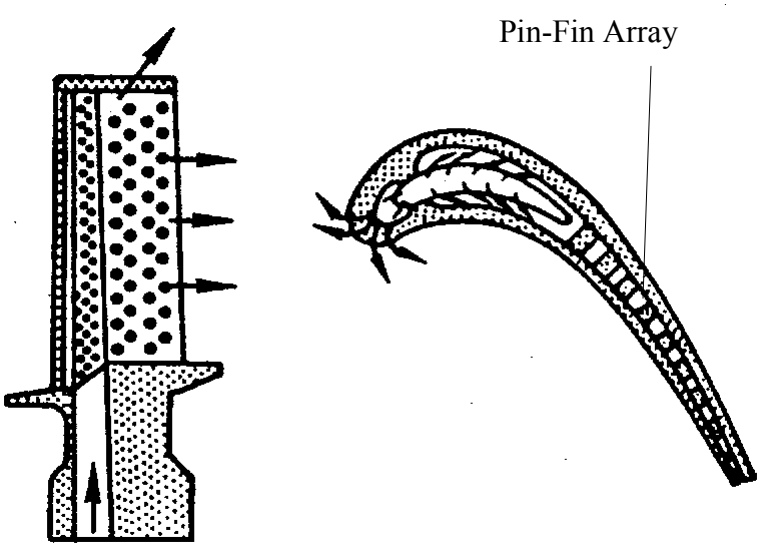

Figure 2 Typical application in a turbine blade

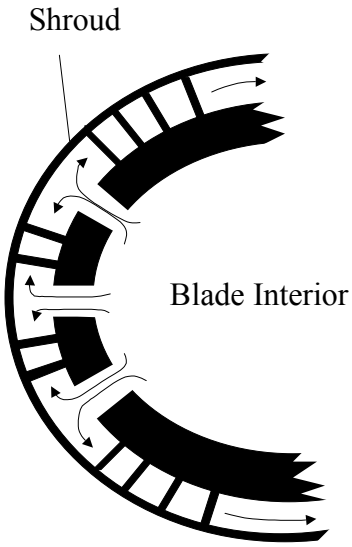

Figure 3 Proposed blade shroud configuration

Alternatively, these pin fin arrays could be used to cool integrated circuit chips in electronic equipment. These components could be mounted directly on top of a microscale pin-fin array cooled by forced convection. An economical electro-deposition process for manufacturing microscale pin fin heat exchanger arrays is described in by Stephens et al. (Ref. 2)

B. PREVIOUS WORK

Because of the critical function pin-fin arrays serve, empirical studies dating back to the 1980s have been carried out to determine and improve the effectiveness of such heat exchangers. VanFossen (Ref. 3) examined staggered pin-fin array configurations for *H/D* values of 0.5 and 2.0. He found that the presence of the pins significantly enhanced the array averaged heat transfer coefficient. He also noted that existing long pin correlations overestimated the short pin heat transfer coefficients, and thus established the need for further research. Sparrow et al. (Ref. 4) later confirmed this finding by studying the heat transfer properties for cylinders adjacent to endwalls. They discovered that wall-cylinder interactions were confined to one pin diameter from the wall and decreased heat transfer compared to regions of the cylinder away from the wall.

Taking the study further, Metzger, et al. (Ref. 5), examined the streamwise row-by-row development of the heat transfer coefficient for a staggered array. Using a 10-row array with H/D = 1.0, S/D = 2.5 and X/D = 1.5 and 2.5, they found that the heat transfer coefficient peaked between the third and fifth row of the array. Their work established a useful baseline empirical model used to validate future experimental results such as in the work of Chyu (Ref. 6), Chyu & Goldstein (Ref. 7), and Li et al. (Ref. 8).

Jubran, et al. (Ref. 9) also experimentally investigated the optimal pin-fin spacing that would provide the maximum heat transfer rate per unit area. Their results showed the optimum *X/D* and *S/D* values to be 2.5 for all flow rates tested. However, they used a fixed size endwall that meant various pin spacing configurations resulted in different numbers of pins. This aspect of their work presents a difficulty in comparing their results with other studies such as the work of Metzger, et al. (Ref. 5). In addition, *H/D* was approximately 9.5, and thus more representative of a long pin array.

Other experimental studies have focused on alternative pin shapes in an effort to improve heat exchanger performance. In 1983, Metzger et al. (Ref. 10) studied heat transfer and pressure drop for oblong pin-fins oriented with the major axis parallel to the flow direction. They found that both pressure drop and heat transfer rates were lower than they were for circular pin-fin arrays. Following this, Arora et al. (Ref. 11), studied similar oblong configurations with the major axis aligned at various angles of attack relative to the flow direction. Arora found that pressure drop was lower and heat transfer rates were as good or better for the oblong pins than circular pins when the major axis was aligned with the flow. For other angles of attack, the oblong pins offered no advantage over the circular pins. Later, Chen et al. (Ref. 12) and Li et al. (Ref. 8) studied drop-shaped and elliptical pin fin arrays respectively. They concluded that these alternate shapes provided better heat transfer rates and approximately half of the friction factor of the circular pin-fin arrays.

The relative contribution to overall heat transfer from the pins and the endwalls has been an issue of considerable debate, and has been discussed in several earlier studies. VanFossen (Ref. 3) first reported that the pin surface heat transfer coefficient was 35 percent greater than that of the endwall. Metzger, et al. (Ref. 10) determined that both were within 10 percent of each other, and then later reported that the pin surfaces had approximately 50% higher heat transfer coefficient than the endwall. Contradicting all previous results, Al Dabagh, et al. (Ref. 13) indicated that the endwall heat transfer coefficient was 15 to 35 percent higher than that for the pin fins. Offering a solution, Chyu, et al. (Ref. 14) determined that the heat transfer coefficient on the pin surface was 10 to 20 percent higher than the uncovered endwall.

Because experimental work can be expensive and time consuming, not all configurations of interest have been tested. With the current availability of tremendous computing resources and several powerful commercially available computational fluid dynamics software packages, the next logical step was to conduct these studies numerically. Recognizing the potential advantages afforded by numerical modeling for pre-design evaluation, Shah et al. (Ref. 15) have made a compelling case for the

imperative need for comprehensive computer-based studies of compact heat exchanger behavior and performance prior to empirical characterization and manufacture.

Donahoo, et al. (Ref. 16) approached this study as a numerical optimization problem using a general-purpose viscous flow solver to simulate the heat transfer and flow features within a staggered pin-fin array. A 2-D model was constructed and meshed to capture the tumultuous flow characteristics around the pins and in the wall regions of the internal flow passages of the heat exchanger. This study has provided some insight into the flow and heat transfer characteristics, however due to, the 2-D nature of the model it cannot be used to treat the effects of the bounding endwalls and hence the role of flow passage height cannot be incorporated into the characterization.

C. OBJECTIVES

After an extensive literature search, it was evident that the staggered short pin-fin heat exchanger had not been simulated with a three dimensional numerical model. The major goal of this research was to develop an experimentally validated three dimensional numerical model of the staggered short pin-fin heat exchanger. This model would then be used to accomplish the following objectives:

1. To quantify the heat transfer characteristics and pressure drop of several staggered short pin-fin array heat exchanger configurations.

2. To develop simple and reliable pin-fin heat exchanger performance correlations for various circular pin configurations and sizes. Demonstrating that these correlations are independent of heat exchanger size would be critical for extending them to microscale heat exchangers.

3. To perform a parametric study of an airfoil-shaped pin fin heat exchanger.

4. To determine optimal pin-fin array configurations based on suitably defined measures of heat exchanger effectiveness.

D. METHODOLOGY

The basic steps involved constructing a suitable numerical model, validating the model with experimental results and finally applying the model to a carefully defined test matrix. The following sections detail this process.

II. NUMERICAL ANALYSIS

In this section, the numerical portion of the heat exchanger study is presented.

A. CIRCULAR PIN BASELINE STUDY

This first subsection provides a detailed numerical analysis of the circular pin-fin array with $H/D = 1$.

1. Numerical Simulation

a. Modeling

The numerical modeling was performed using the FLOTRAN solver of the commercial finite element analysis package ANSYS (version 6.0). This code was selected with the expectation that periodic unsteadiness would be confined by relatively tight physical bounds and would not significantly affect the total time averaged flow solution. Based on later observation of the steady reduction in numerical residual values and steadiness in experimental data, this assumption was considered to be justified. This study examined turbulent flow and heat transfer characteristics within a planar 3-D staggered short pin-fin array heat exchanger.

In order to reduce computational requirements, some simplifying assumptions were made. First, by taking advantage of the symmetry planes, only one quarter of the heat exchanger was modeled as shown in Figure 4. Further, only the fluid (air) flow and heat transfer behavior were modeled thereby eliminating the need to model the solid regions of the heat exchanger (pins and end wall) and calculate their temperature distributions. This approach assumes that the heat exchanger surfaces could be treated as isothermal. Given that the pins are relatively short and metallic, a simple pin-fin analysis was carried out to validate this assumption. Calculations justifying this decision are shown in Appendix A. Therefore a conjugate analysis has not been implemented at this stage, and the passage walls and pin-fins were modeled as solid isothermal boundaries.

Two basic models were created in this study. The first model, shown in Figure 4 simulated a staggered array consisting of 10 rows of pins in the streamwise direction, and alternating between 4 and 5 pins per row in the spanwise direction. This represented a heat exchanger of finite width similar to the arrays tested by Metzger et al. (Ref. 5) and was used primarily for validation runs. The second model also simulated a staggered pin array with 10 rows of pins, but infinitely wide in spanwise extent. In this

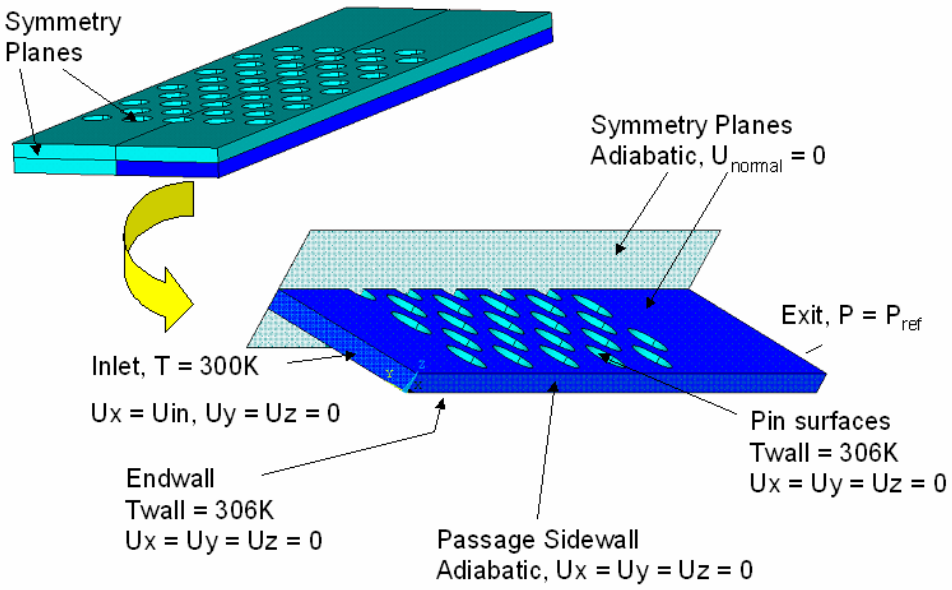

Figure 4 Numerical model details

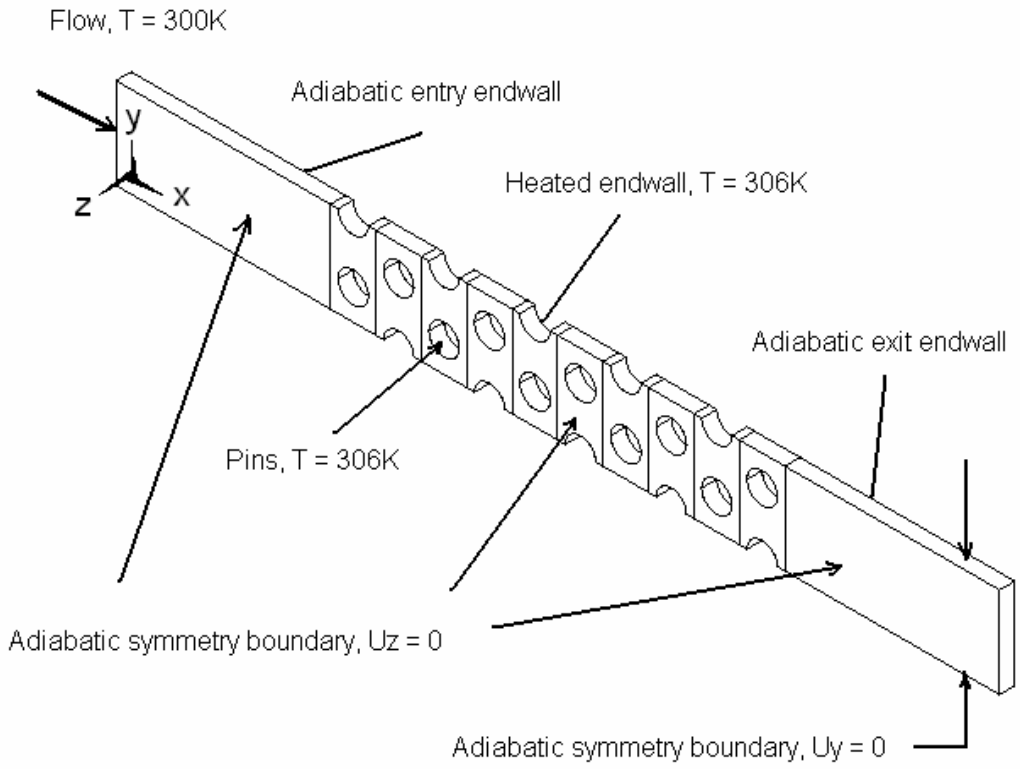

Figure 5 Infinite width numerical model

case, one half of an infinitely wide array was simulated. This infinite span condition was numerically achieved by placing "symmetry", i.e. zero flux boundaries on both the spanwise edges of the array as shown in Figure 5. This was done to simulate the behavior in microscale heat exchangers of ultimate interest, which typically have large feature densities consisting of many tens of pins per row whereby contributions from the sidewalls would make up but a very small fraction of the total flow solution. Both the finite and infinite models were used to complete the chosen test matrix. Figure 6 shows results for a representative configuration that was simulated with both models. It is clear that both models produced nearly identical results for Nusselt number and close results for friction factor and the implications will be discussed in more detail below. Friction factor for arrays with more than 5 pins in the spanwise direction would fall between the limits shown in this graph and are also well within the accuracy limits for the friction factor correlation developed in this study.

For consistency and efficiency, each numerical simulation was performed by executing a macro. Desired test configurations such as Reynolds number, axial pitch, pins spacing, height ratio, cooling air and wall temperature were specified as inputs to the macro. In addition to building the model, the macro was used to control mesh density and boundary conditions. Further details on the macro and a sample macro are provided in Appendix B.

To be consistent with earlier studies the heat exchanger array test section was placed between constant area adiabatic entrance and exit duct sections (see Figure 5). As in Metzger's experiments (Ref. 5), the entrance duct measured 12.7 cm in streamwise length. However, while Metzger used a 7.62 cm exit duct, the model exit duct in this study was extended to 12.5 cm, or 25 hydraulic diameters, to ensure well mixed conditions at the exit plane for reliable extraction of numerical data. All heated endwall and pin surfaces were maintained at a specified temperature. Inlet air velocity and temperature were specified to produce the desired Reynolds numbers, and the no-slip condition was observed on all rigid boundaries. Velocities and heat fluxes normal to symmetry boundaries were set to zero.

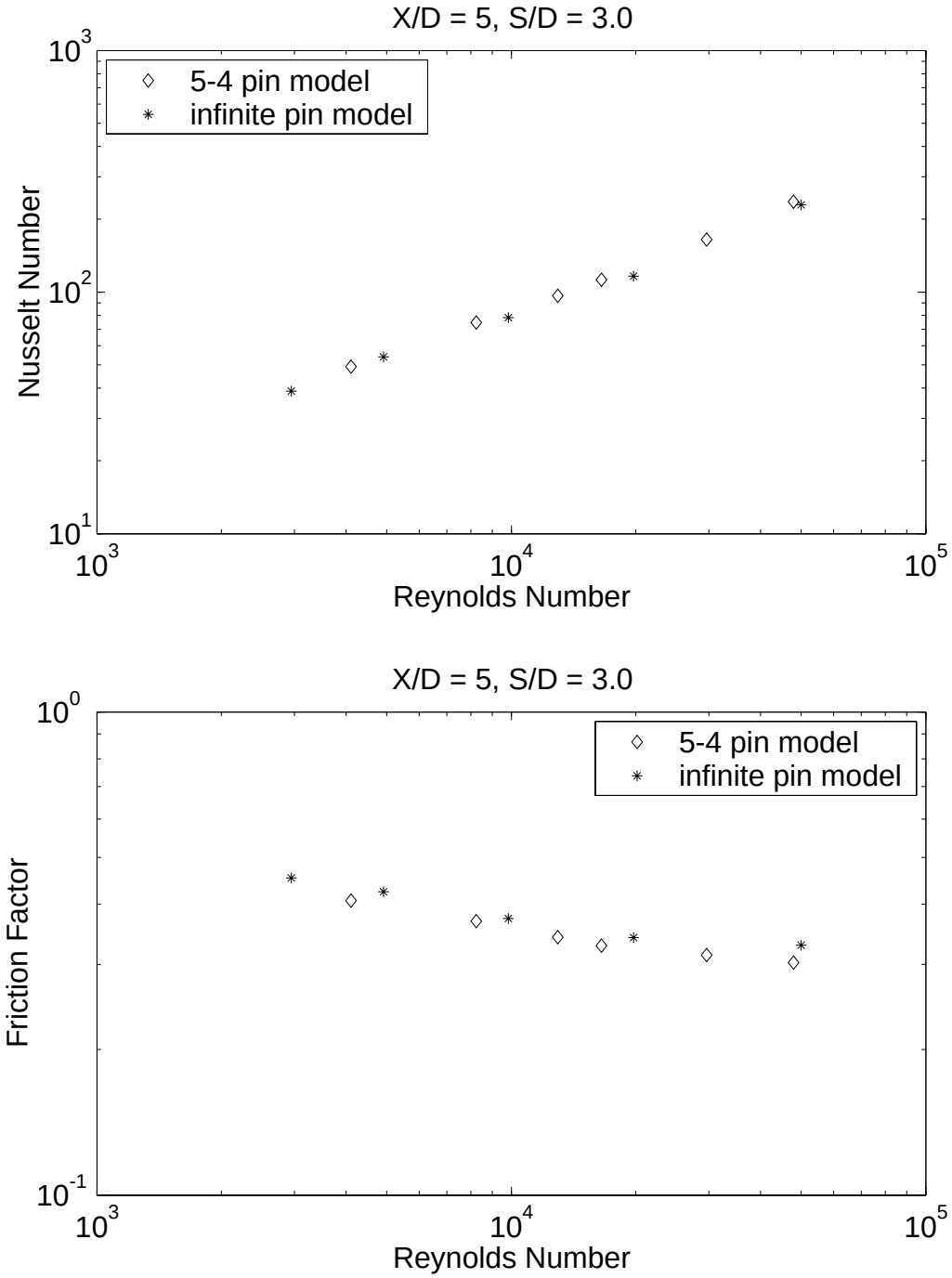

Figure 6 Comparison of results from finite and infinite models

b. Solution Technique and Numerical Accuracy

All models were solved using a standardized set of criteria. Each model was solved using the standard k_t-ε turbulence model with Van Driest coupling for the wall region. Additionally, all flows were treated as being incompressible and at steady state. The CFD FLOTRAN solver in ANSYS was set to use the Preconditioned Generalized Minimum Residual (PGMR) method and the Collocated-Galerkin (COLG) approach was used to discretize the advection term. More information on these CFD algorithms can be found in Appendix C or in the ANSYS Theory Manual (Ref. 17).

Initially, attempts were made to discretize the advection term using the Streamline Upwind/Petro-Galerkin (SUPG) approach in order to reduce solution time. However, solution analysis revealed that this method although quicker, produced an unreliable and oscillatory heat transfer rate solution. Figure 7 depicts the behavior of these two solution approaches applied to a typical problem. In this particular case, the goal of the task was to replicate the experimental study by Metzger et al. (Ref. 5) in order to validate the numerical model. The COLG method yielded a heat transfer rate of 3.41 watts, while 3.42 watts would have been required to match the results of Metzger. The SUPG method appeared to provide a less stable answer, while the COLG method yielded stable results that matched experimental results within 0.3%.

c. Grid Independence

Meshing was carefully specified to ensure maximum coverage in areas of interest such as regions of increased velocity and temperature gradient near the walls as shown in Figure 8. Additionally, mesh density was meticulously scaled to facilitate grid independence studies. Grid independence was taken to be achieved when the heat transfer results could be treated as effectively invariant, i.e. when changes in the overall heat transfer rate remained below 2% for subsequent change/refinement in the grid. Table 1 provides a representative example of a grid independence check for a given configuration. Finally a solution was considered valid only if the heat exchanger fluid outlet temperature prediction from the numerical model, matched the temperature prediction made from a simple energy balance to within 0.1K (<2%).

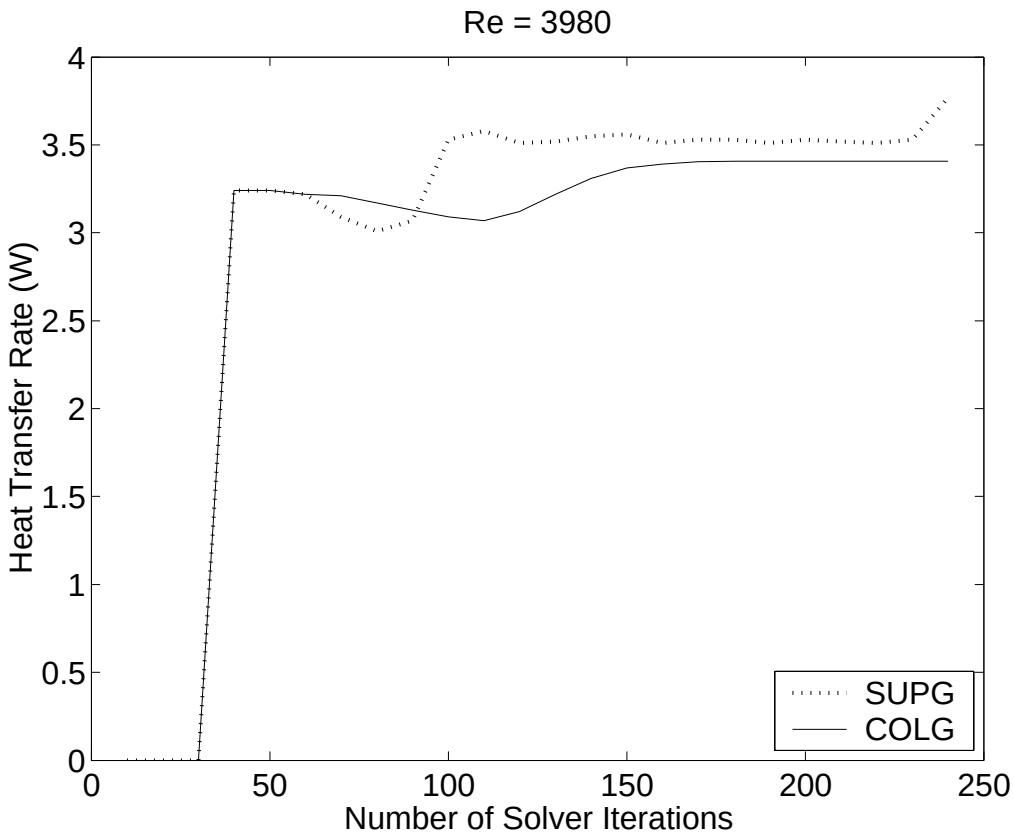

Figure 7 Comparison of advection discretization schemes

Table 1 Grid independence, $X/D = S/D = 3.0$, $Re_{Dh} = 5{,}000$

Parameter	Grid 1	Grid 2	Grid 3
x x y x z /pin[a]	200x20x9 /27	220x22x12 /29	230x23x15 /31
nodes	83,760	123,851	170,928
Q (W)	1.8163	1.9065	1.9076
T_{out} (K)	303.87	304.02	304.01
$\dot{m}$ (kg/s)	4.70E-04	4.72E-04	4.73E-04

[a]Indicates grid divisions along test section in x, y and z directions and along pin edges

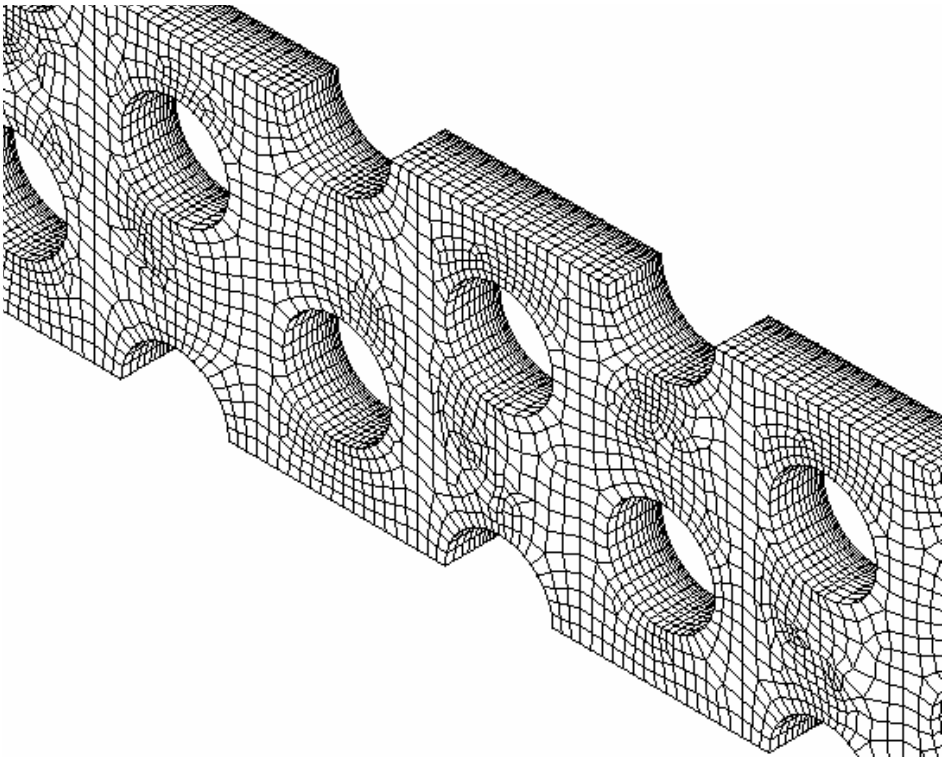

Figure 8 Sample model meshing

2. Test Approach

a. Model Validation

In order to validate the model, several runs were made in an attempt to reproduce the experimental results obtained by Metzger et al. (Ref. 5) and Arora (Ref. 11). Table 2 shows the configurations and conditions used for validation. The final column shows the temperature difference between the prescribed isothermal wall and pin heat exchanger surfaces, and the incoming air at 300K.

For validation, the Reynolds number was defined based on pin diameter, and the maximum geometry-based velocity as follows (originally used by Metzger):

$$\mathrm{Re}_D = \frac{\rho U_{\max} D}{\mu} \qquad (1)$$

where

$$U_{\max} = \frac{U_{in}\left(S/D\right)}{\left(S/D\right)-1} \qquad (2)$$

Table 2 Validation configurations

Config	*S/D*	*X/D*	*H/D*	*Re*	*ΔT(K)*
Metzger 1	2.5	1.5	1.0	3980, 7310, 13800, 20000, 30000, 41500, 69100, 98900	6,12
Metzger 2	2.5	2.5	1.0	3590, 7340, 13900, 24900 37900, 62100, 93500	6,12
Arora 1	2.22	2.83	1.07	6500,13827,24000	6
Arora 2	2.42	2.83	1.07	4200,13092,23000	6
Arora 3	2.46	3.39	1.28	4800,11012,29000	6

The graphs in Figure 9 through Figure 12 show the results from these validation runs plotted and compared with the data and correlations derived from the experiments of Metzger and Arora. Here, the Nusselt number and friction factor are defined as:

$$Nu_D = \frac{hD}{k} \qquad (3)$$

and

$$f = \frac{\Delta P}{2\rho U_{\max}^2 N} \qquad (4)$$

where N is the number of pin-fin rows in the streamwise direction. In the experiments conducted by Arora, N was replaced with array length.

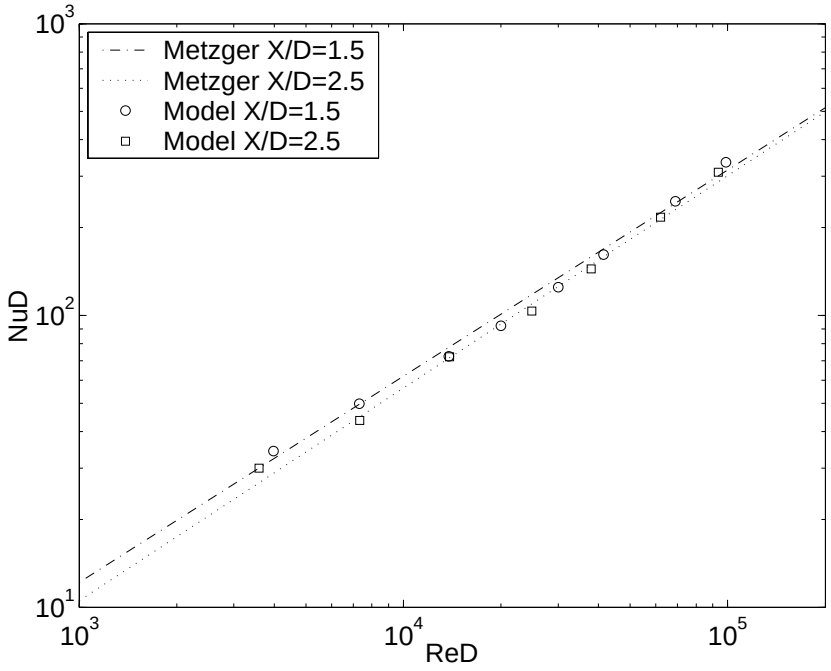

Figure 9 Comparison of numerically obtained Nusselt number with experimental data of Metzger (After Ref. 5)

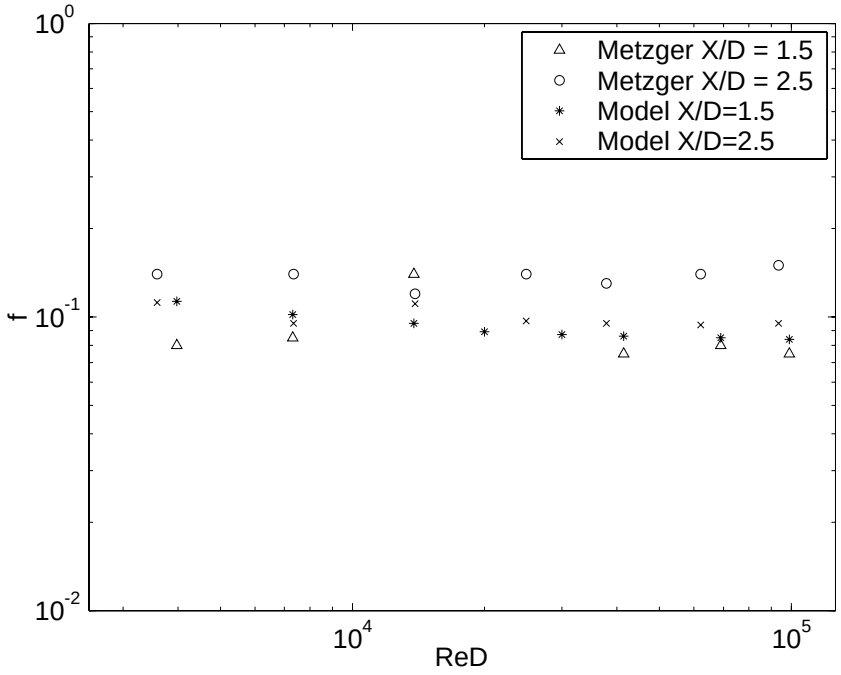

Figure 10 Comparison of numerically obtained friction factor with experimental data of Metzger (After Ref. 5)

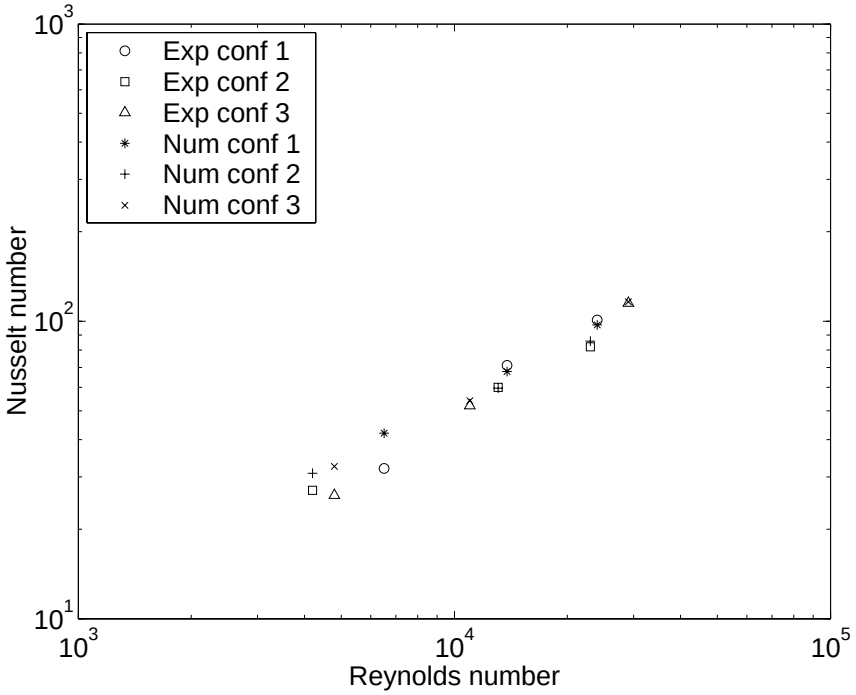

Figure 11 Comparison of numerically obtained Nusselt number with experimental data of Arora (After Ref. 11)

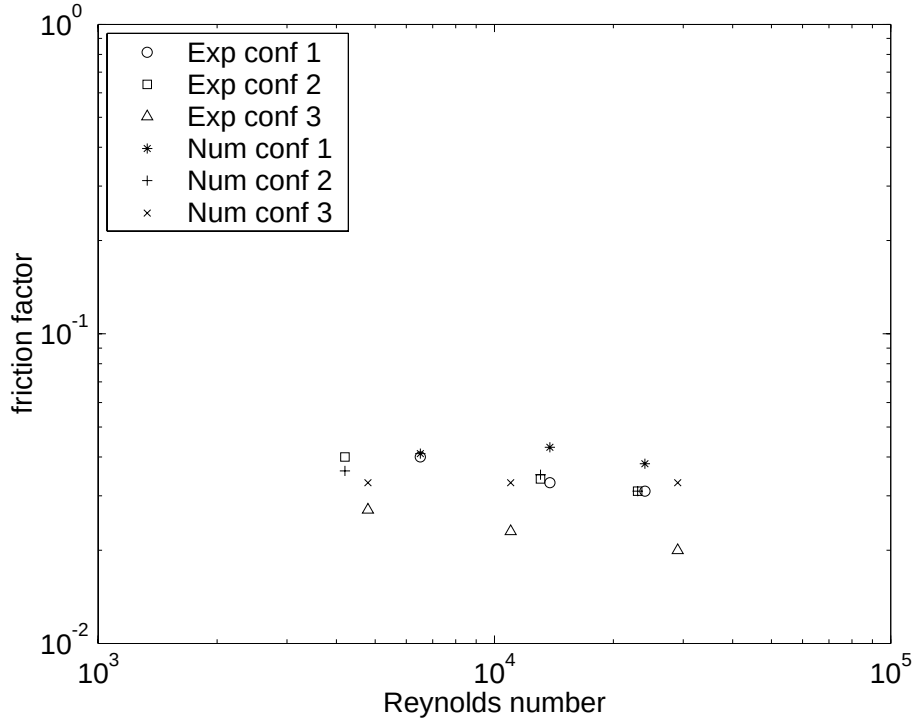

Figure 12 Comparison of numerically obtained friction factor with experimental data of Arora (After Ref. 11)

From these charts it can be seen that the numerical model has predicted Nusselt number very well. Table 3 shows a comparison between the correlations developed by Metzger et al. (Ref. 5) and correlations developed using the numerical model during validation.

Table 3 Validation results

X/D	Metzger experimental	ANSYS Model
1.5	$Nu_D = 0.069\,\mathrm{Re}_D^{0.728}$	$Nu_D = 0.075\,\mathrm{Re}_D^{0.721}$
2.5	$Nu_D = 0.092\,\mathrm{Re}_D^{0.707}$	$Nu_D = 0.090\,\mathrm{Re}_D^{0.707}$

The corroboration with Nusselt number results from Arora is also quite good especially for the higher Reynolds number cases. However, the numerically predicted friction factor results do not provide the same level of consistency. Compared to Metzger's data, the numerical model seems to fall in between the two configurations tested. When compared to Arora's data, the numerical model agrees extremely well with the experimental configuration 2 but tends to overestimate friction factor for configurations 1 and 3. Despite these differences noted, the model was considered useful as it displayed relative trends in friction factor between configurations to the same degree as the experiment.

Based on the comparisons between the numerical results and existing experimental data, the model was considered validated for Nusselt number predictions for Reynolds numbers between 3,500 and 100,000. The model was considered useful but moderately conservative for predicting friction factors over the same range.

b. Array Characteristic Length

For validation, pin diameter was chosen as the characteristic length in order to corroborate experimental results. However, with further numerical runs it became evident that the pin diameter was not truly representative of the characteristic length scale in the convoluted array flow passages for all the test configurations being considered in this study since it failed to account for array differences due to variations in *X/D*. Thus a more suitable characteristic length based on the ratio of open volume (V_{open})

available for fluid flow in the array, to the total fluid wetted area (A_w), was adopted as more truly representative of the tortuous flow paths and defined as:

$$D_h = \frac{4V_{open}}{A_w} \qquad (5)$$

This was the same characteristic length used by VanFossen (Ref. 3).

c. Test Matrix

The model was used to study the staggered short pin-fin heat exchanger for various values of pin spacing and Reynolds numbers. Table 4 shows the variables and their values chosen for this study. Except for a few size comparison runs, all test sections were numerically constructed with an axial pitch of 12.7 mm, while the pin diameter was varied to meet spacing requirements. In all cases, *H/D* was set to 1.0.

Table 4 Test configurations, baseline numerical circular pin study

Variable	Values
Re_{Dh}	3,000 – 50,000
S/D	1.25, 1.5, 2.0, 3.0, 5.0
X/D	1.25, 1.5, 2.0, 3.0, 5.0

Using the revised definition of the characteristic length scale in Eq. (5), the Reynolds number is now defined as:

$$\mathrm{Re}_{D_h} = \frac{\rho \bar{U} D_h}{\mu} \qquad (6)$$

where

$$\bar{U} = \frac{\dot{m}}{\rho \bar{A}}$$

and

$$\bar{A} = \frac{V_{open}}{L}$$

3. Data Reduction

Key results were either obtained directly from the CFD package, or calculated using fundamental heat transfer relationships or conservation laws. CFD direct outputs included the total heat transfer rate, inlet and outlet bulk temperatures, pressure drop and mass flow rate. The following steps were followed to calculate the test array Nusselt number and friction factor.

a. Nusselt Number Calculations

1. Total heat transfer rate and mass flow rate were recorded directly from the CFD results file after grid independence had been verified for each run.
2. Outlet bulk temperature was calculated from a simple energy balance as:

$$T_{out} = T_{in} + \frac{Q}{\dot{m}\ C_p} \qquad (7)$$

3. As a check, this outlet temperature was compared with the outlet bulk temperature provided by the CFD results file. In most cases, the temperatures were identical. If the temperatures differed by more than 0.1 K, then the run was repeated with either a revised/finer mesh and/or with an increased number of solver iterations.
4. With output temperature resolved, the log mean temperature difference was calculated over the test array as follows:

$$\Delta T_{lm} = \frac{\left(T_{wall} - Tbulk_{in}\right) - \left(T_{wall} - Tbulk_{out}\right)}{\ln\left(\frac{T_{wall} - Tbulk_{in}}{T_{wall} - Tbulk_{out}}\right)} \qquad (8)$$

5. The heat transfer coefficient was calculated using the following equation:

$$\bar{h}_{array} = \frac{Q}{A_{wetted}\ \Delta T_{lm}} \qquad (9)$$

Finally, the Nusselt number for the array was determined using:

$$Nu_{D_h} = \frac{\overline{h}_{array} D_h}{k} \qquad (10)$$

b. Friction Factor Calculation

The friction factor in the array was calculated using the following definition:

$$f' = \frac{\Delta P_{array} D_h}{\frac{1}{2}\rho \overline{U}^2 L} \qquad (11)$$

where L was the overall streamwise length of the array.

c. Specific Fluid Friction Power

Specific fluid friction power, useful in comparing heat exchanger performance was calculated using the following definition:

$$E = \frac{\dot{m}\Delta p}{\rho A} \qquad (12)$$

where A can be either wetted area or heat exchanger array footprint/face area. Note that E has the units of W/m^2.

4. Results And Discussion

Upon completion of all the test runs, several key performance indicators were examined to understand the heat transfer characteristics and trends for each pin-fin configuration and Reynolds number. No data were obtained for the specific case of *S/D* = 1.25, when *X/D* was 3.0 and 5.0, since numerical convergence was not achieved for these configurations.

a. Nusselt Number

The Nusselt number was calculated for each test configuration. The graphs in Figure 13 and Figure 14 show Nusselt number plotted against Reynolds number on a logarithmic scale for specific *S/D* and *X/D* configurations. While plots of the other

configurations are not shown in the interest of brevity, all of them displayed similar characteristics and trends as the ones provided.

From these figures it was evident that Nusselt number could be correlated as a power law function such as Equation 13. Moreover, from Figure 13, it was also apparent that Nusselt number was fairly insensitive to variations in *S/D* for a given *X/D* and Reynolds number. However, from Figure 14, it was apparent that *S/D* had a greater effect on Nusselt number. These observations led to the conclusion that the leading coefficient, C_N, was a weak function of *X/D*, and a strong function of *S/D*. Similarly the exponent, m, was observed to be a weak function of *S/D*.

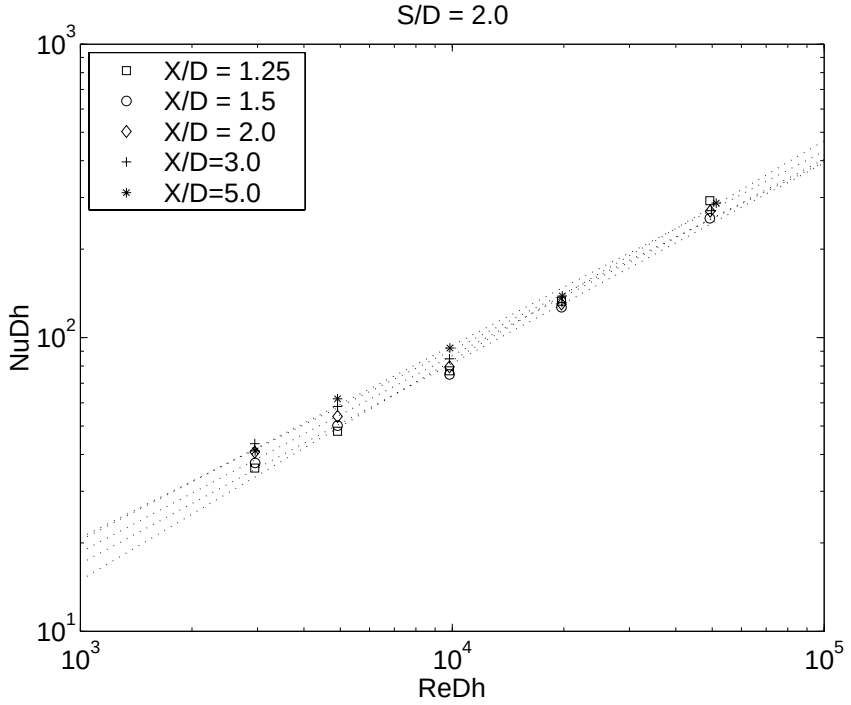

Figure 13 Nusselt number for *S/D* = 2.0, circular pins

After analyzing the curve fit data for the different configurations, the correlation for Nusselt number was derived as:

$$Nu_{D_h} = C_N \, \mathrm{Re}_{D_h}^{m} \qquad (13)$$

where the values of C_N and *m* are provided in Table 5. Using these values, the array Nusselt number can be predicted to within 5% for $3{,}000 \le \mathrm{Re}_{D_h} \le 50{,}000$ for $1.25 \le S/D \le 5.0$ and $1.25 \le X/D \le 5.0$.

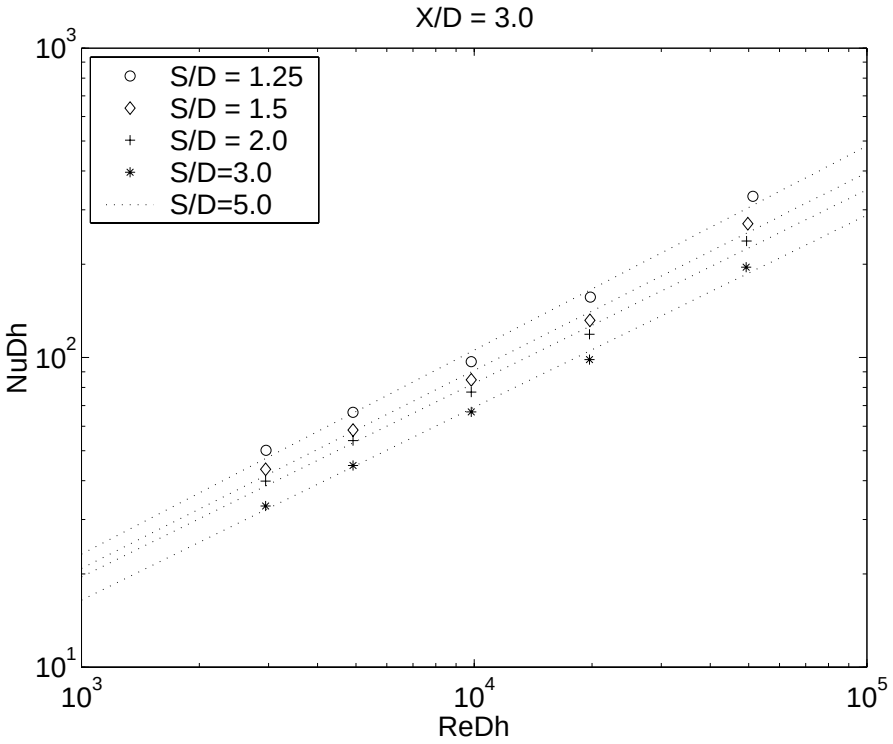

Figure 14 Nusselt number for *X/D* = 3.0, circular pins

Table 5 Nusselt number correlation constants, circular pins, *H/D* = 1

	S/D									
	1.25		1.5		2.0		3.0		5.0	
X/D	C_N	*m*	C_N	*m*	C_N	*m*	C_N	*m*	C_N	*m*
1.25	0.050	0.832	0.069	0.770	0.085	0.748	0.154	0.680	0.193	0.630
1.5	0.071	0.801	0.090	0.753	0.152	0.683	0.166	0.671	0.165	0.650
2.0	0.097	0.777	0.145	0.707	0.183	0.669	0.162	0.680	0.198	0.642
3.0	-	-	0.244	0.659	0.252	0.639	0.259	0.626	0.225	0.622
5.0	-	-	0.431	0.605	0.210	0.662	0.278	0.616	0.238	0.612

However, these constants may also be approximated by simple equations for ease in programming applications using the following definitions:

$$C_N = 0.04\left(S/D\right)^{0.5}\left(X/D\right)^{0.05} \qquad (14)$$

and

$$m = 0.865\left(S/D\right)^{-0.13} \qquad (15)$$

Using these approximations, Nusselt number can be predicted to within ±20% for $3{,}000 \le \mathrm{Re}_{D_h} \le 50{,}000$ for $1.25 \le S/D \le 5.0$ and $1.25 \le X/D \le 5.0$.

b. Friction Factor

The friction factor results have also been plotted for each configuration in a similar manner. The graph in Figure 15 shows friction factor plotted against Reynolds number on a logarithmic scale for *X/D* = 2.0. As in the case of Nusselt number, plots of the other configurations have been omitted for brevity. It can be readily seen that the friction factor varied greatly with changes in *S/D*. This behavior can be reasoned by noticing that for small spanwise spacing the entering flow is forced to follow a tortuous path around the pin fins thus resulting in large pressure drops. However as *S/D* is increased there is an effective opening up of the flow passages and the friction factor approaches the open duct value. The friction factor also increased as *X/D* was increased, primarily due to the increase in the overall array length.

As in the case with Nusselt number, the friction factor was related to Reynolds number with a power function correlation. Using the constants provided by Table 6, the following correlation predicts friction factor to within 5% for $3{,}000 \le \mathrm{Re}_{D_h} \le 50{,}000$ for $1.25 \le S/D \le 5.0$ and $1.25 \le X/D \le 5.0$.

$$f' = C_F \,\mathrm{Re}_{D_h}^{n} \qquad (16)$$

Table 6 Friction factor correlation constants, circular pins, *H/D* = 1

	S/D									
	1.25		1.5		2.0		3.0		5.0	
X/D	C_F	*n*	C_F	*n*	C_F	*n*	C_F	*n*	C_F	*n*
1.25	2.525	-0.018	1.273	-0.040	1.149	-0.050	1.339	-0.069	1.281	-0.155
1.5	4.418	-0.030	1.849	-0.045	1.602	-0.093	1.175	-0.071	1.152	-0.140
2.0	6.243	-0.025	2.318	-0.041	1.429	-0.071	1.192	-0.088	1.189	-0.141
3.0	-	-	2.845	-0.043	1.538	-0.071	1.154	-0.100	1.192	-0.160
5.0	-	-	3.238	-0.039	1.512	-0.073	1.155	-0.119	1.274	-0.198

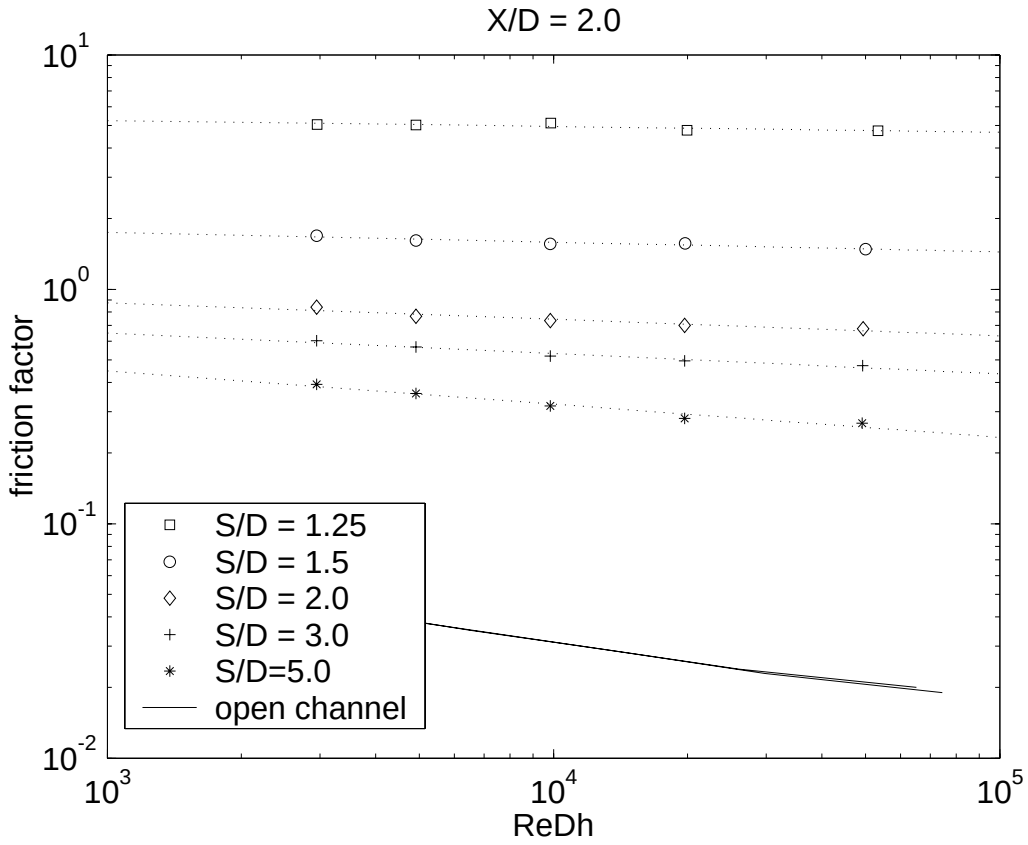

Figure 15 Friction factor for *X/D* = 2.0, circular pins

As with Nusselt number, there may be cases where a simpler mathematical model is desired for programming. In order to derive such a model, relationships for the behavior of friction factor as a function of X/D and S/D were examined. Interestingly, the behavior of the friction factor for configurations with S/D less than 2.0 was very different from configurations with S/D greater than 2.0. Physically, this is likely due to the tortuous nature of the flow lines when S/D is less than 2.0 for which the geometry clearly shows that the uniform flow at the entrance is forced to negotiate a serpentine

path around the pins as noted above. However for S/D greater than 2.0, the geometry indicates the presence of a clear and direct straight "line-of-sight" flow path through the array, whereby it can be argued that some of the flow streamlines can pass straight through the array with minimal or no interaction with the pins, thus resulting in a significant decrease in the pressure drop. Figure 16 shows two numerical solutions with streamlines plotted to further illustrate the effects of S/D on the flow. From this graphic, it is clear that the wider pin spacing results in smoother streamlines and a more direct path through the array. The narrow pin spacing causes nearly all streamlines to negotiate a serpentine path around the pins. These differences in flow geometry result in very different pressure drop characteristics. As a result, two separate correlations for friction factor based on S/D were developed to account for this behavior.

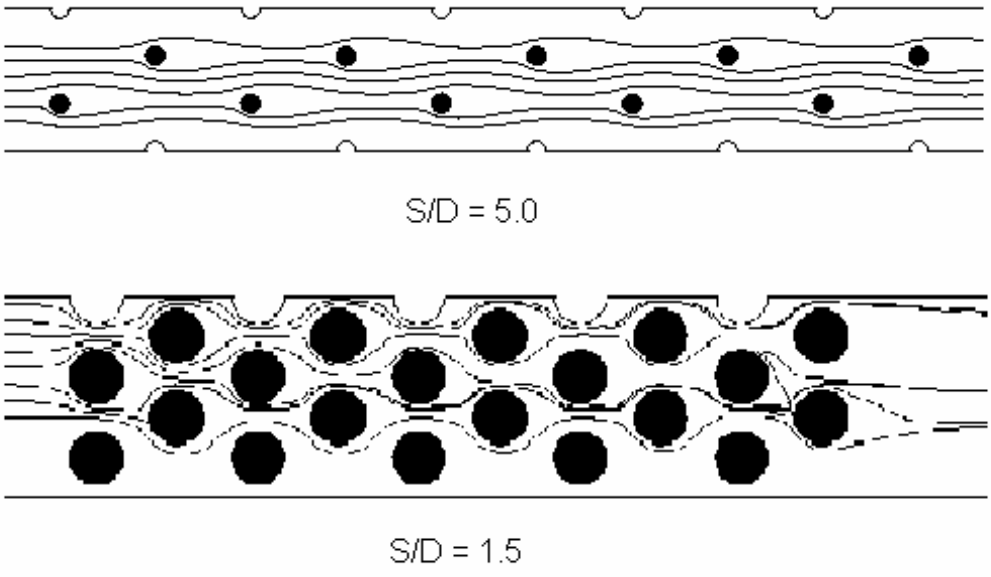

Figure 16 Effect of *S/D* on streamlines

The friction factor correlations developed are as follows:

$$f' = \left[12 - 7.6236\left(S/D\right)^{-0.85}\right]\mathrm{Re}_{D_h}^{-0.5} + B \quad (17)$$

where

$$B = 98.142\left(S/D\right)^{-12}\ln\left(X/D\right) + 0.9197\left(S/D\right)^{-0.5} \quad (18)$$

for $1.25 \le S/D \le 2.0$, and

$$B = \left[0.9262 - 0.1327\left(S/D\right)\right]\left(X/D\right)^{\left[1.6721(S/D)^{-0.8}-1\right]} \quad (19)$$

for $2.0 < S/D \le 5.0$.

These correlations predict friction factor to within ±20% for $3{,}000 \le \mathrm{Re}_{D_h} \le 50{,}000$ for $1.25 \le X/D \le 5.0$.

c. Heat Transfer Coefficient

One of the unique advantages of a numerical study is the ability to obtain detailed local heat transfer coefficient values at any point in the test array. These data provide opportunities to evaluate the relative contributions of both the endwall and pin-fin surface to the total heat transfer problem and identify other regions of interest. Additionally, it is possible to observe the changes in heat transfer coefficient based on location on the pins and along the endwall. Ultimately, these observations can shed light on ways to improve heat exchanger performance. In this section, the numerical solution for the configuration $X/D = S/D = 5.0$ at $Re_{Dh} = 20{,}000$ has been used to probe the local heat transfer behavior in the array in detail.

As previously stated, pin-fins have been introduced in the otherwise planar duct in order to enhance overall heat transfer performance. Although endwall surface area is reduced by the presence of pins, the pins improve heat transfer rate due to the addition of their own surface area, and also by increasing flow turbulence levels on the endwall thereby giving rise to better transport rates. Figure 17 provides a contour plot indicating the local values of the heat transfer coefficient on the endwall of the array as the flow moves from left to right. It is evident that the pins are affecting these local values. For example, the heat transfer coefficient is reduced in the wake or "shadow" of

each pin where the local velocities are low. Further downstream of each pin, the local heat transfer coefficient is enhanced as vortices produced by the pins strike the endwall. Note also that as expected the large velocities achieved in the flow region between the pins tend to increase the film coefficient.

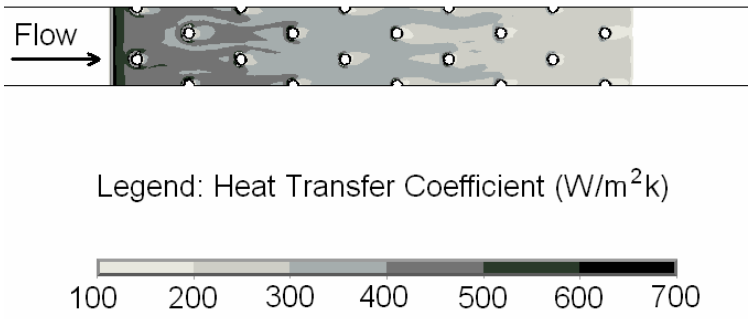

Figure 17 Endwall heat transfer coefficient

In order to quantify the heat transfer benefits gained by adding pins to the planar duct, a comparison was made with empty duct performance. To this end, a numerical model with the same dimensions, but without any pins, was constructed. Using this model, simulations were performed at Re_{Dh} = 20,000, the same conditions that were used to develop the contour map in Figure 17. As a cross-check, heat transfer performance of the empty duct was also calculated using well established semi-empirical correlations (Ref. 18). The numerical and analytical solutions for the empty duct were found to be in very good agreement as shown in Table 7.

Table 7 Empty duct solution comparison

Parameter	Analytical Prediction	Numerical Solution
Friction factor	0.026	0.027
Nusselt Number	50.5	53.6

Figure 18 provides a qualitative comparison of the endwall heat transfer coefficients for the pin-fin array and the empty duct. The data for this plot were obtained directly from the resolved numerical model by recording heat transfer coefficient values for nodes adjacent to the endwall. These nodes were situated on three separate

streamwise paths for the pinned array. One path ran unobstructed between pins while the other two ran through pin centerlines. These paths were chosen to qualitatively evaluate the effects of the pins on endwall heat transfer coefficient. For the empty duct, a single streamwise path was chosen in the center of the duct. Note that for both configurations, local heat transfer coefficients decrease with streamwise travel, initially due to the thickening boundary layer and developing effects, and after the first row additionally due to flow separation effects. However, in nearly all cases, these coefficients for the pinned endwall are greater than those on the endwall of the empty duct. This clearly illustrates the beneficial effect that turbulence from the pins has on the endwall heat transfer performance. The only regions of lower heat transfer coefficient for the pinned array are in the immediate wake or "shadow" of the pins where local velocities are lower. Slightly further downstream of the pin, the heat transfer coefficient rapidly climbs almost to the value of the unobstructed path.

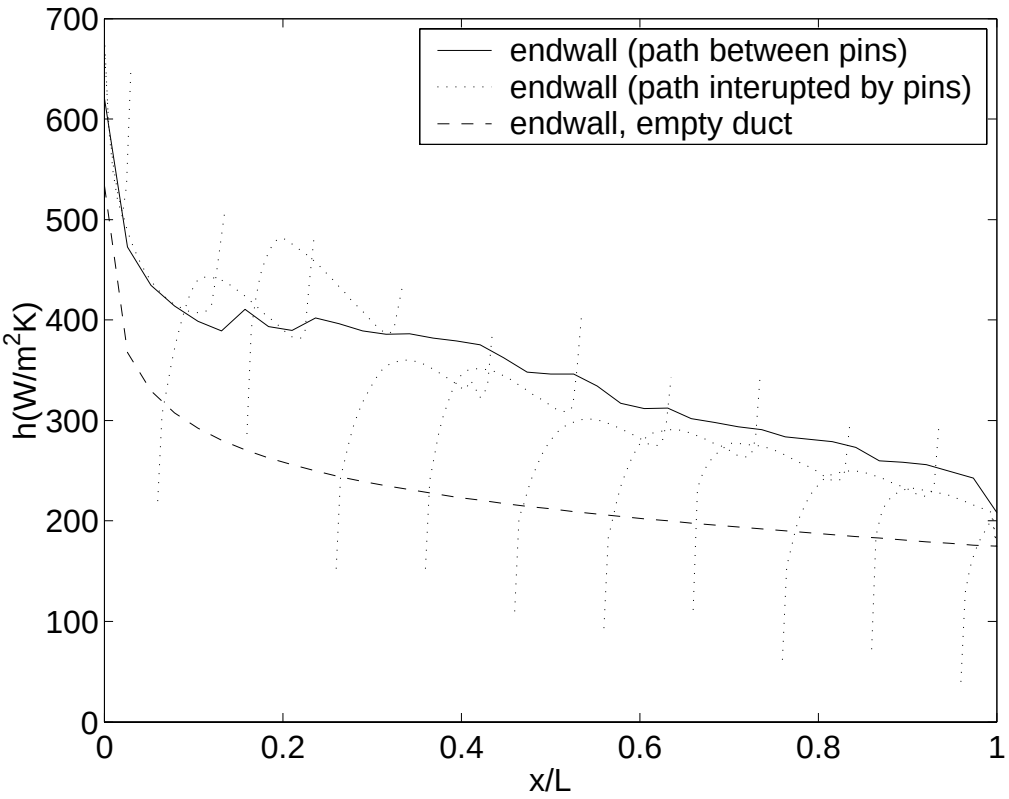

Figure 18 Endwall heat transfer coefficient trends

Examination of heat transfer coefficient trends on the pin surfaces also provided interesting results. Figure 19 consists of radial plots showing the angular variation of the heat transfer coefficient on pins from various rows. In each plot, the flow is from left to right. Local heat transfer coefficients were recorded circumferentially at two heights along the pin measured from the endwall, at $z = D/8$ and $z = D/2$. From these plots it is clear that local heat transfer coefficient is highest on the leading face of the pin. This region is defined on each plot by angles between 90 and 270 degrees. Continuing beyond this region, heat transfer coefficient drops off dramatically as the flow separates from the pin surface. Additionally, the values at the $z = D/8$ height location are significantly lower than those at $z = D/2$ due to the boundary layer effects from the endwall.

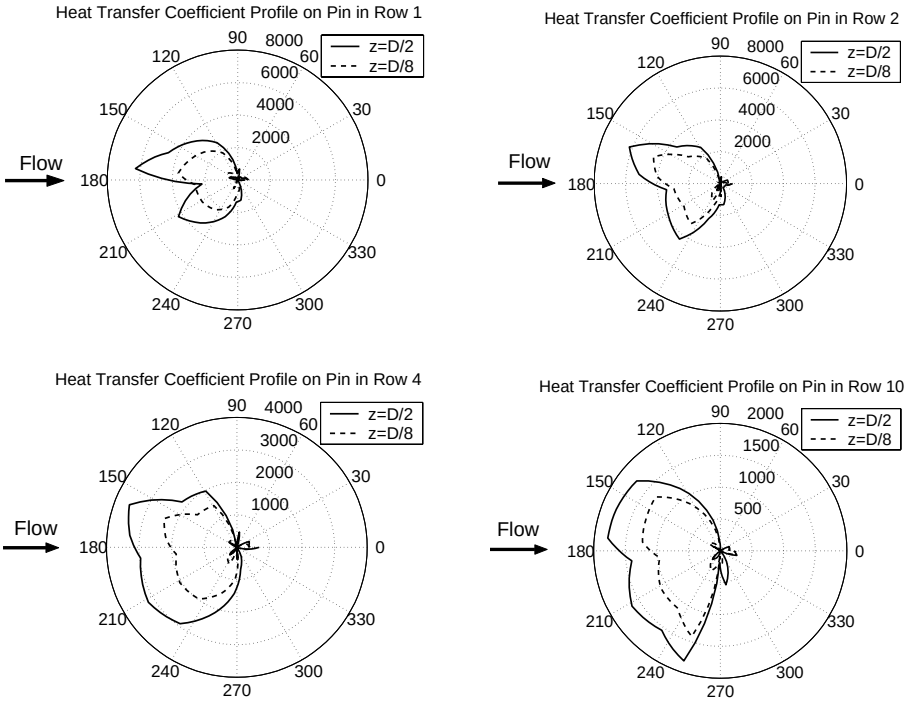

Figure 19 Circular pin heat transfer coefficient profiles

The effects of the endwall are further illustrated by plotting average heat transfer coefficient development as a function of height along the pin. Figure 20 shows this development for pins in various rows. As noted before, the heat transfer coefficient increases with distance from the endwall and shows a slight increasing trend even at the

mid-section of the duct, i.e. at $z = D/2$. This is consistent with the findings of Sparrow et al (Ref. 4) who studied a long isolated cylinder in cross flow to investigate edge effects due to the bounding planes of the surface at the ends of the cylinder. As mentioned previously, they concluded that wall-cylinder interactions were confined to within one diameter of the wall and decreased heat transfer on the cylinder near the wall when compared to regions of the cylinder away from the wall.

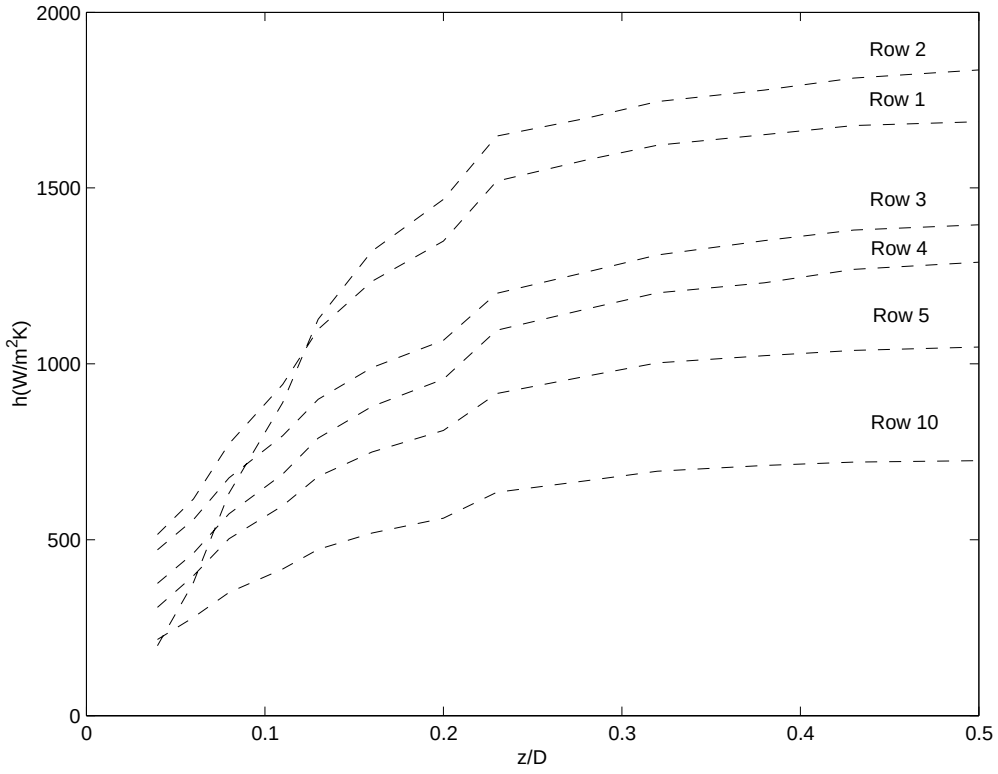

Figure 20 Circular pin heat transfer coefficient trends

Another interesting observation is that the pins in the second row have the highest heat transfer coefficients when compared to pins in the other rows of the array. There are two likely contributors to this observation. First and primarily, the second row of pins encounters a higher local velocity than the pins in row 1. This is due to the "nozzle effect" created by the first row of pins as the flow accelerates to provide a constant mass flow rate through a reduced cross sectional area. This accelerated flow directly impinges on the second row pins due to the staggered geometry thus significantly

increasing heat transfer due to stagnation flow characteristics. A weaker secondary reason is that the turbulence from the first row enhances the heat transfer of the second row. Beyond the second row however there are no additional increases in velocity or turbulence level as shown in Figure 21 and Figure 22 since portions of the flow are now separated and do not lend to the same stagnation flow type enhancement.

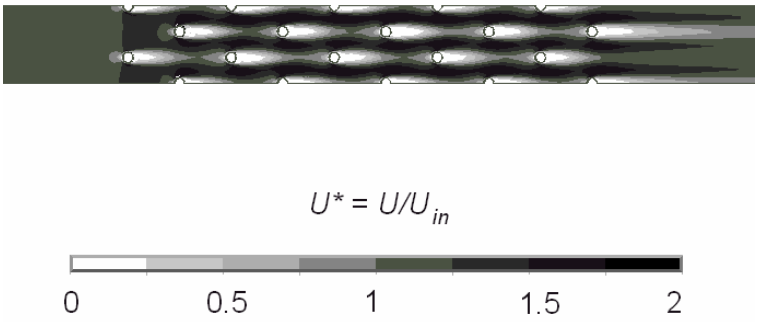

Figure 21 Velocity profile, circular pins

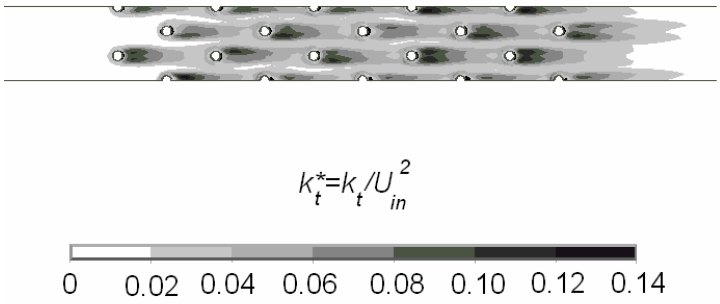

Figure 22 Turbulence level, circular pins

Also of interest is the comparison between the pin and endwall heat transfer coefficients which has been a topic of much discussion in earlier studies. Figure 23 shows a representative case. Note that in this case the heat transfer coefficients from the pins were clearly about 100 – 200% higher than for the endwall. While this magnitude varied for each test configuration, the pin heat transfer coefficient values were always found to be higher by about 50-200%.

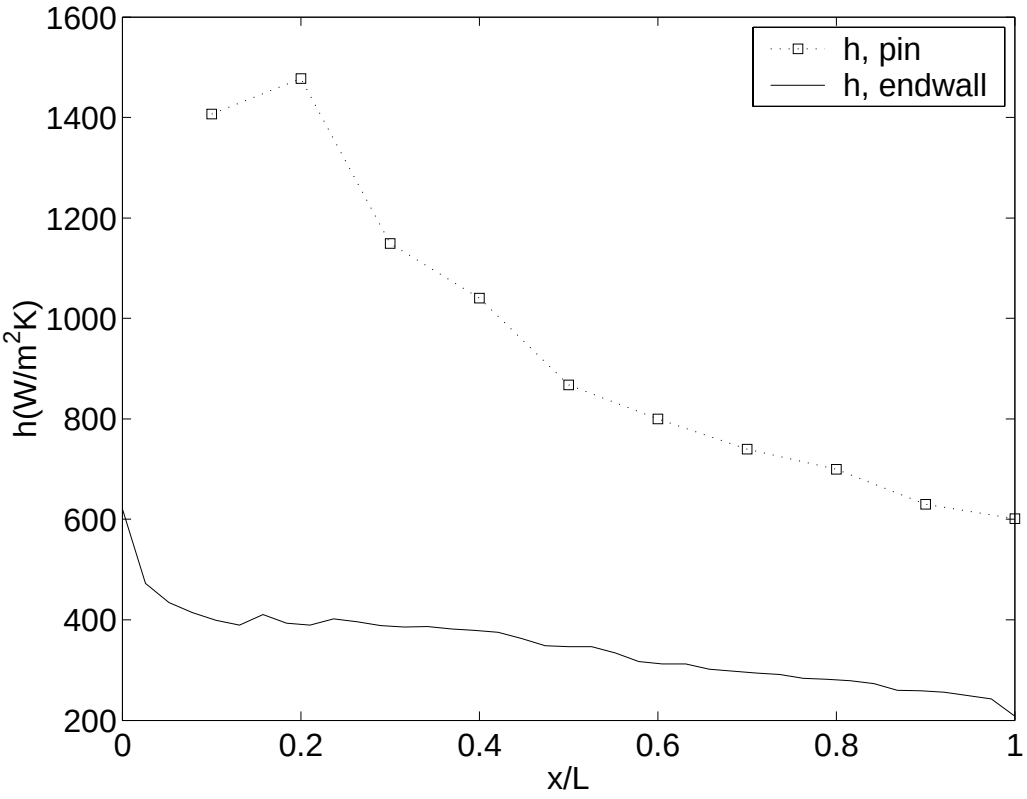

Figure 23 Heat transfer coefficient, circular pins vs. wall

This conclusion is consistent with a majority of the earlier studies that have demonstrated a greater heat transfer contribution from the pin surfaces.

d. Optimization

One of the goals of this study was to predict optimal heat exchanger design configurations that would maximize heat transfer rate while minimizing frictional losses in the flow. As recommended by Kays and London, (Ref. 19) various heat exchanger configurations can be readily evaluated and compared by plotting the heat transfer coefficient versus friction power on a suitable unit surface area basis. Such a plot is provided in Figure 24. For clarity, only two configurations showing the extremes of heat exchanger performance are shown, and compared with empty duct performance. All other configurations fall between these extremes. From this chart, it was clear that for all of the configurations tested, the case of X/D = 5, S/D =3 provided the greatest heat transfer rate per friction power while the case of X/D = 1.25, S/D = 5 was the least

desirable. Surprisingly, the empty duct provided performance nearly as good as the least favorable pin-fin configuration at higher Reynolds numbers. This highlights the need for careful heat exchanger design in order to verify and fully realize the benefits of using pin-fins for performance enhancement.

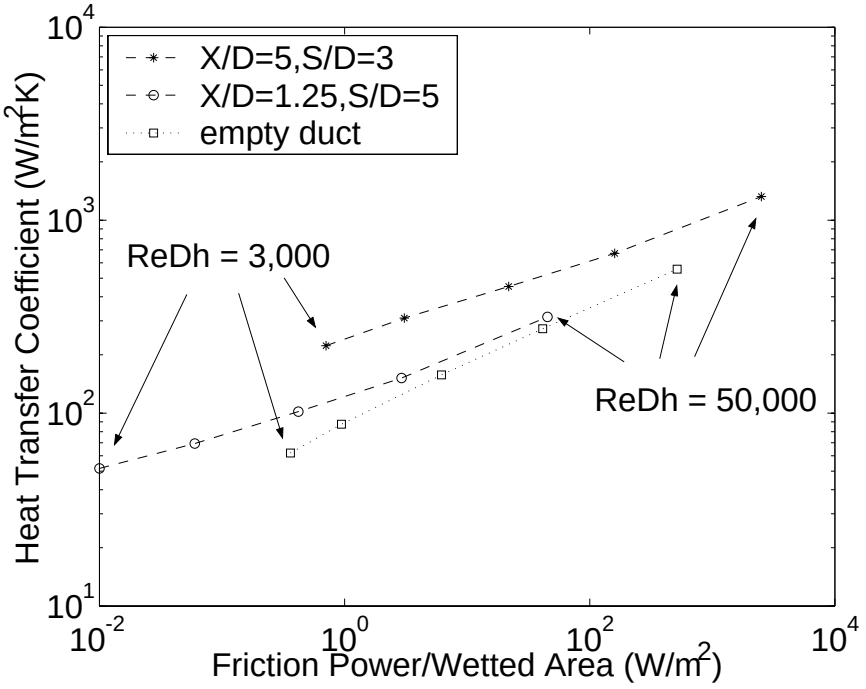

Figure 24 Performance comparison, circular pins

It appeared that the relative goodness of each configuration was closely related to the volumetric density of available heat transfer surface area, or A_w/V. Of all configurations tested, the optimum array had the third highest area density of 829 m^2/m^3 while the worst configuration had the lowest density of 222 m^2/m^3.

The significance in the difference in performance of the different configurations can be quantified by choosing a specific heat transfer coefficient, and comparing the friction power required for each configuration. Using this measure it was found that the least efficient configuration requires up to 15-20 times more friction power for the same heat transfer coefficient, i.e. relatively small gains in heat transfer coefficient require large increases in friction power. For example, for the best configuration, increasing the heat transfer coefficient from 300 to 450 W/m^2K results in friction power increases from 3 to 22 W/m^2. In other words, increasing heat transfer coefficient by 50%

requires over 600% more fluid power. Careful examination of the slope of these graphs can help the designer choose an operating region that provides the best cost/benefit ratio.

e. Application

The actual performance of these heat exchangers can best be quantified by inserting sample initial conditions and calculating predicted performance parameters. For example, assuming a 30K difference between wall and cooling air temperature, the optimum configuration transfers 0.7 W/cm^2 at Re_{Dh} = 3,000 and 4.0 W/cm^2 at Re_{Dh} =50,000.

While 4.0 W/cm^2 is fairly respectable, it is expected that higher rates would be attainable by further increasing the area density of these heat exchangers. Two methods for increasing the heat transfer surface area density are reducing the heat exchanger size and reducing *H/D*. Reducing either size or *H/D* by a factor of 2 results in a doubling of area density. Numerical studies to quantify the effects of variable size and *H/D* on pin-fin heat exchanger performance were completed and are presented in the next sections.

5. Conclusions

The objectives of this investigation were met by simulating various pin-fin heat exchanger configurations with an experimentally validated three-dimensional finite element model. Specifically:

1. Comprehensive power function correlations were developed for Nusselt number and friction factor accurate to within 5% for all configurations at Reynolds numbers between 3,000 and 50,000.

2. Heat transfer coefficients were found to be 50-200% greater for the pin surfaces than for the endwalls.

3. In terms of the heat transfer coefficient, the configuration that required the least amount of fluid friction power was *X/D* = 5.0, *S/D* = 3.0 Conversely, *X/D* = 1.25, *S/D* = 5.0 had the greatest pressure losses.

4. In all pin-fin array configurations, it was found that small increases in heat transfer coefficient resulted in disproportionately large increases in frictional losses thus suggesting the presence of a sensitive design operating point.

B. CIRCULAR PINS, EFFECTS OF AXIAL PITCH

In the previous section, the study focused entirely on pin-fin arrays with a fixed axial pitch of 12.7 mm. It was briefly mentioned that reducing axial pitch would increase area density and therefore had the potential to improve heat exchanger performance. Additionally, it is critical to understand the effects or axial pitch reduction in order to extend the results from macroscale experiments to microscale configurations which are of ultimate interest.

1. Test Approach

a. Test Plan

The previously defined numerical model was used to study the staggered short pin-fin heat exchanger for various configurations and Reynolds numbers. Table 8 shows the variables and their values chosen for this study.

Table 8 Axial pitch test matrix, circular pins

X/D	*S/D*	*H/D*	*X*	Re_{Dh}
2	2	1	3-50mm	3,000 – 20,000
2	2	1	0.75–6 mm	50 – 2,000
1.5	1.5	1	3-50mm	3,000 – 20,000
1.5	1.5	1	0.75–6 mm	50 – 2,000

b. Laminar Modeling

As mentioned previously, the majority of runs were conducted using the standard k-ε turbulence model. However, since some of the variable axial pitch runs included low Reynolds number, laminar modeling was also considered. Figure 25 shows an h vs. E chart for X/D = 1.5, X/D = 1.5 at X = 3mm. This chart includes numerical results obtained with turbulent modeling for Reynolds numbers ranging from 50 to 20,000 as well as numerical results using laminar modeling for Reynolds numbers ranging from 50 to 2000. The models produced nearly identical results for Reynolds numbers in the 1,000 to 2,000 range. However, below a Reynolds number of 1000, the laminar and turbulent solutions were no longer identical. As Reynolds number was decreased, the difference between the two solutions was seen to increase.

According to ANSYS documentation (Ref. 17) the decision on which type of modeling to use can be made by considering the ratio of effective viscosity and

laminar viscosity. In cases where the effective viscosity is less than 5 times greater than laminar viscosity, the documentation recommends using a laminar solution. In this application, it was seen that this point occurred near Reynolds number equal to 1000. This fact, coupled with the behavior observed in Figure 25, lead to the conclusion that laminar modeling should be used for Reynolds number below 1000.

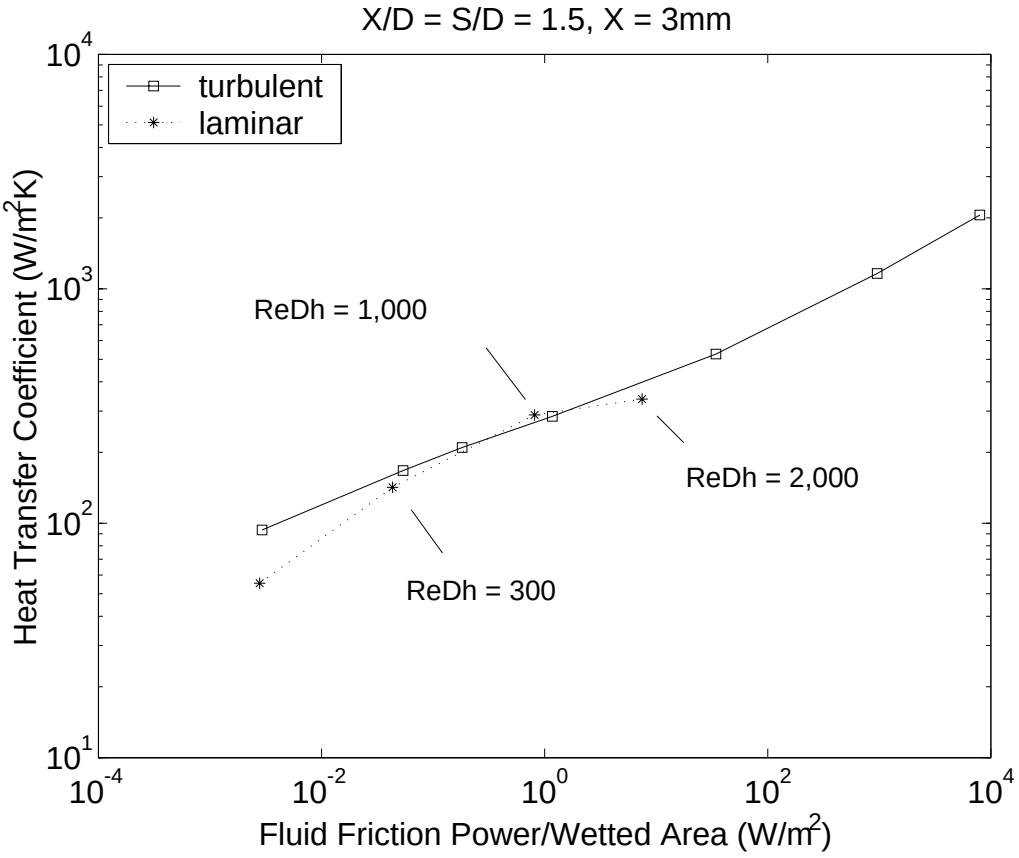

Figure 25 Comparison of laminar and turbulent models

2. Results and Discussion

a. Effects of Axial Pitch on Nusselt Number and Friction Factor

As shown in Figure 26, the dimensionless quantity Nusselt number showed no significant change as axial pitch was varied from the baseline value of 12.7 mm. As axial pitch was decreased, pin diameter had to be decreased to maintain the desired *X/D* values. As a result, the inlet velocity was increased to maintain the Reynolds number at these smaller hydraulic diameter values. This resulted in larger heat transfer

coefficients. However, this increase was offset by the smaller hydraulic diameter when calculating Nusselt numbers.

The effect of axial pitch on friction factor is shown in Figure 27. While there are perturbations for the lower Reynolds numbers, there are no indications that friction factor is dependent on axial pitch. These perturbations are likely aberrations in the numerical data that are consistent with the level of difficulty achieving convergence for these low Reynolds number cases.

While these trends were expected, it was beneficial to confirm them numerically. The obvious benefit of these results is that data obtained either numerically or experimentally for large-scale models may be applied to microscale arrays. Additionally, the consistent behavior of the dimensionless qualities further confirmed the validity of the numerical model and its ability to provide accurate solutions over a wide range of absolute flow velocities.

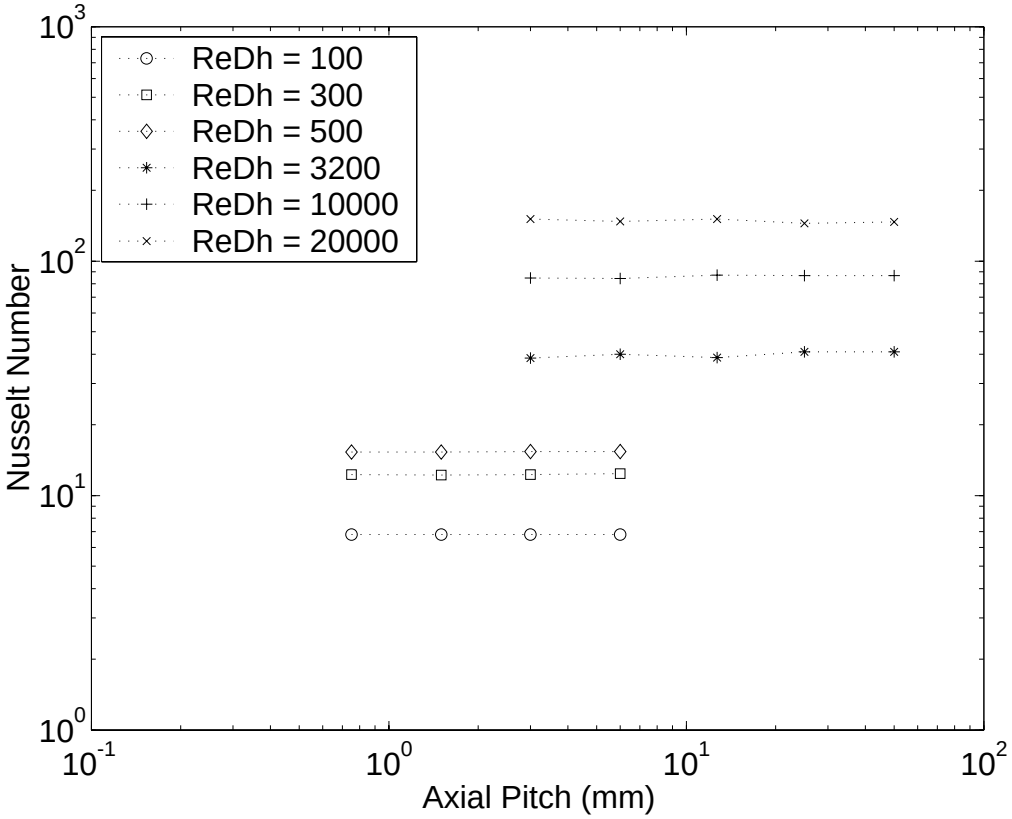

Figure 26 Effect of axial pitch on Nusselt number, circular pins

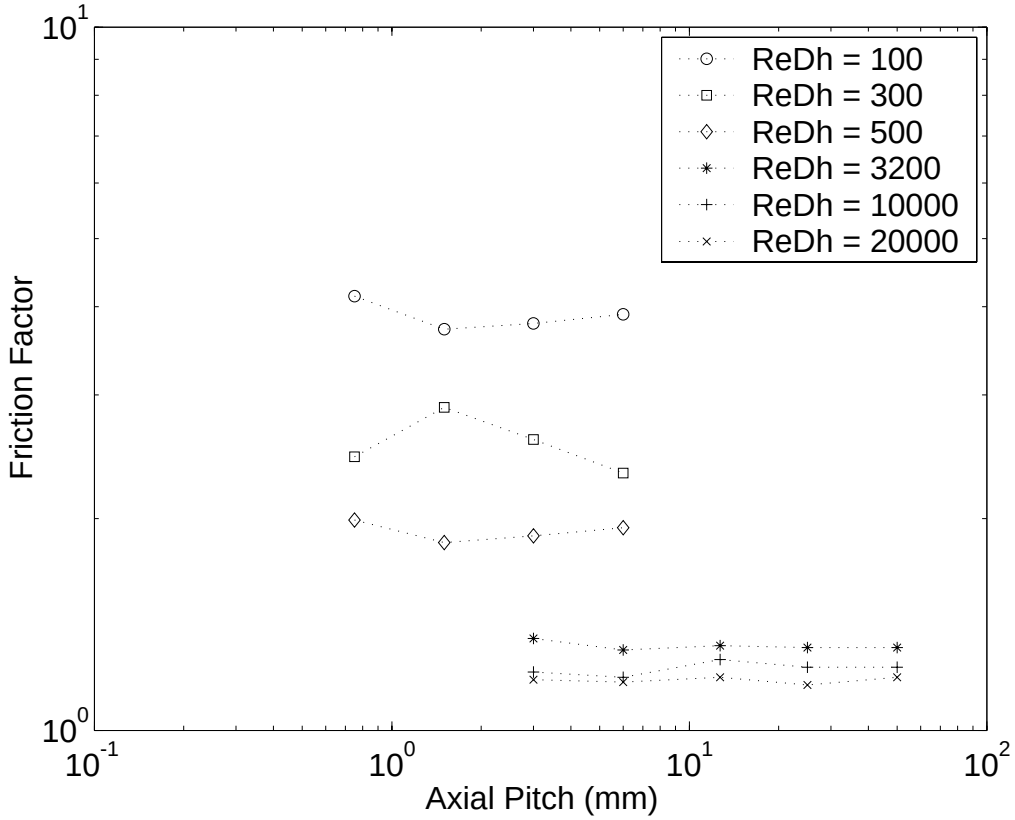

Figure 27 Effect of axial pitch on friction factor, circular pins

b. Performance Comparisons

As in the previous section, a chart plotting heat transfer coefficient versus fluid friction power per wetted area can be made to evaluate heat exchanger performance. Here the desired goal is to maximize heat transfer rate while minimizing losses due to pressure drop. Figure 28 depicts h vs. E for the configuration X/D = 1.5, S/D = 1.5 at various axial pitches and Reynolds numbers. The solid lines indicate constant Reynolds number with varying axial pitch. Conversely, the dashed lines indicate constant axial pitch with varying Reynolds number. From this figure it is clear that heat transfer coefficient and fluid friction power increase as axial pitch decreases and Reynolds number increases. Further, it can be seen that in both all cases, relatively small increases in heat transfer coefficient result in large increases in fluid friction power. A similar graph can be prepared for X/D = 2.0, S/D = 2.0 but has been omitted for brevity.

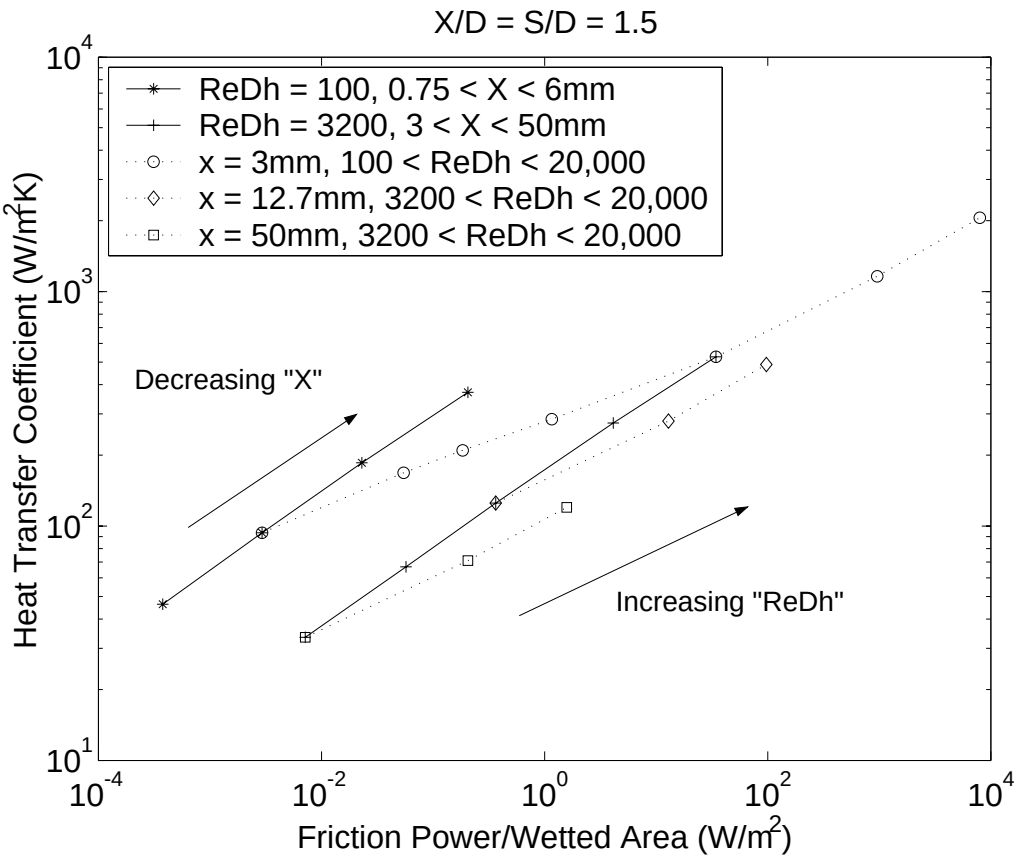

Figure 28 Effect of axial pitch on heat exchanger performance, circular pins

Further examination of Figure 28 reveals that it is more "cost effective" to enhance heat transfer coefficient through reductions in axial pitch rather than through increases in Reynolds number. This is mainly due to the advantages of scale on both heat transfer coefficient and fluid friction power. When holding Reynolds number constant, it was observed that heat transfer coefficient varied inversely with axial pitch. However, because pin diameter was directly related to axial pitch for a given configuration, fluid friction power was inversely proportional to axial pitch cubed. Combining these trends produces the following relationship for heat transfer coefficient and fluid friction power.

$$h \propto E^{0.33} \qquad (20)$$

When holding axial pitch constant, it was observed that heat transfer coefficient varied with the square root of Reynolds number. However, fluid friction

power varied with the Reynolds number squared. Combining these trends resulted in the following relationship.

$$h \propto E_{D_h}^{0.25} \qquad (21)$$

Both of the above relationships are consistent with the trends observed in Figure 28. While the differences in the exponents appear to be small, the impact of these differences is very significant. By way of example, consider the line of constant Reynolds number = 100 shown in Figure 28. The furthest point to the right has an axial pitch of 0.75 mm and produces a heat transfer coefficient of approximately 370 W/m^2K at a friction power cost of about 0.2 W/m^2. To achieve an equivalent heat transfer coefficient of this microscale heat exchanger using an array with an axial pitch of 3 mm, a Reynolds number of about 2,000 is required which produces a friction power loss of approximately 6 W/m^2. Thus, selection of an array that is only 4 times larger results in an increase of fluid friction losses by a factor of 30.

3. Conclusions

The objectives of this phase of the investigation were met by simulating pin-fin heat exchanger configurations with various axial pitch values with an experimentally validated three-dimensional finite element model. Specifically it was found that:

1. Variations in axial pitch were shown to have no appreciable effect on Nusselt number and friction factor. This not only validated the choice of hydraulic diameter as a suitable characteristic length but also demonstrated that the results of macroscale experiments could be directly applied to microscale heat exchangers.

2. Reductions in axial pitch can produce a significant increase in heat exchanger performance. In fact, it was shown that reducing axial pitch is more cost effective than increasing Reynolds number to improve performance.

C. CIRCULAR PINS, EFFECTS OF PIN HEIGHT RATIO

The purpose of this section is to discuss the effect of pin height ratio on circular pin-fin heat exchanger performance. Variations in pin height ratio, like reductions in axial pitch have a large effect on area density. This phase of the study demonstrates the result of these effects.

1. Test Approach

The majority of test runs were conducted using a numerical model with pin spacing ratio of $S/D = X/D = 2$ and H/D varying from 0.25 to 4.0. Reynolds number ranged from 2,000 to 64,000. Additional configurations were also run to spot check Nusselt number and friction factor correlations developed from this primary test configurations and are shown later.

2. Results and Discussion

Upon completion of the test runs, key data were obtained and Nusselt number and friction factor values were calculated for each configuration and Reynolds number. The results of these runs are presented in this section.

a. Effects of Pin Height Ratio on Nusselt Number

Figure 29 shows Nusselt number plotted against Reynolds number for various H/D configurations of the single pin spacing $X/D = S/D = 2.0$. Note that the Nusselt number tended to increase as H/D increased from 0.25 to 4.0. This effect is more pronounced at higher Reynolds number.

This increase was consistent with the geometric differences in the test arrays. As H/D increased, hydraulic diameter also increased resulting in lower absolute flow velocities for a given Reynolds number. These lower velocities produced lower array averaged heat transfer coefficients. However, the hydraulic diameter increased at a greater rate than the heat transfer coefficient dropped. As a result, the Nusselt number increased.

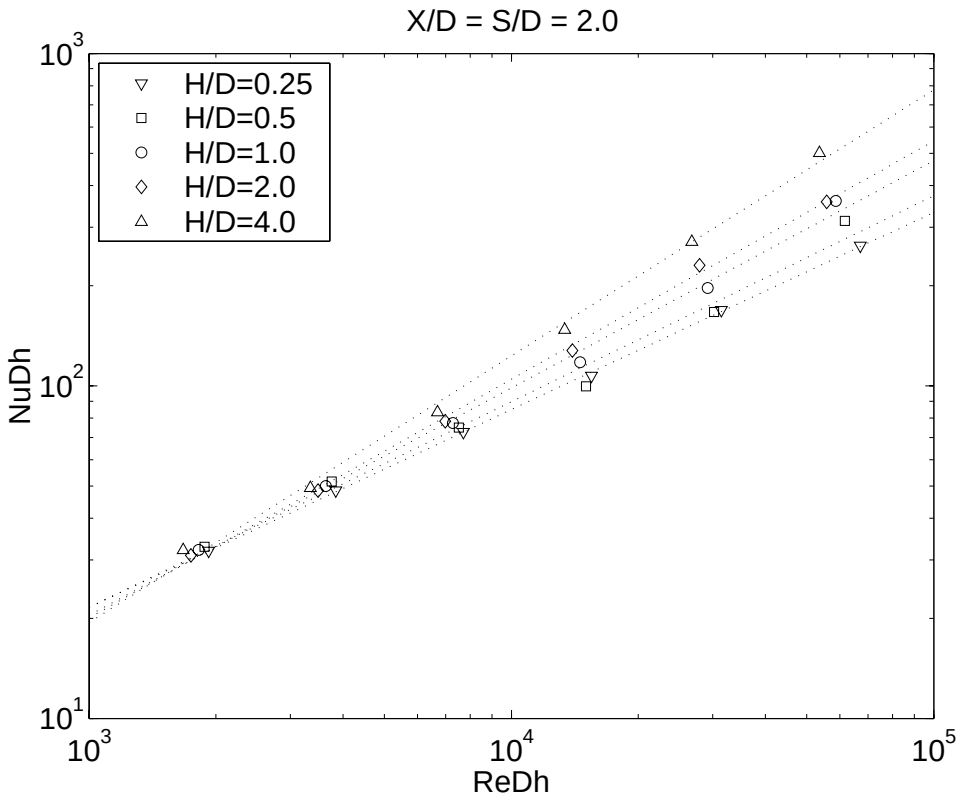

Figure 29 Effect of H/D on Nusselt number, circular pins

Compared to the baseline case of *H/D* = 1.0, each variation in *H/D* acted as a magnification factor that depended on Reynolds number and pin height ratio. It was recognized that this amplification factor could be estimated by a power function correlation. By curve fitting these factors, the following magnification relation was derived:

$$A_N = \left(\frac{H}{D}\right)^{-0.5} \mathrm{Re}_{D_h}^{\,0.68\left(\left(\frac{H}{D}\right)^{0.11}-1\right)} \qquad (22)$$

Combining this amplification factor with the previously developed Nusselt power function correlation of equations 13 through 15, results in:

$$Nu_{D_h} = C_N \,\mathrm{Re}_{D_h}^{\,m} \qquad (23)$$

where

$$C_N = 0.04\left(\frac{X}{D}\right)^{0.05} \sqrt{\left(\frac{S/D}{H/D}\right)} = 0.04\left(\frac{X}{D}\right)^{0.05} \sqrt{\frac{S}{H}}$$

and

$$m = 0.865\left(\frac{S}{D}\right)^{-0.13} + 0.68\left(\left(\frac{H}{D}\right)^{0.11} - 1\right)$$

This correlation predicts Nusselt number to within ±30% for $3{,}000 \le \mathrm{Re}_{D_h} \le 50{,}000$ for $1.25 \le \frac{S}{D} \le 5.0$, $1.25 \le \frac{X}{D} \le 5.0$ and $0.25 \le \frac{H}{D} \le 4.0$

b. Effects of Pin Height Ratio on Friction Factor

Figure 30 shows friction factor plotted against Reynolds number for all *H/D* configurations tested. As with Nusselt number, friction factor is magnified as *H/D* increases from 0.25 to 4.0.

As with Nusselt number, this increase was also consistent with geometric characteristics of the test arrays. Higher *H/D* resulted in lower flow velocities and subsequently less pressure drop for a given Reynolds number. However, the rate of decrease in pressure drop was overcome by the rate of decrease in the square of the velocity. As a result the friction factor increased for higher *H/D* configurations even though pressure loss was dramatically lower than in the lower *H/D* configurations.

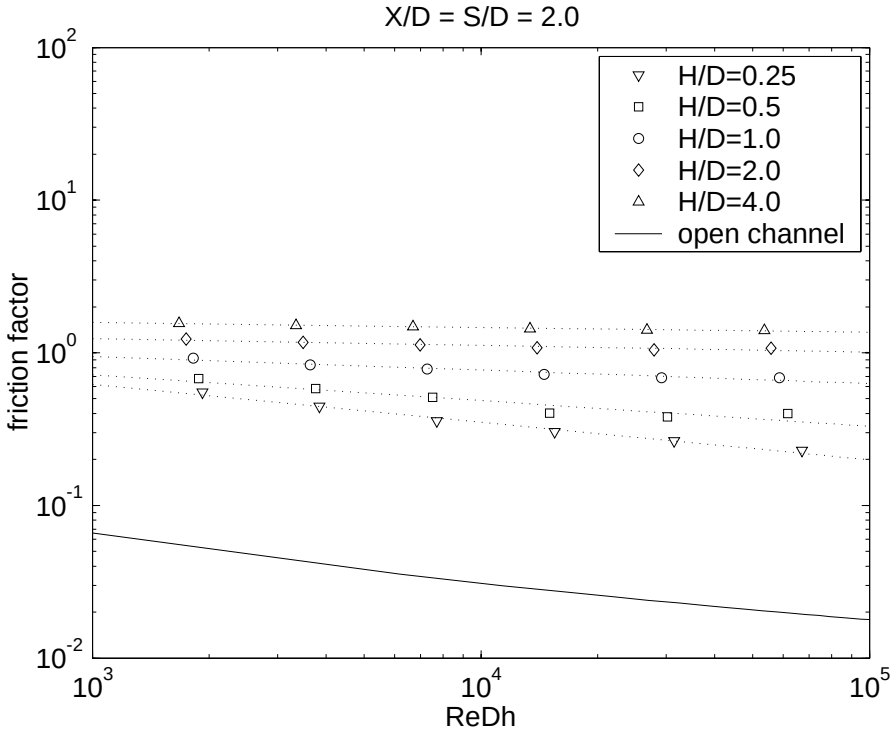

Figure 30 *H/D* effects on friction factor, circular pins

As before, it was apparent that a power function correlation would adequately represent the magnification of friction factor. Curve fitting these factors resulted in the following amplification equation:

$$A_f = \exp\left[0.2\left(\ln\frac{H}{D} - \ln 2\right)^2\right] \mathrm{Re}_{D_h}^{-0.119\left(\frac{H}{D}^{-0.68} - 1\right)} \qquad (24)$$

Combining this amplification factor with the previously developed friction factor power function correlations results in:

$$f' = A_f C_F \mathrm{Re}_{D_h}^{n} \qquad (25)$$

where

$$C_F = 22.67\left(\frac{S}{D}\right)^{-6.37} \ln\left(\frac{X}{D}\right) + 1.4$$

and

$$n = -0.085\left(\frac{S}{D}\right) + 0.085$$

$$\text{for } 1.25 \le \frac{S}{D} \le 2.0$$

and

$$C_F = 0.25\left(\frac{S}{D}\right) + 1.7$$

and

$$n = -0.041\left(\frac{S}{D}\right) - 0.019$$

$$\text{for } 2.0 < \frac{S}{D} \le 5.0$$

These correlations predict friction factor to within ±30% for $3{,}000 \le \mathrm{Re}_{D_h} \le 50{,}000$ for $1.25 \le \frac{X}{D} \le 5.0$ and $0.25 \le \frac{H}{D} \le 4.0$.

Since these correlations were developed based on trends seen in a single configuration, it was necessary to validate its ability to predict Nusselt number and friction factor over a wide range of configurations and Reynolds numbers. To

accomplish this, the configurations listed in Table 9 were run. The last two columns indicate ratios of values predicted by the correlations divided by values obtained numerically. In the majority of cases, the values predicted by the correlations are within 30% of the numerically obtained values.

Table 9 Correlation "Spot check" results, circular pins

X/D	*S/D*	*H/D*	Re_{Dh}	Nu_c/Nu_m	f_c/f_m
1.5	1.5	0.25	3,000	1.01	1.02
1.5	1.5	0.25	50,000	1.34	0.67
1.5	1.5	4.0	3,000	0.95	1.14
1.5	5.0	0.25	3,000	0.95	0.95
1.5	5.0	0.25	50,000	1.33	0.65
1.5	5.0	4.0	3,000	0.79	0.96
1.5	5.0	4.0	50,000	1.00	0.75
3.0	5.0	0.25	13,000	1.11	0.75
3.0	5.0	4.0	17,000	0.92	0.79
5.0	1.5	4.0	3,000	0.69	0.73
5.0	1.5	4.0	50,000	1.02	0.87
5.0	2.0	4.0	8,200	0.95	0.99
5.0	5.0	4.0	3,000	0.73	0.85
5.0	5.0	4.0	50,000	0.97	0.58

c. Combined Effects of Axial Pitch and Pin Height Ratio

One critical objective of this study was to ensure that heat exchanger performance correlations were applicable to microscale designs. Earlier, it was shown that Nusselt number and friction factor were relatively independent of axial pitch at $H/D = 1$. A spot check was run at $S/D = X/D = 5.0$ and $H/D = 4.0$ to demonstrate that these important dimensionless parameters remained unchanged as axial pitch was varied. Figure 31 and Figure 32 show the results of this investigation. It was observed that Nusselt number was insensitive to changes in axial pitch and friction factor changed by less than 15% as axial pitch was varied from 3 to 50 mm. This finding is important if the previously developed correlations are to be used to predict heat exchanger performance in microscale applications.

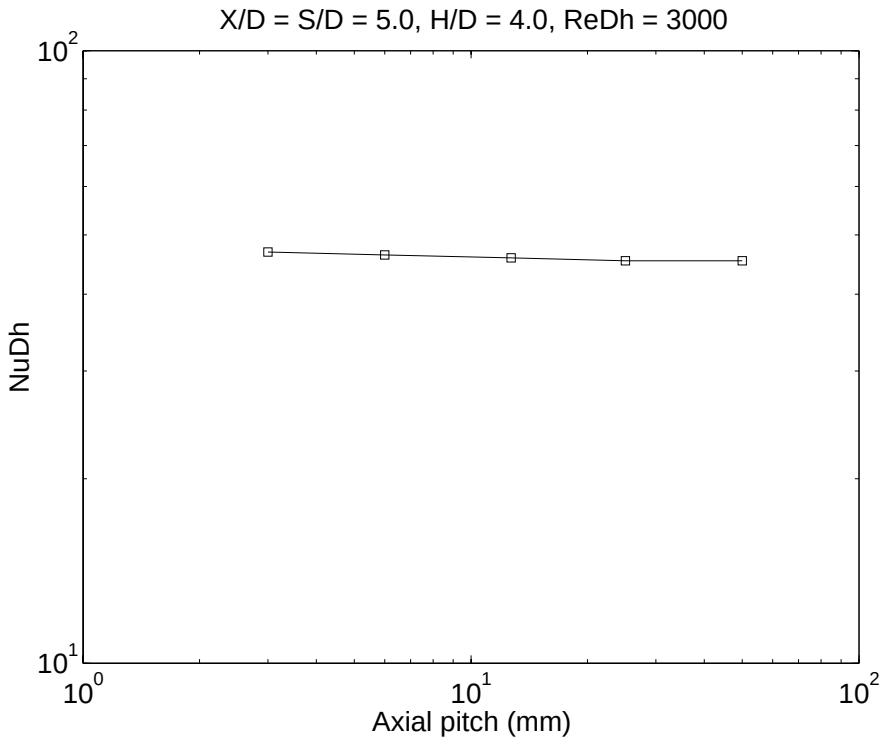

Figure 31 Effect of axial pitch on Nusselt number, *H/D* = 4

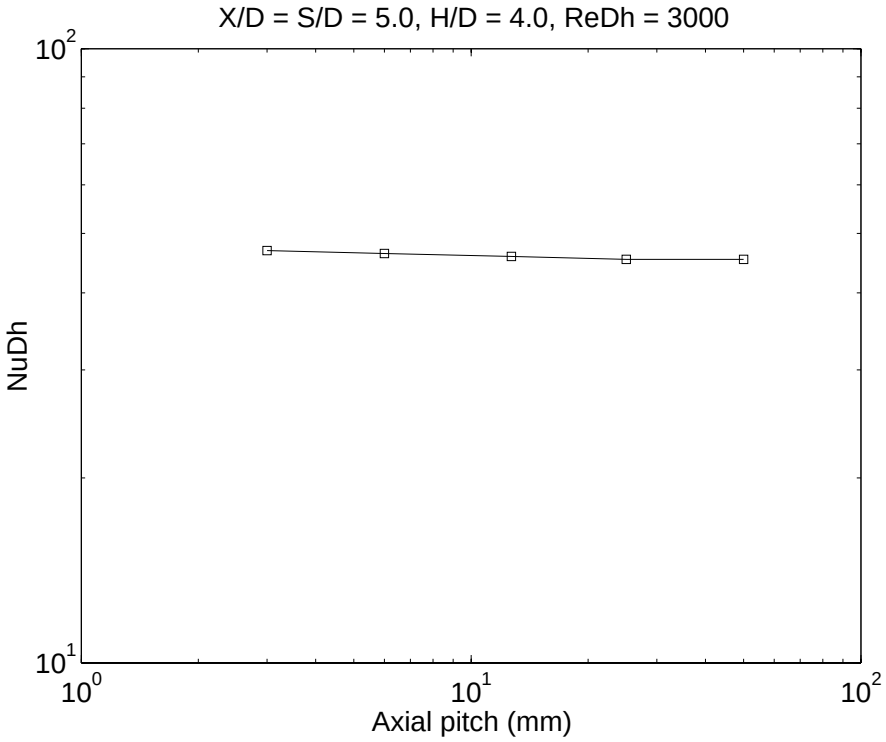

Figure 32 Effect of axial pitch on friction factor, *H/D* = 4

d. Performance Comparisons

In order to determine the effects of variable *H/D* on heat exchanger performance, all configurations tested were plotted as a series of *h* vs. *E* curves. Figure 33 contains a plot of *h* vs. *E* on a wetted area basis while Figure 34 shows *h* vs. *E* on a face area basis. On a wetted area basis, heat exchanger performance tended to decrease as *H/D* was increased from 0.25 to 4.0. This performance decline was mainly due to the decrease in area density as pin height ratio increased. For *H/D* = 0.25, the area density was 11.50 cm^2/cm^3, while for *H/D* = 4.0 it decreased to 1.75 cm^2/cm^3.

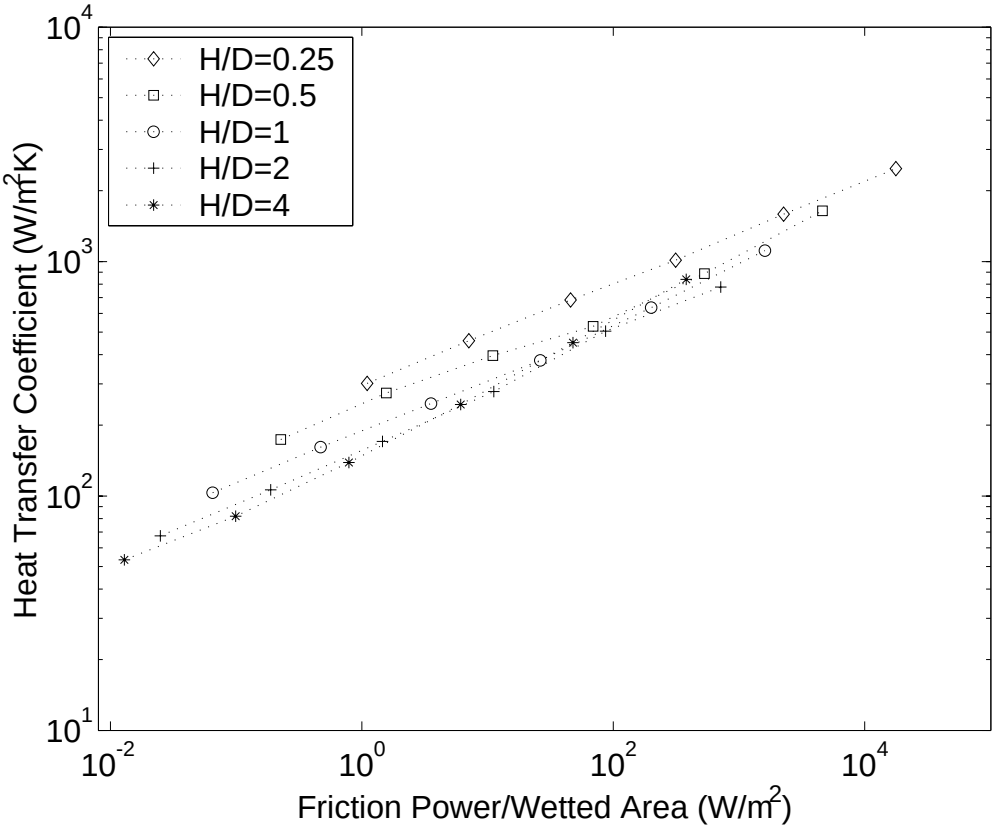

Figure 33 Effect of H/D on performance, wetted area basis

However, when considering performance based on a face area basis the optimum pin height ratio tested was 4.0 despite the fact that this configuration had the lowest area density. This was likely due to two factors. First, the longer pins presented

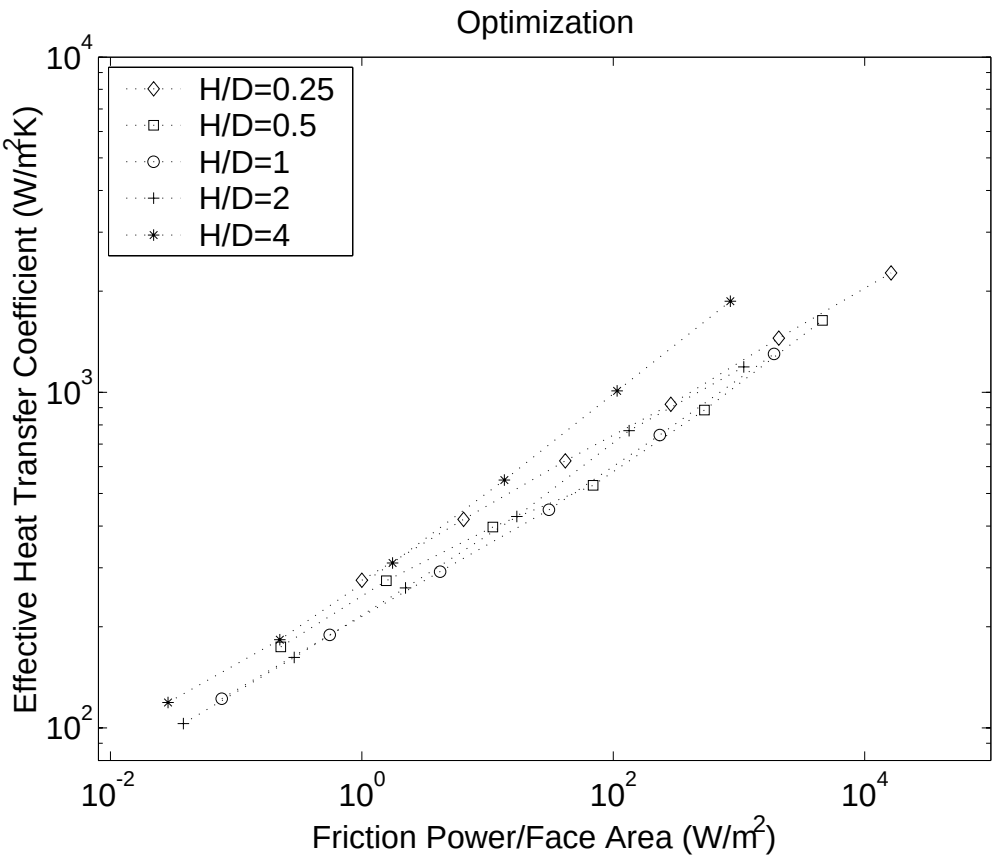

Figure 34 Effect of H/D on performance, face area basis

increased surface area to provide heat transfer. Thus a greater amount of heat had to be transferred through the heat exchanger footprint thereby increasing the effective heat transfer coefficient. Additionally, it has been shown Sparrow et al (Ref. 4) that the presence of the endwall tends to degrade heat transfer coefficient on the pins. As this degrading effect is primarily limited to a distance from the endwall equal to approximately one pin diameter, the longer pins would have greater length with a higher heat transfer coefficient. This point is further illustrated in Figure 35 which shows the heat transfer coefficient for pins of varying height ratio. Note that for $H/D = 1$, only a small percentage of the pin length is close to the maximum value of the mid-pin heat transfer coefficient. As pin height ratio increases, a larger percentage of the pin length is exposed to maximum heat transfer levels. Note that $H/D = 8$ was not part of the test matrix but it has been included in this chart to further illustrate the trend.

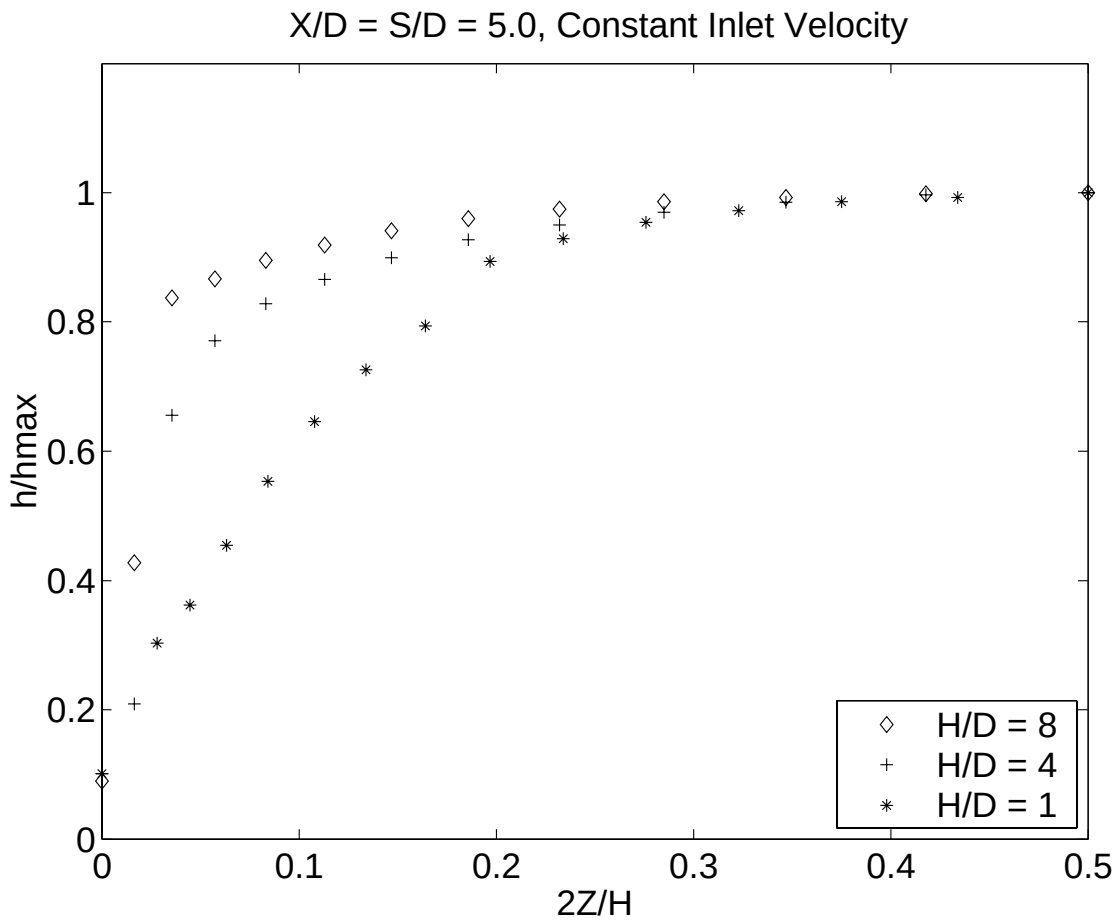

Figure 35 Heat transfer coefficient development on circular pins

Returning to Figure 34, some interesting trends are noted regarding pin height ratio effects. As expected from the previous argument, the configurations *H/D* = 2.0 and 1.0 provide considerably less desirable performance than *H/D* =4.0. However, when pin height ratio is further reduced from 0.5 to 0.25, the trend actually reverses. In this case the increase in area density associated with the smaller pin height ratio has overcome the degradation due to wall interaction on the cylinders.

While these trends were observed for *X/D* and *S/D* = 2.0, it was not obvious that the same would hold true for other pin spacing such as *X/D* = *S/D* = 5.0. This configuration was investigated and the results are provided in Figure 36. In this case, the performance of the larger pin height ratio is not significantly different from the configuration *H/D* = 1.0. As before, the changes in area density are likely the reason for these trends. As shown in Figure 37, this difference in area density is more significant

for the widely spaced pin configuration. For $X/D = S/D = 5.0$, the area density at $H/D = 1$ is significantly higher than it is at $H/D = 4$. As a result, the gains in effective heat transfer performance achieved through longer pins are matched by the performance gains associated with the higher area density of the short pin configuration. Based on these observations, it appears that enhancing heat transfer rates across the face area of pin-fin heat exchangers by increasing H/D is more effective for streamwise and spanwise pin spacing ratios less than 5.0.

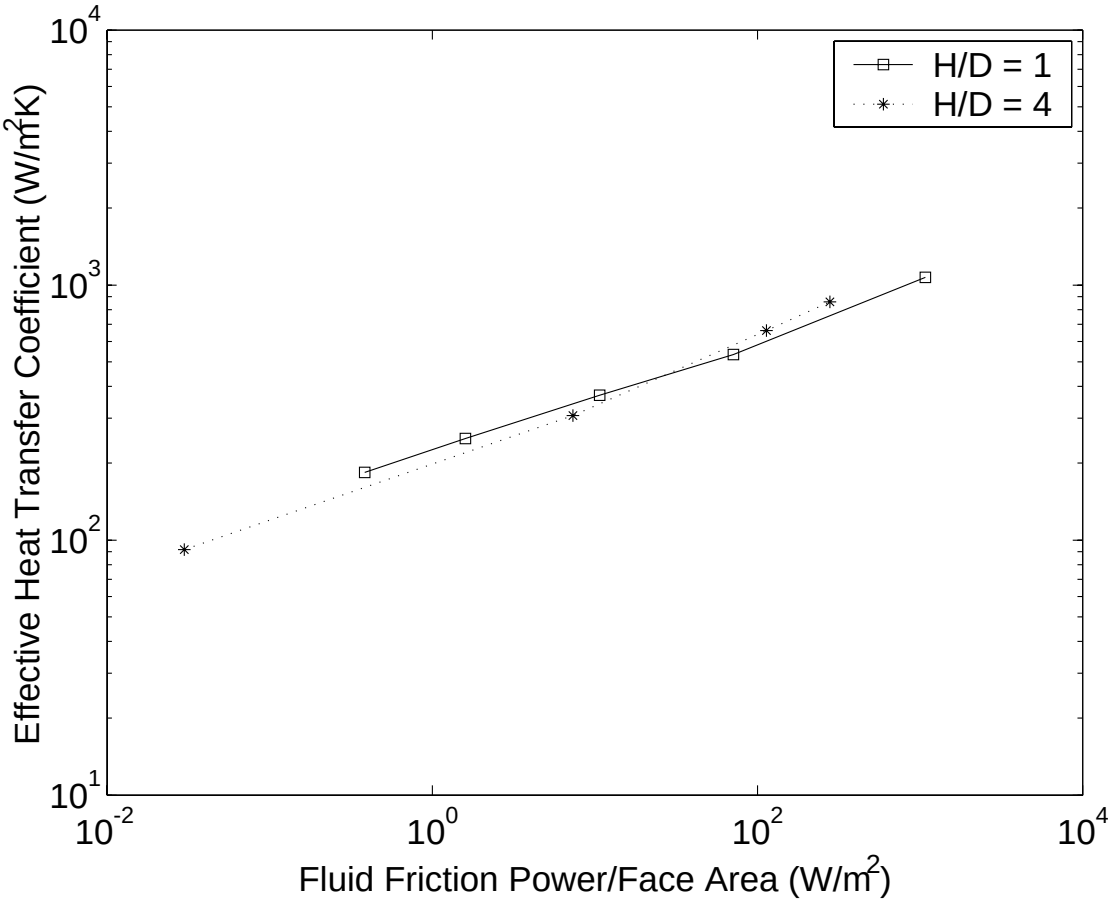

Figure 36 *H/D* effects on performance, wide circular pin spacing

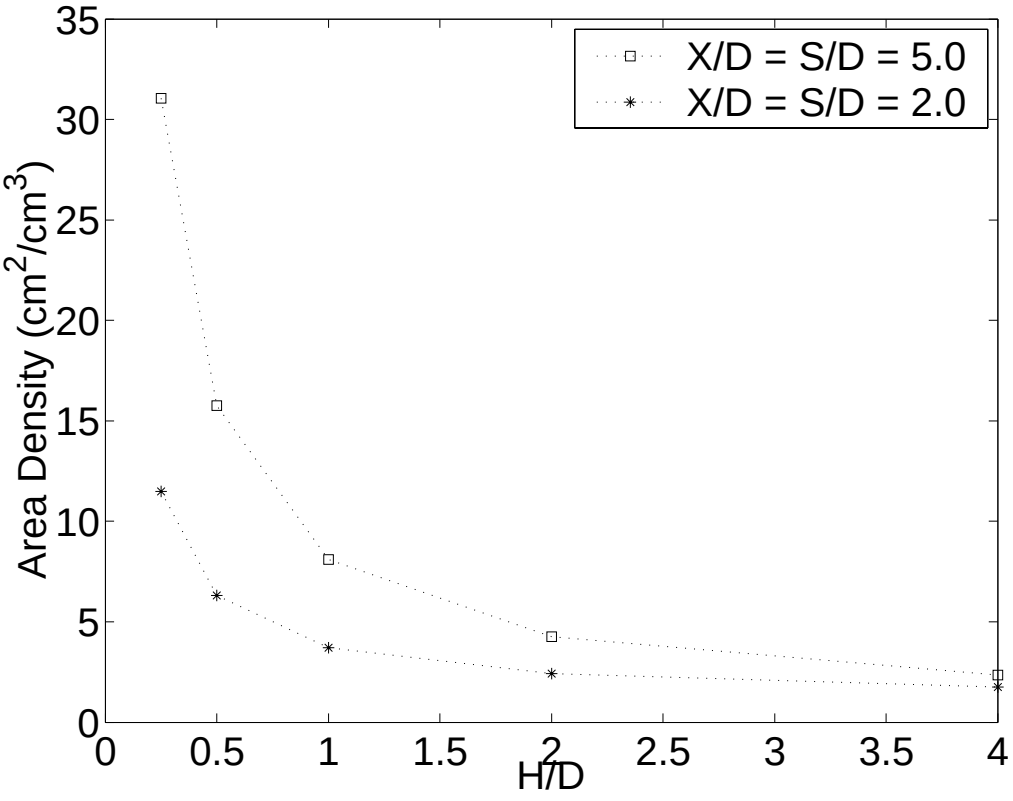

Figure 37 *H/D* and pin spacing effects on area density

e. Effects of Pin Height Ratio on Endwall Heat Transfer Coefficient

It has been shown above that the presence of the endwall has a significant effect on the pin heat transfer coefficient profile. The effect of the pin height ratio on the endwall heat transfer coefficient can also be examined using standard CFD post processing tools. Figure 38 shows contour plots indicating endwall heat transfer coefficient values for three different pin height ratios. Note that *H/D* = 8 was not part of the original test matrix but has been included to explore possible trends. From this figure it appears that higher pin height ratios result in greater variations in heat transfer coefficient along the endwall especially in the spanwise direction. This is likely due to the greater space available for vortex growth as the cooling air swirls around the longer pins. Additionally, the impact of viscous damping on the wall may be reduced in the longer pin configuration.

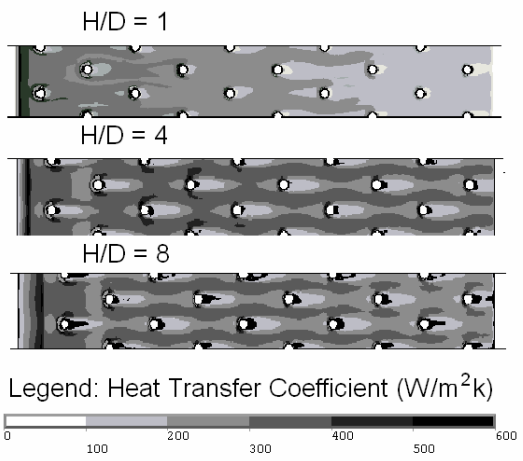

Figure 38 *H/D* effects on endwall heat transfer coefficient

However, despite the significant local variations in heat transfer coefficient seen in long pin configurations, the overall values are not significantly different from the short pin case. Figure 39 shows a comparison of average heat exchanger coefficient values for different pin height ratios. Cooling air inlet velocity was held constant for all cases to provide an opportunity to compare absolute values of heat transfer coefficient. A comparison is also made with the empty duct to further illustrate the beneficial effect of adding pins to enhance heat transfer rate. Interestingly, the long pin heat transfer coefficient profile tends to behave like the profile seen in the empty duct. Although its average is significantly higher, the long pin heat transfer coefficient profile rapidly decreases and then levels out much like the empty duct case. Also, the large variations seen in the contour plots are seen as highly fluctuating absolute values in Figure 39. These actions support the earlier suggestion that longer pin configurations have reduced effect from viscous wall damping.

The three dimensional model provides visibility into the nature of the flow in the vicinity of the junction of the pins and endwall. Figure 40 shows an isometric and side view of streamlines in the flow as they pass over the pins. Note that there is some variation of the streamlines in the "z" or pin axis direction. Presumably this adds to the effective transport of heat that is promoted by the presence of the pins. Additionally, the streamlines are seen spreading around the pin bases in the vicinity of the wall as the vortices are formed.

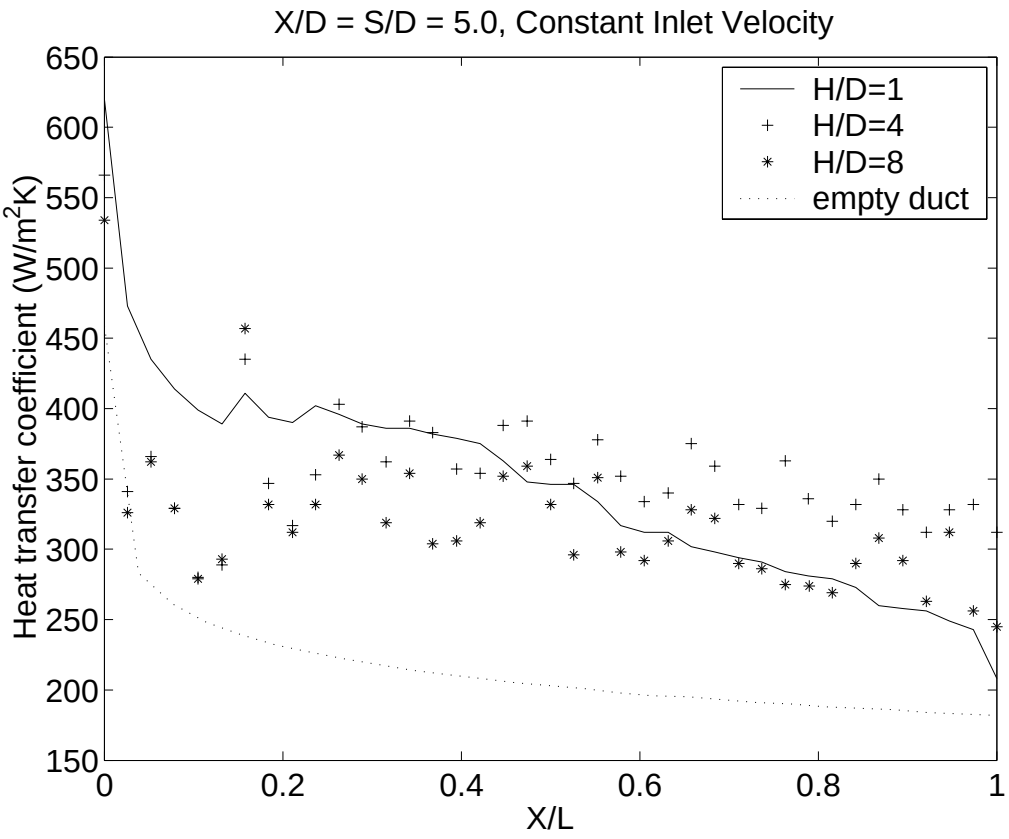

Figure 39 Endwall heat transfer coefficient comparison

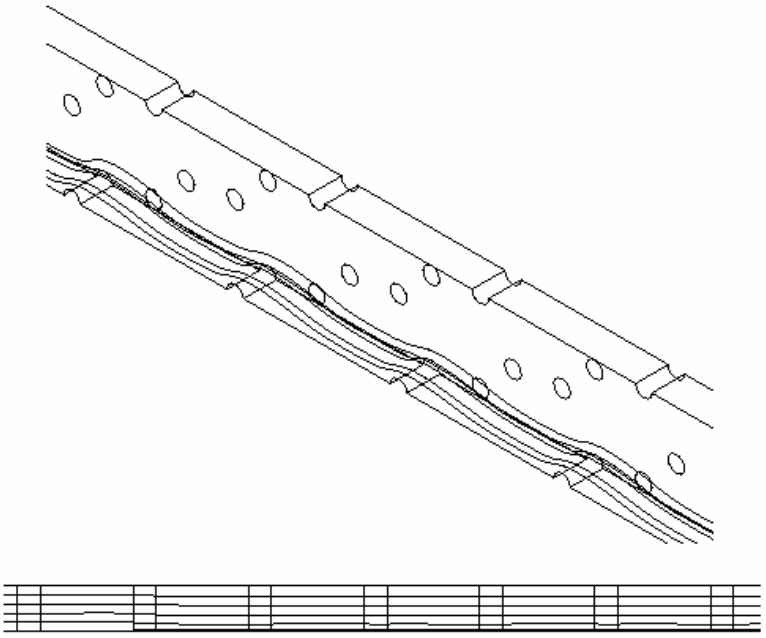

Figure 40 Streamline vertical development within pin-fin array

f. Optimization

By combining the effects observed in this study, an optimum theoretical heat exchanger configuration can be determined. The optimum configuration would consist of small axial pitch, small *H/D*, large *S/D* and *X/D* and operate at low Reynolds number. Table 10 shows the logical progression as these enhancing features are applied starting from a baseline configuration. All configurations compared have *S/D* and *X/D* held at 5.0. Within the bounds of this test program, the optimum configuration would be defined as X = 0.75 mm, H/D = 0.25, X/D = 5.0 and S/D = 5.0 and would have an area density of 525 cm^2/cm^3.

Table 10 Optimization configurations, circular pin-fin array

Config	X (mm)	H/D	A_w/V ($cm^2/cm^{3)}$
baseline	12.7	1.0	8.1
min pitch	0.75	1.0	137.1
min H/D	0.75	0.25	525.8

Figure 41 shows an h vs. E chart that shows the performance of these theoretical optimization designs. As expected the baseline configurations provides the worst performance. Reducing the axial pitch greatly increases the heat exchanger performance. Finally, reducing the pin height ratio results in the best heat exchanger performance. Not surprisingly, the performance of these arrays closely follows area density.

The degree of performance enhancement can be appreciated by comparing the optimum configuration with the baseline case. For example, at a Reynolds number of only 50, the optimum configuration produced a heat transfer coefficient of nearly 1000 W/m^2K. The baseline configuration required a Reynolds number of 20,000 to provide the same heat transfer performance at a cost of about 300 times the specific fluid friction power. For a 30K temperature difference between cooling air and heat exchanger surface, the optimum configuration would transfer 3 W/cm^2 at Re_{Dh}=50 and 17 W/cm^2 at Re_{Dh} = 1000.

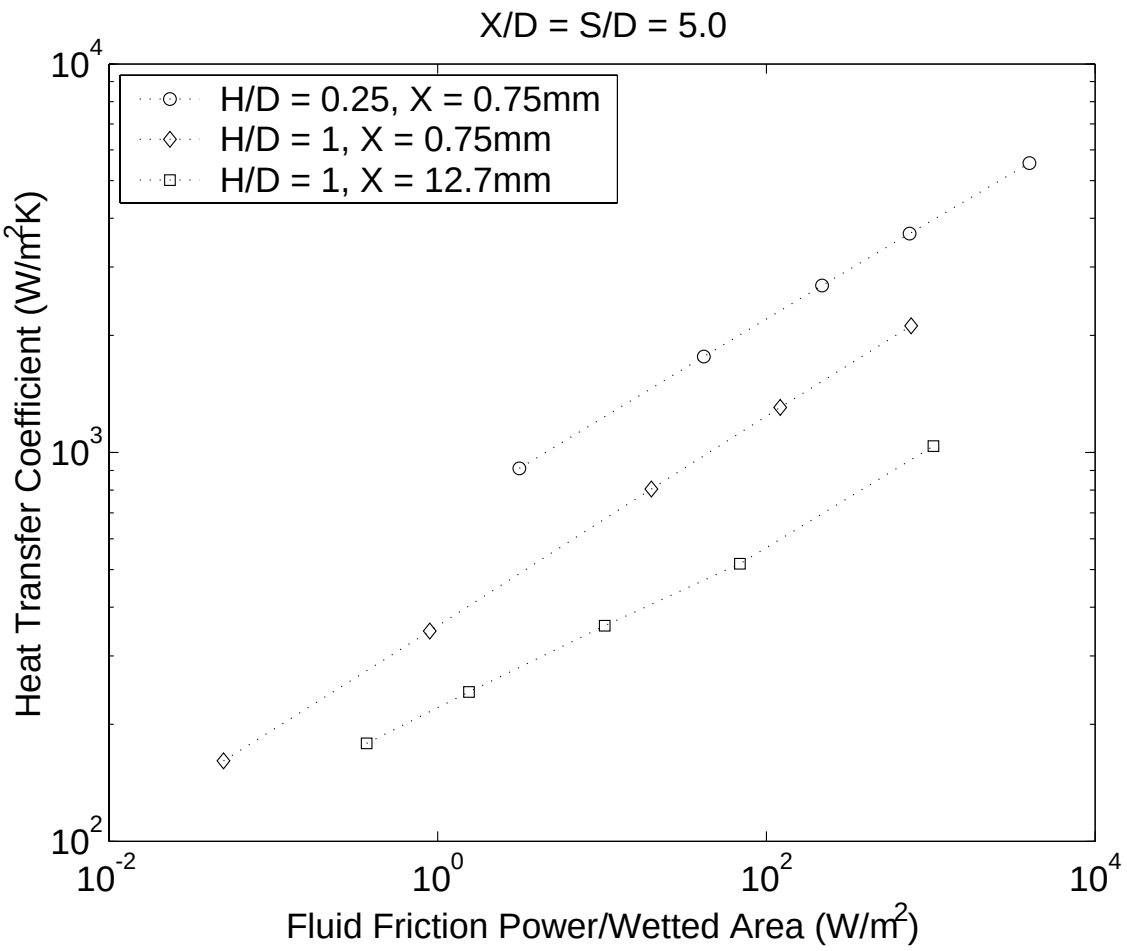

Figure 41 Optimization configuration performance, circular pins

However, the optimum theoretical configuration would have an actual passage height of only 38 μm and would be highly susceptible to particulate contamination. Typically, turbine engine designers use minimum passage diameters of 8 – 12 mils or 0.2 to 0.3 mm to reduce the risk of blockage. Even the intermediate configuration, $H/D = 1$, $X = 0.75$ mm would only have a passage height of 150 μm. With this in mind, the theoretical optimum configuration can be modified to achieve required clearance. With *S/D* and *X/D* held at 5.0, many practical configurations can be defined that all have a minimum clearance value of 0.3 mm. Table 11 shows three of these configurations and their associated area density. These configurations were chosen to take advantage of reducing pin height ratio, axial pitch or a balance of both factors.

Table 11 Practical optimum configuration options, circular pin-fin array

Conf #	X (mm)	H/D	A_w/V (cm^2/cm$^{3)}$
P1	0.75	2.0	73.0
P2	3.0	0.5	66.7
P3	6.0	0.25	65.6

The performance results for these practical configurations are shown in Figure 42. From this chart it is clear that P3 was the best performer among the practical heat exchanger configurations.

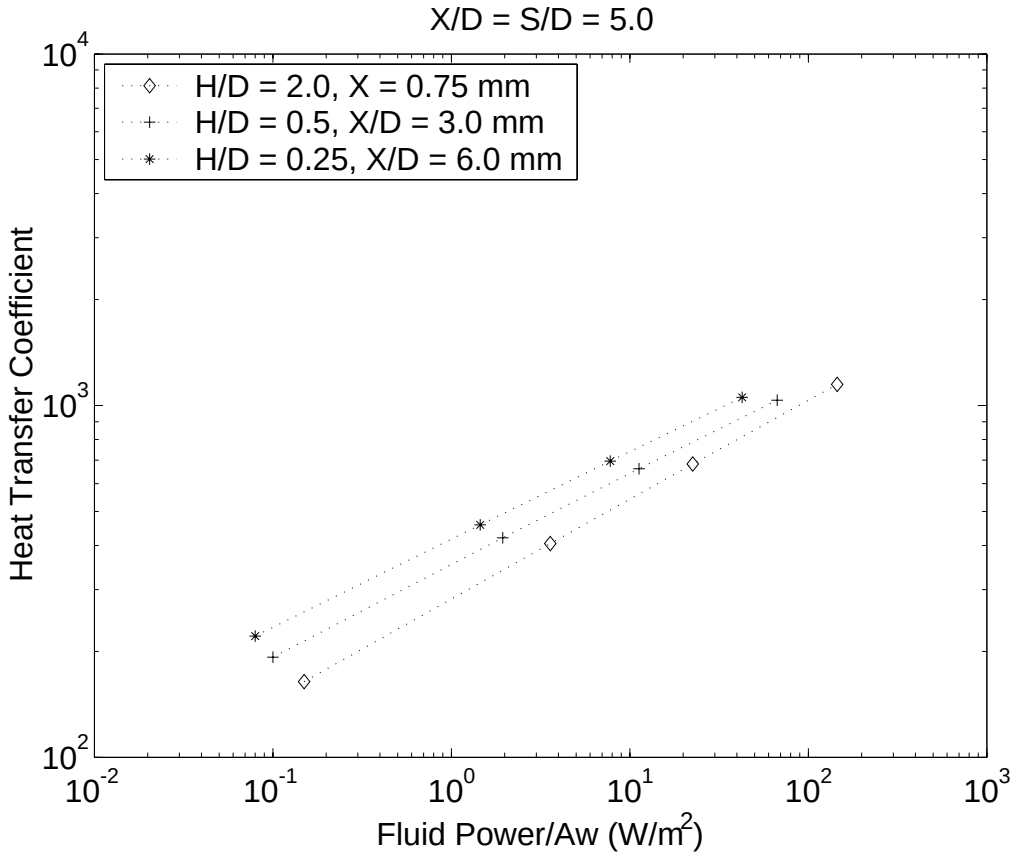

Figure 42 Performance comparison, practical configurations, circular pins

Figure 43 shows a comparison between the best practical configuration and the previously discussed theoretical optimum configuration. The baseline and intermediate configurations are included for reference. It is important to recall that

neither the optimum nor the intermediate configurations were feasible due to susceptibility to particulate contamination.

Despite the size requirement, this optimum practical configuration provided excellent performance from Reynolds numbers ranging from 50 to 2000. On the low end, this configuration had an average heat transfer coefficient of 220 W/m^2K and required 0.08 W/m^2 friction power. At the high end, this configuration produced an average heat transfer coefficient of 1050 W/m^2K and incurred frictional losses of 43 W/m^2. On average the optimum practical configuration required over 40 times less specific friction power to achieve the same heat transfer coefficient values as the baseline configuration.

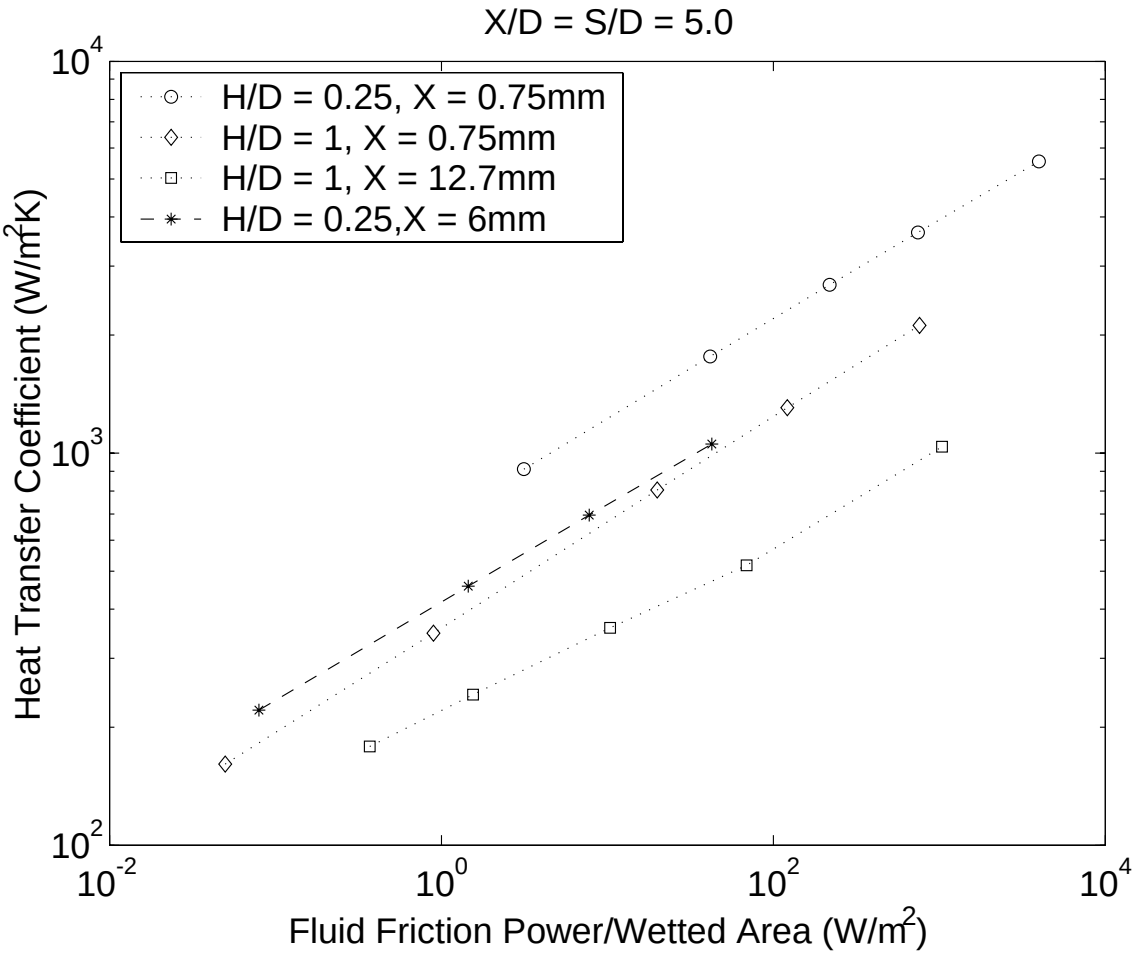

Figure 43 Optimum practical and theoretical configurations, circular pins

3. Conclusions

The objectives of this investigation were met by simulating several pin-fin heat exchanger configurations with various pin height ratios with an experimentally validated three-dimensional finite element model. Specifically:

1. Comprehensive power function correlations were derived to predict Nusselt number and friction factor as a function of Reynolds number, *X/D*, *S/D* and *H/D* for $3,000 \le \mathrm{Re}_{D_h} \le 50,000$.

2. Variations in *H/D* had significant effects on heat exchanger performance. When basing performance on wetted area, reducing *H/D* was found to be most beneficial due to the increase in area density. However, when basing performance on heat exchanger face area or footprint, increasing *H/D* provided considerable improvements over the baseline configurations especially for streamwise and spanwise pin spacing ratios less than five times pin diameter.

3. By combining all factors found to be beneficial in this study, the optimum theoretical configuration was *X/D* = *S/D* = 5.0, *H/D* = 0.25, and *X* = 0.75 mm. Measuring performance on an *h* vs. *E* chart, this configuration was shown to match the heat transfer rate of the baseline case with 300 times less specific energy loss.

4. When considering practical limitations imposed by particulate contamination susceptibility, the best configuration tested was *X/D* = *S/D* = 5.0, *H/D* = 0.25, and *X* = 6 mm. This configuration had heat transfer coefficients ranging from 220 to 1050 W/m^2K over a Reynolds number ranging from 50 to 2000 and resulted in over 40 times less specific energy loss when compared to the baseline case.

D. AIRFOIL-SHAPED PINS

In this section, the heat transfer and pressure drop characteristics of airfoil-shaped pin-fin arrays were investigated using a numerical model. Having thoroughly examined the circular pin configurations, changing pin shape was the next logical step in achieving performance improvement.

1. Numerical Simulation

a. Modeling

The model simulated a staggered pin array with 10 rows of airfoil-shaped pins, but infinitely wide in spanwise extent. As with the circular pin model, this infinite span condition was numerically achieved by placing "symmetry", i.e. zero flux boundaries on both the spanwise edges of the array as shown in Figure 44.

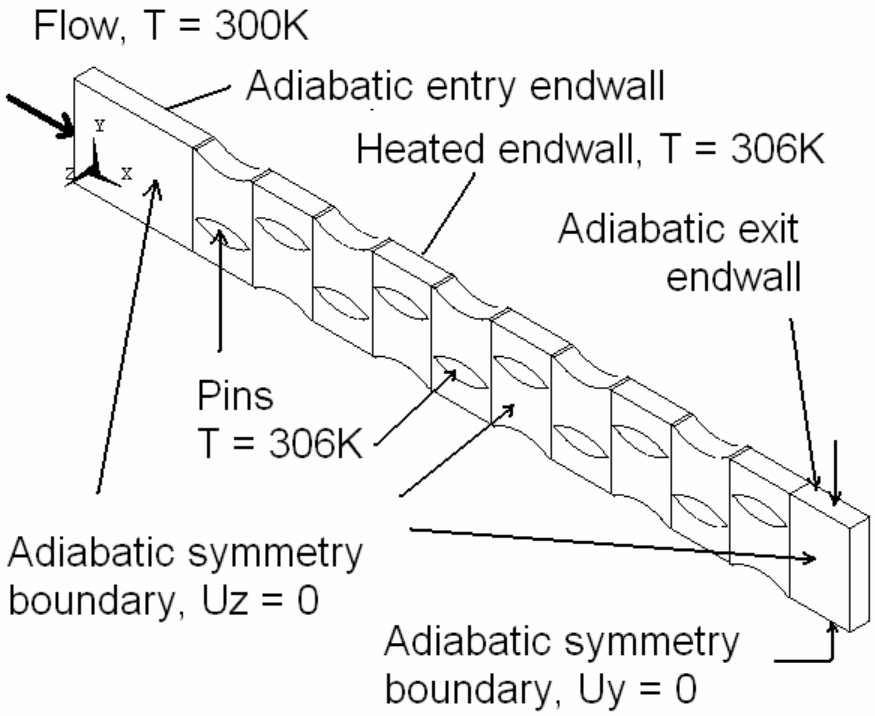

Figure 44 Infinite width numerical model, airfoil-shaped pins

b. Pin Construction Detail

The pins were geometrically defined by the intersection of two circular cylinders as shown in Figure 45. By varying the radius of each circle and controlling center-to center distance, several airfoil geometries were obtained. While these two

specifications were sufficient to fully define the airfoil shapes, additional parameters were used to better characterize the pins as mounted in the test array. These four parameters were spanwise ratio (*S/D*), pin height ratio (*H/D*), length ratio *(LR*) and aspect ratio (*AR*). Figure 46 provides detail on how these parameters are defined. For simplicity, D_y is replaced by *D* for spanwise and pin height ratios.

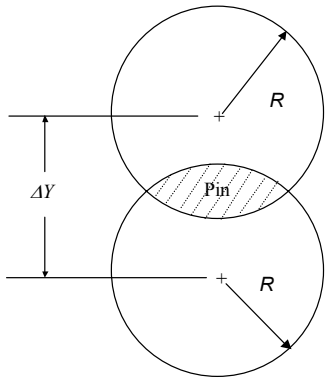

Figure 45 Airfoil construction

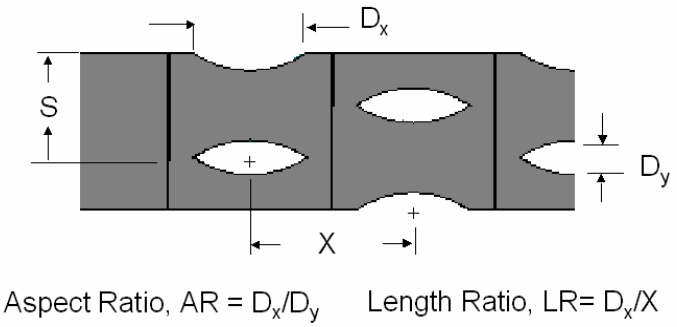

Figure 46 Airfoil-shaped pin dimensions

c. Array Characteristic Length

The hydraulic diameter definition used for the circular pin phase of study was also used for the airfoil-shaped pin-fin array. This was considered to be a useful characteristic length as it would account for differences due to variations in *H/D, LR* and *AR*.

d. Grid Independence

Meshing was carefully specified to ensure maximum coverage in areas of interest such as regions of increased velocity and temperature gradient near the walls as shown in Figure 47. Additionally, mesh density was meticulously scaled to facilitate grid independence studies. The same criteria used to determine grid independence in the circular pin study was applied to the airfoil-shaped pin study. Table 12 provides a representative example of a grid independence check for a given configuration.

Table 12 Airfoil array grid independence, S/D = 3, H/D =1, LR =0.7, AR = 2.0, Re_{Dh} = 5,000

Parameter	Grid 1	Grid 2	Grid 3
x x *y* x z /pin[a]	146/19/11 /13	158/21/13 /14	166x22x15 /15
nodes	94K	135K	163K
Q (W)	1.51	1.52	1.52
T_{out} (K)	305.37	305.40	305.40
$\dot{m}$ (kg/s)	2.81E-04	2.81E-04	2.81E-04

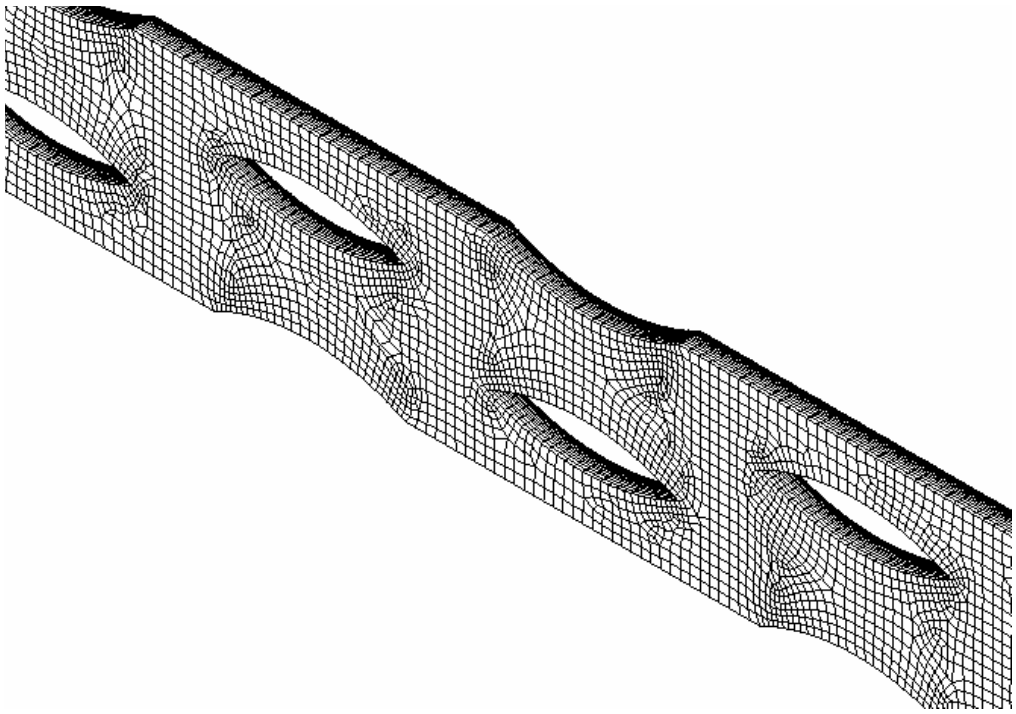

Figure 47 Sample model meshing for airfoil-shaped pin-fin array

2. Test Approach

a. Validation

The numerical model was previously shown to demonstrate satisfactory corroboration with historical experiments for circular pins-fins. While the validity of the numerical model could be extended to the airfoil-shaped pin-fin array based on this corroboration, experiments using actual airfoil-shaped pins were conducted and are discussed in a later section.

b. Test Plan

A parametric study was devised to investigate the effects of the varying *S/D, H/D, LR* and *AR*. In this study, each parameter in turn was varied within the ranges shown in Table 13. When a single parameter was varied, the other three were maintained at nominal values. For each configuration, heat transfer rate and array pressure drop were recorded for Reynolds numbers ranging from 3000 to 20000. Based on the trends observed, theoretically optimum configurations that combined the best of each parameter range were defined and analyzed.

Table 13 Airfoil numerical test configurations

Parameter	Range	Nominal Value
S/D	2 – 5.0	3.0
H/D	1.0 – 4.0	1.0
LR	0.5 – 0.9	0.7
AR	2.4 – 6.2	4.2

3. Results and Discussion

Upon completion of all the test runs, several key performance indicators were examined to understand the heat transfer characteristics and trends for each pin-fin configuration and Reynolds number.

Heat exchanger performance was found to vary significantly as each parameter was varied from nominal values. In the sections that follow, Nusselt number and friction factor are presented to show the effects of each parameter. Additionally, overall heat exchanger performance was evaluated by plotting heat transfer coefficient versus specific fluid friction power on a suitable unit surface area basis.

a. Effects of Varying Spanwise Spacing

The effects of varying *S/D* from 2.0 to 5.0 on heat exchanger performance were investigated during the first phase of the analysis. For each configuration, *H/D* = 1.0, *LR* = 0.7 and *AR* = 4.2.

Figure 48 provides a plot of Nusselt number as a function of Reynolds number for various *S/D* values. From this chart it is clear that Nusselt number can be related to Reynolds number with a power law correlation. Additionally, decreasing *S/D* has a beneficial effect on Nusselt number. However, as shown in Figure 49, friction factor also increases as *S/D* is decreased. Both trends are expected as the decreasing *S/D* provides a more tortuous fluid path and decreased effective flow area.

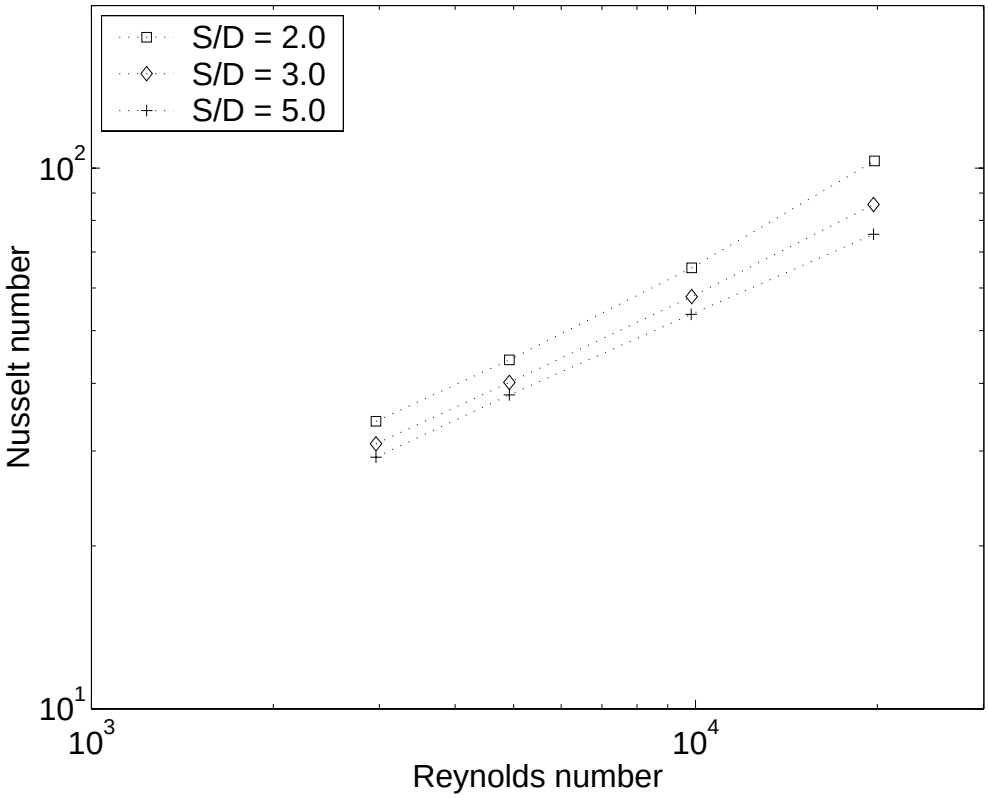

Figure 48 Effect of *S/D* on Nusselt number, airfoil-shaped pins

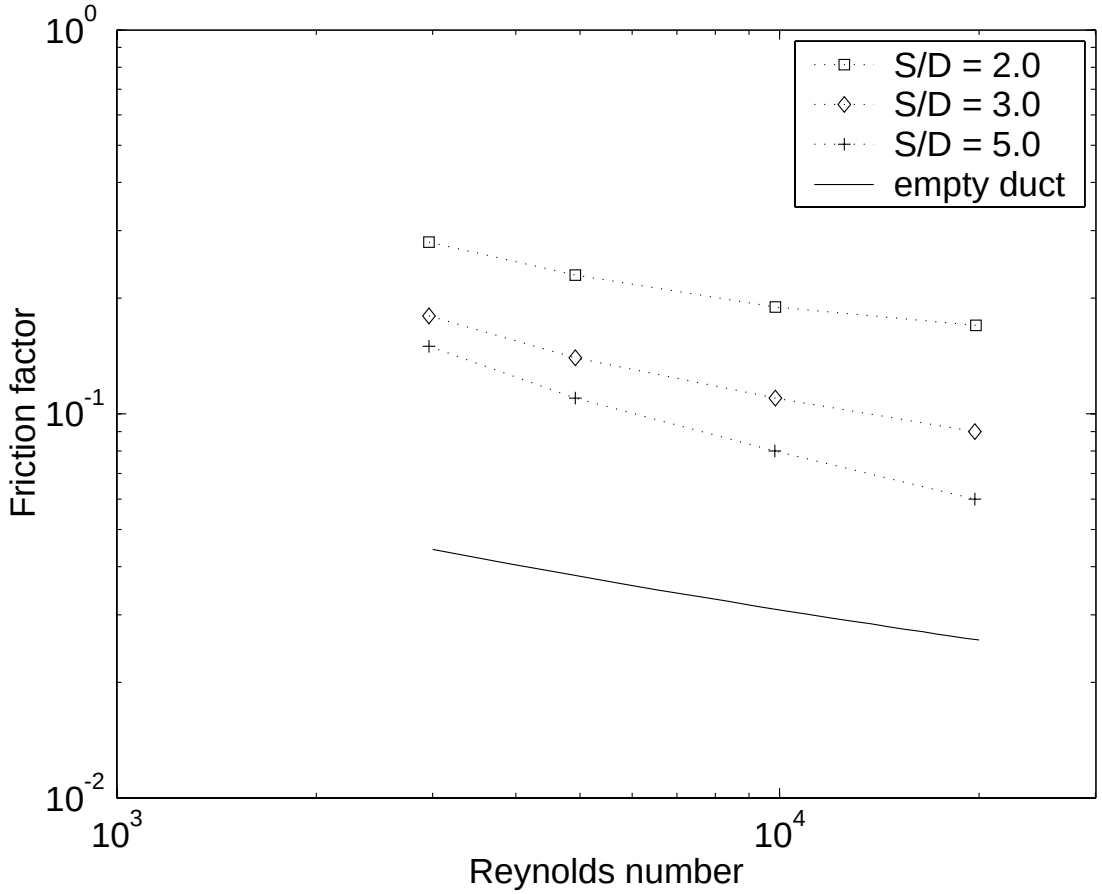

Figure 49 Effect of *S/D* on friction factor, airfoil-shaped pins

By comparing the configurations on an *h* vs. *E* chart as shown in Figure 50, the overall effects of varying *S/D* on heat exchanger performance can be determined. Here it can be seen that a slight increase in performance can be gained by reducing *S/D*. While the advantage is not overwhelming, it highlights the point that increased heat transfer rates associated with smaller *S/D* outweigh the increase in pressure drop.

b. Effects of Varying Pin Height Ratio

Next, the effects of varying *H/D* from 1.0 to 4.0 on heat exchanger performance were studied. For these configurations, *S/D* = 3.0, *LR* = 0.7 and *AR* = 4.2.

Figure 51 shows a plot of Nusselt number versus Reynolds number for various *H/D* configurations. As in the case of variable *S/D*, Nusselt number appears to follow a power law correlation. However, in this case, the effects of varying *H/D* are more subtle than the effects of variable *S/D*. Increasing *H/D* seems to slightly improve

Nusselt number. The benefits however would likely fall within the bounds of experimental uncertainty and are not significant.

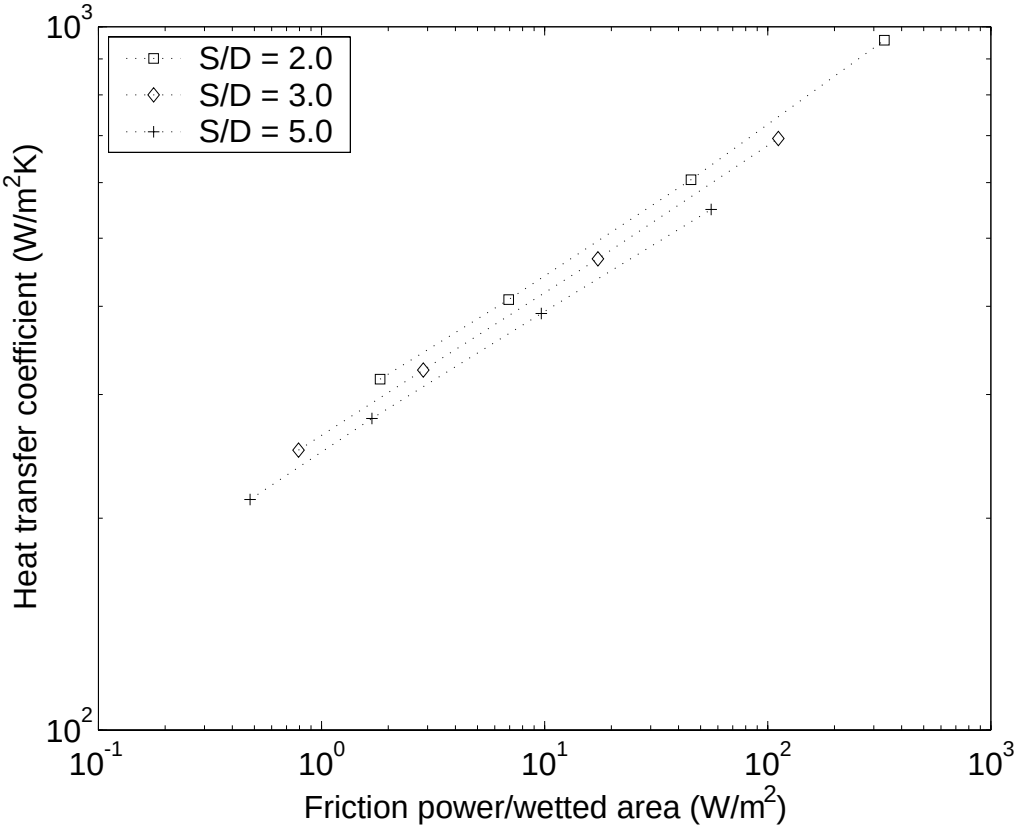

Figure 50 Effects of *S/D* on *h* vs. *E* (wetted area basis), airfoil-shaped pins

On the other hand, friction factor has a much stronger dependence on pin height ratio. As shown in Figure 52, friction factor increases as *H/D* decreases. This trend is mainly due to the geometric differences in the test array. While pressure drop decreased as *H/D* increased, the square of the required average flow velocity to achieve a given Reynolds numbers decreased more rapidly resulting in higher friction factors. This decrease in velocity was due to the increase in hydraulic diameter as *H/D* was increased.

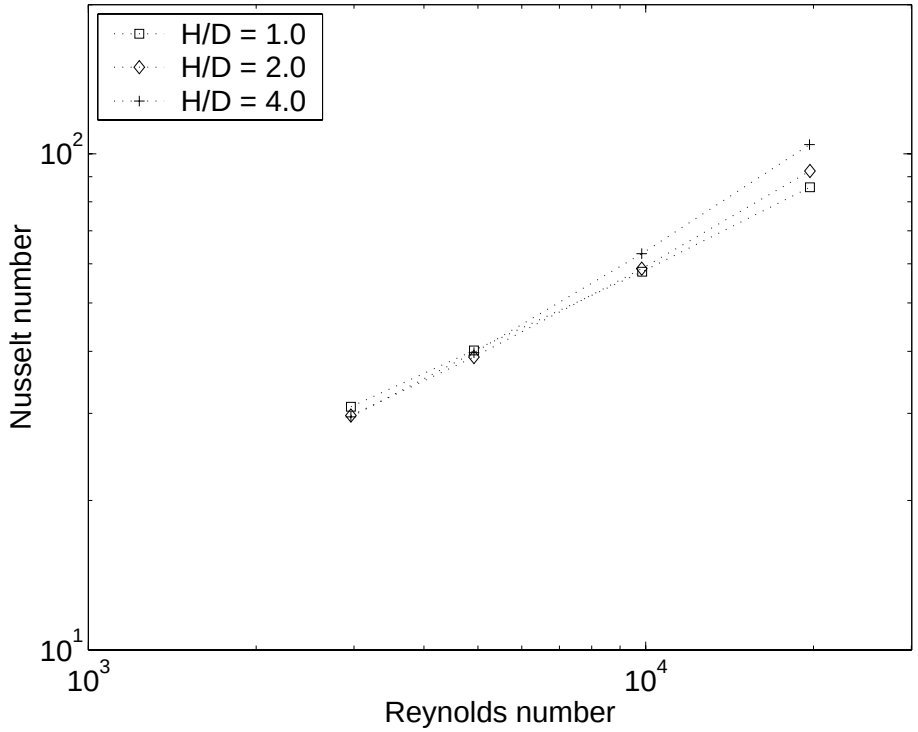

Figure 51 Effects of *H/D* on Nusselt number, airfoil-shaped pins

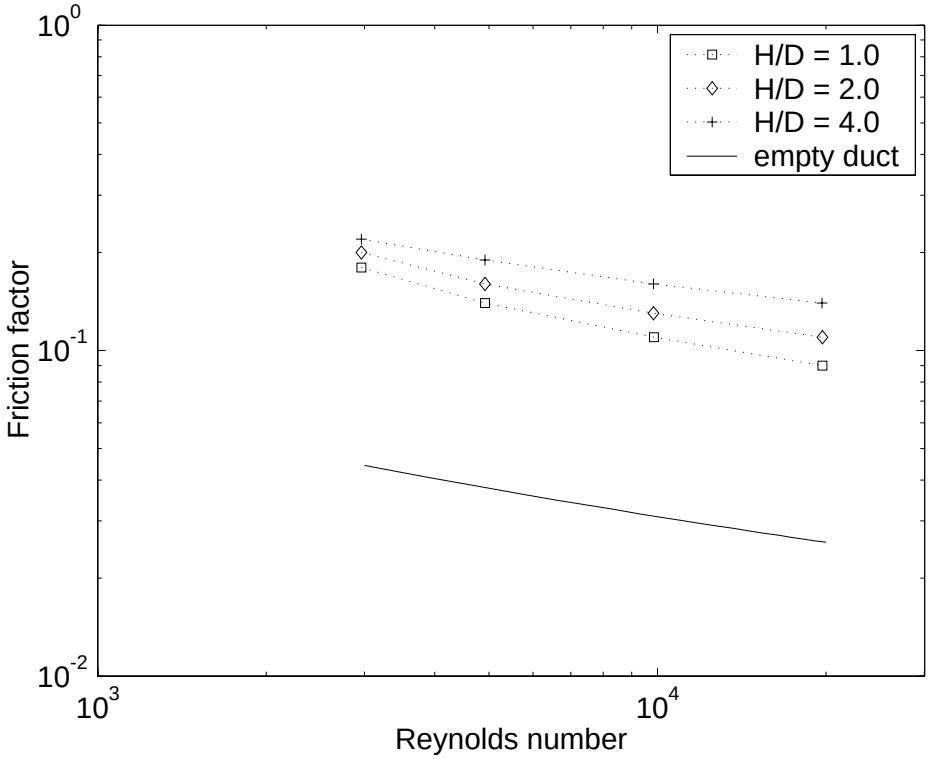

Figure 52 Effects of *H/D* on friction factor, airfoil-shaped pins

In order to evaluate the impact of these trends on overall heat exchanger performance, an *h* vs. *E* chart is shown in Figure 53. When based on wetted area, performance is seen to improve as *H/D* is decreased. However, when based on face area as shown in Figure 54, an opposite trend is observed. In this case, performance is better for higher pin ratios. This enhancement is mainly due to the increased surface area provided by the longer pins and the reduced impact on pin heat transfer coefficient due to endwall effects. The greater heat rate must be transferred through the heat exchanger endwall face. In theory, longer pins would provide even more performance. However, due to manufacturing and operating constraints, pin height ratios greater than 4.0 are not considered representative of cooling schemes employed in turbine blades.

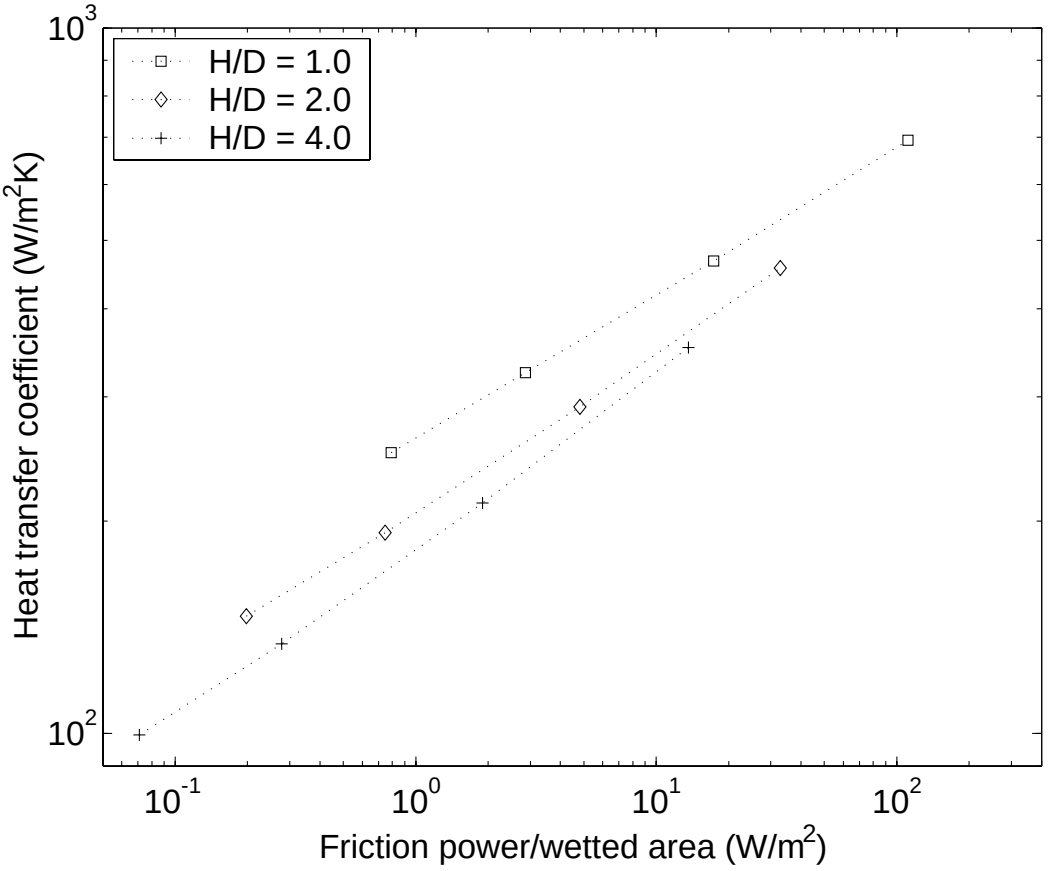

Figure 53 Effect of *H/D* on *h* vs. *E* (wetted area basis), airfoil-shaped pins

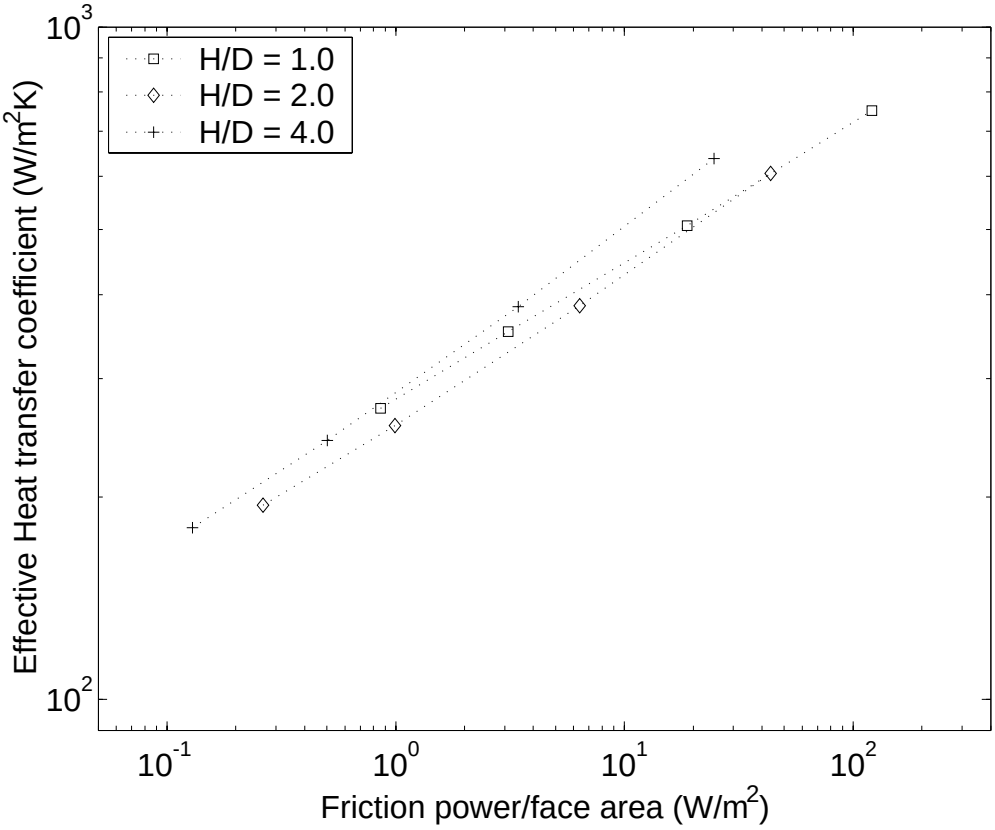

Figure 54 Effect of *H/D* on *h* vs. *E* (face area basis), airfoil-shaped pins

c. Effects of Varying Pin-fin Length Ratio

The effects of varying *LR* from 0.5 to 0.9 on heat exchanger performance were examined. For each configuration, *S/D* = 3.0, *H/D* = 1.0 and *AR* = 4.2.

Figure 55 and Figure 56 show plots of Nusselt number and friction factor versus Reynolds number for various pin length ratios. Showing consistent and orderly trends, both Nusselt number and friction factor increase as *LR* is decreased. As before, these effects are mainly due to changes in average flow velocity required to achieve desired Reynolds number. As length ratio decreases, hydraulic diameter also decreases resulting in higher average velocity. Also, pressure drop increases more rapidly than the square of the velocity. Thus, the friction factor tends to increase.

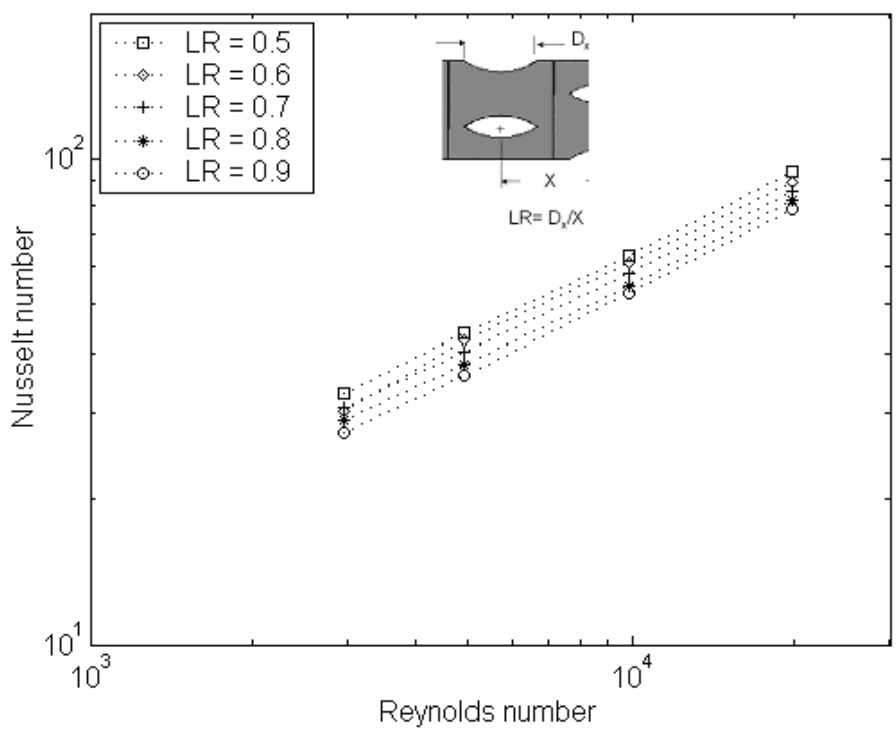

Figure 55 Effects of length ratio on Nusselt number, airfoil-shaped pins

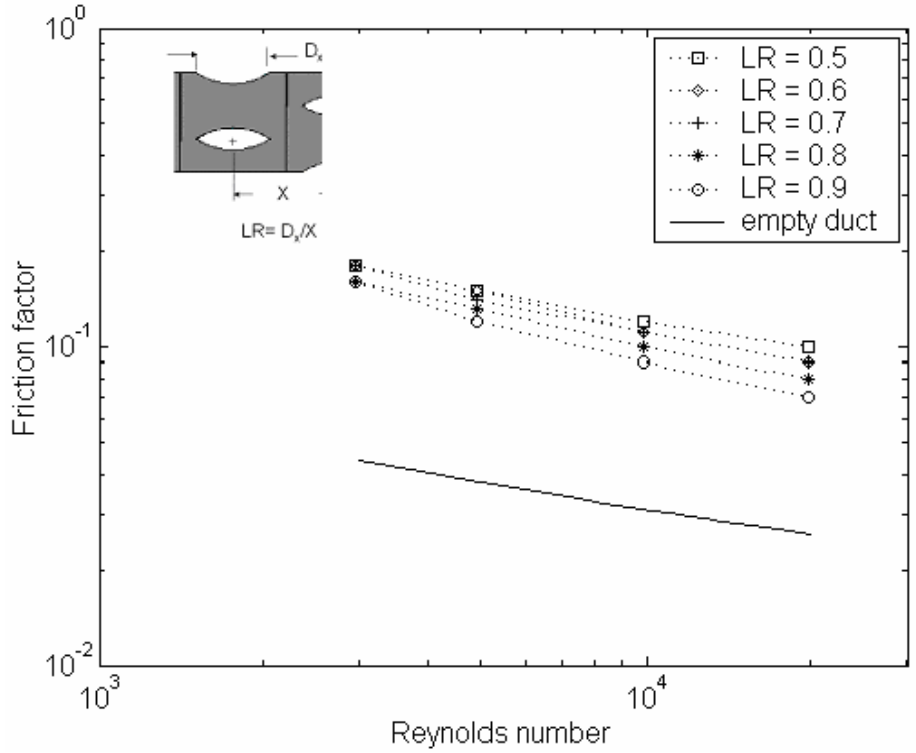

Figure 56 Effect of length ratio on friction factor, airfoil-shaped pins

The overall effect of *LR* on heat exchanger performance is realized by examining the *h* vs. *E* plot shown in Figure 57. From this chart it is evident that the increase in heat transfer rate outweighs the increases in pressure drop as *LR* is reduced. Thus reducing pin length ratio improves heat exchanger performance.

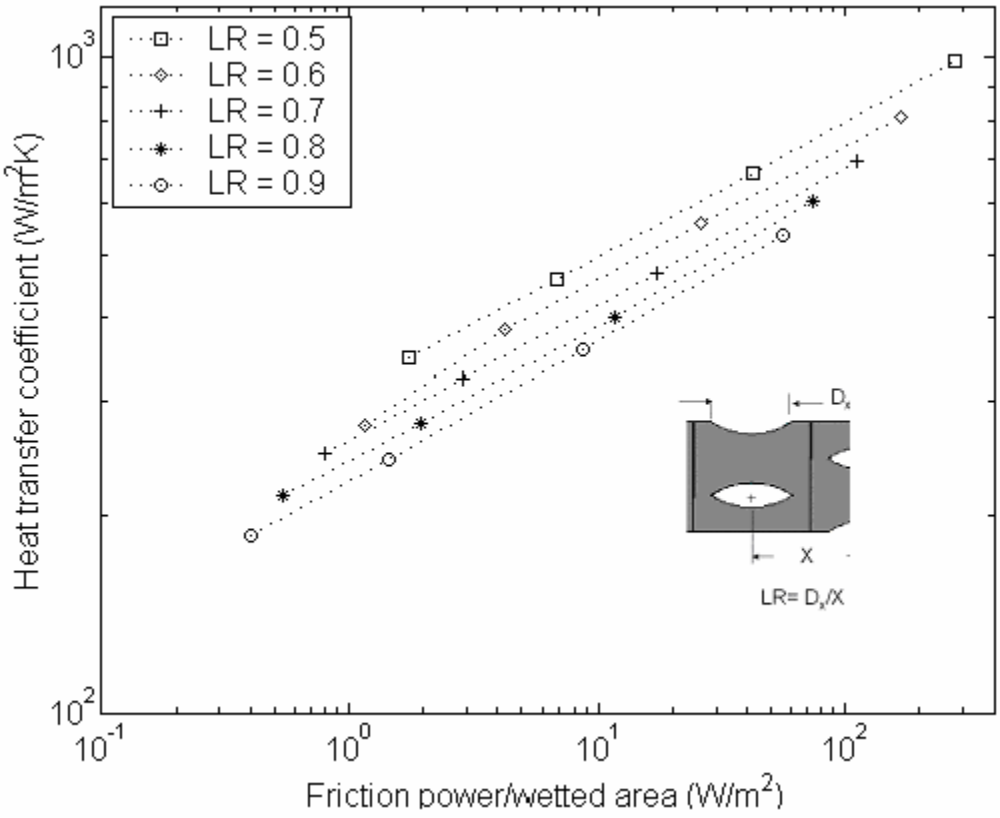

Figure 57 Effect of length ratio on *h* vs. *E* (wetted area basis), airfoil-shaped pins

d. Effects of Varying Pin-fin Aspect Ratio

Finally, the effects of varying aspect ratio from 2.4 to 6.2 on the performance of the heat exchanger were investigated. For these configurations, *S/D* = 3.0, *H/D* = 1.0 and *LR* = 0.7.

Figure 58 shows a plot of Nusselt number versus Reynolds number for each *AR* variation tested. Interestingly, there is no significant effect on Nusselt number as *AR* is changed. In these cases, the array averaged heat transfer coefficient increases as *AR* increases but is offset by hydraulic diameter which decreases at the same rate. Friction factor, on the other hand, is heavily dependent on *AR*. From Figure 59, it is clear

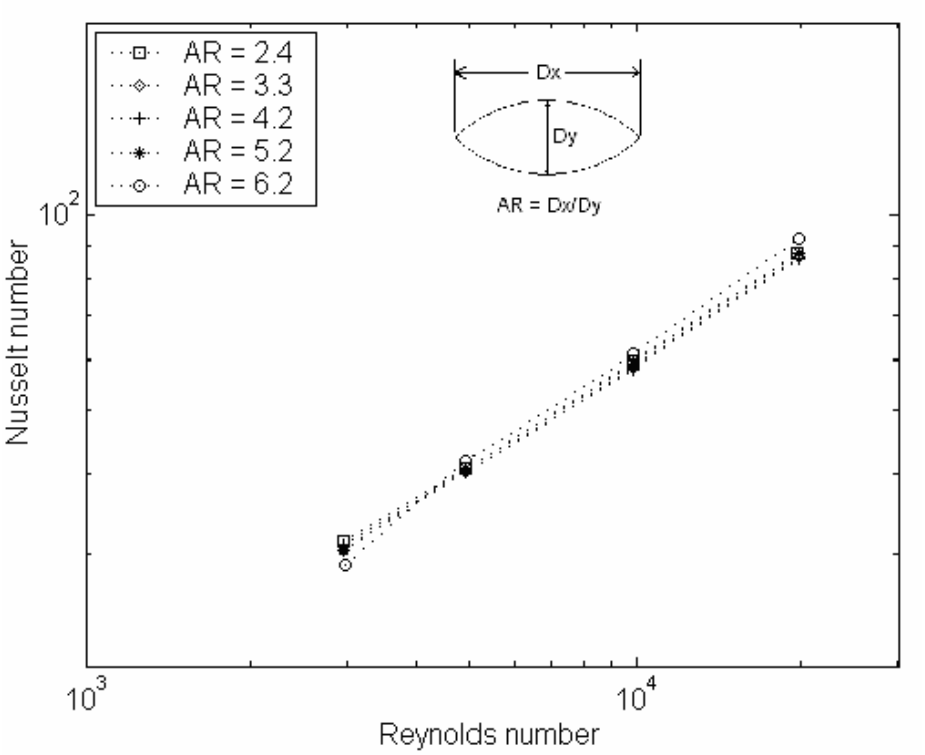

Figure 58 Effects of aspect ratio on Nusselt number, airfoil-shaped pins

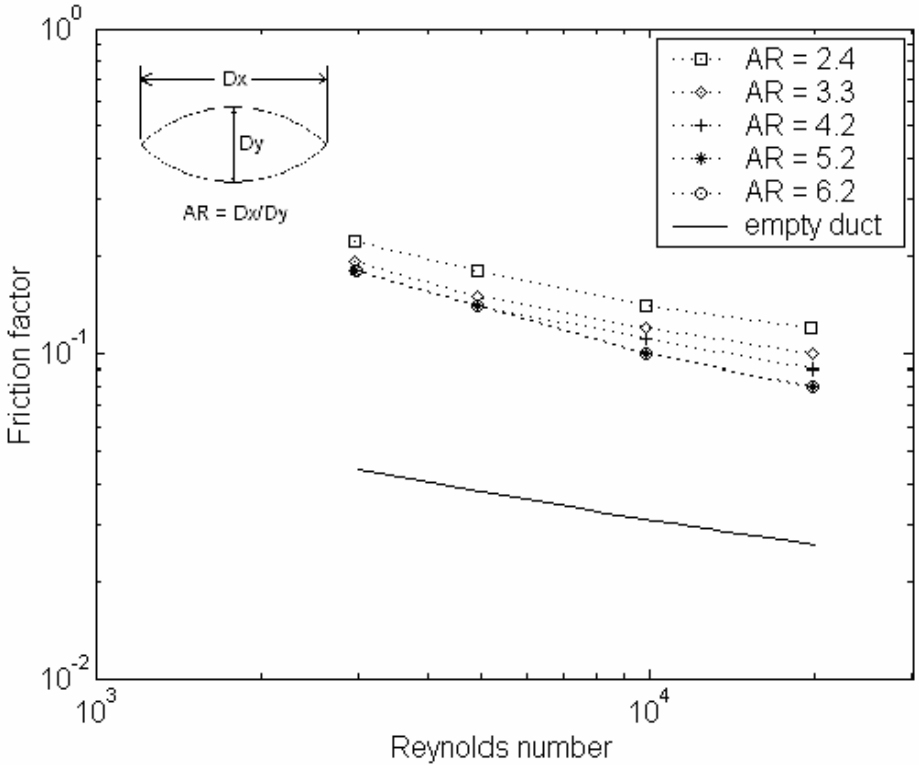

Figure 59 Effects of aspect ratio on friction factor, airfoil-shaped pins

that friction factor decreases as aspect ratio increases. As increased aspect ratio gives the pins a sleeker appearance relative to the flow direction, this reduction in friction factor is expected. As aspect ratio is increased, flow separation is reduced and overall pressure drop is dramatically decreased.

Figure 60 provides a plot of *h* vs. *E* for the variable *AR* ratio runs. It confirms the expectation that the sleeker or higher aspect ratio pins provide improved performance when compared to low aspect ratio pins.

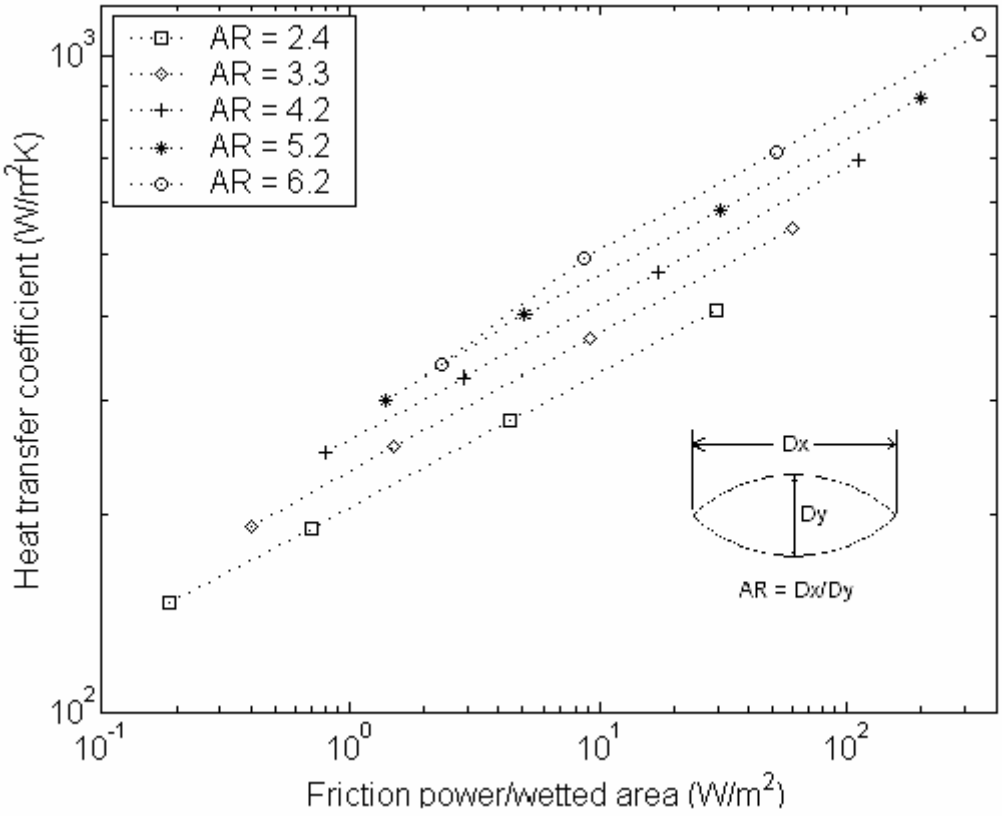

Figure 60 Effect of aspect ratio on *h* vs. *E* (wetted area basis), airfoil-shaped pins

In summary, the four basic defining parameters had a significant effect on heat exchanger performance. Decreasing *S/D, H/D, LR* and increasing *AR* were all beneficial with respect to performance based on wetted area. For performance based on face area, the only difference was that increasing *H/D* was most beneficial. Interestingly, these trends can be linked to changes in area density, that is, surface area per unit volume. Figure 61 shows the effect on area density as each of the four parameters was

independently varied from the baseline configuration. It can be observed that trends in heat exchanger performance directly follow area density. Note that area density, like performance, increases as *S/D, H/D* and *LR* are reduced. Conversely, area density and heat exchanger performance increase as *AR* increases. This linkage can provide helpful clues to the heat exchanger designer for preliminary development phases.

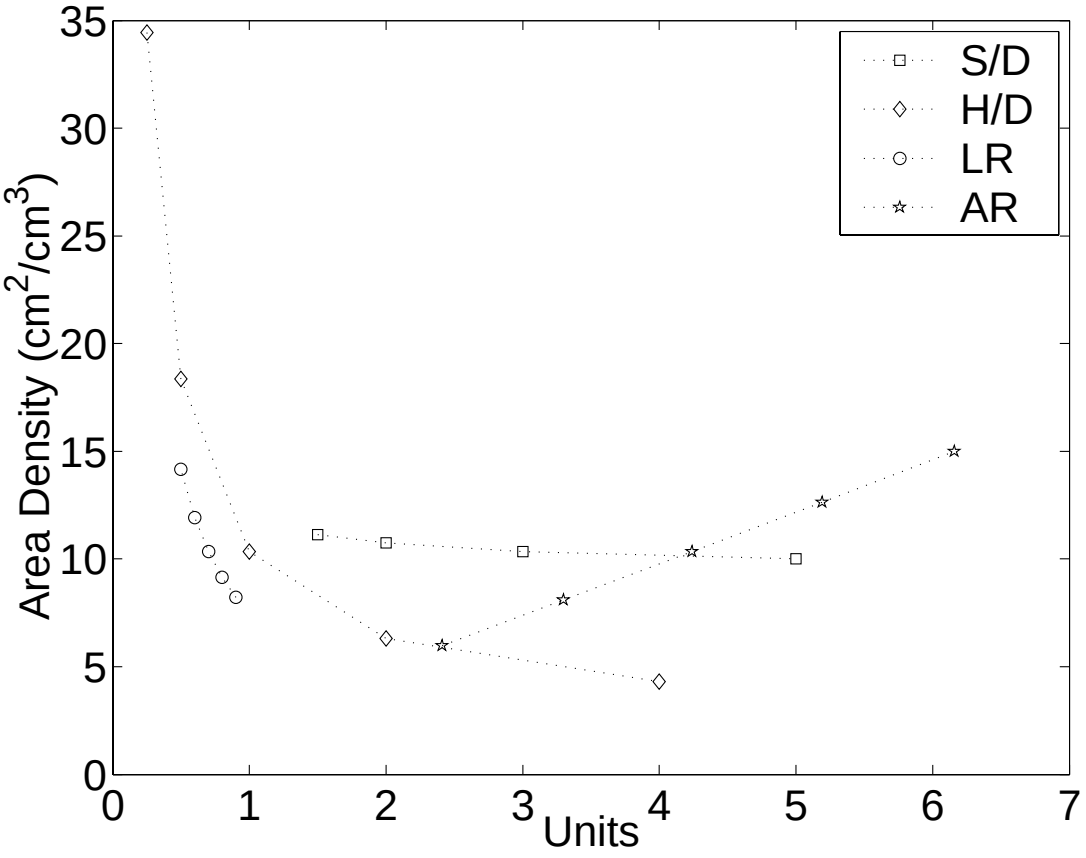

Figure 61 Area density trends for airfoil-shaped pin-fin arrays

Taking advantage of observed performance trends for each of the four defining parameters, it is possible to predict the configuration of an optimum heat exchanger within the limits of the test matrix. Such a heat exchanger would have *S/D* = 2.0, *LR* = 0.5 and *AR* = 6.2. Depending on whether performance was based on wetted area or face area would dictate the selection of *H/D*. For wetted area basis, minimizing *H/D* would be most beneficial whereas for face area basis, maximum *H/D* would be selected.

e. Size Effects

Taking the development one step further, the optimum configuration can be further improved by taking advantage of scale. Figure 62 and Figure 63 show that Nusselt number and friction factor are essentially independent of array size. This is important for two reasons. First, as hydraulic diameter is reduced, heat transfer coefficient must increase to maintain Nusselt number. Thus heat transfer rates can be enhanced by decreasing the axial pitch of an array. Secondly, the results obtained when testing macroscale heat exchanger arrays can be directly applied to microscale designs.

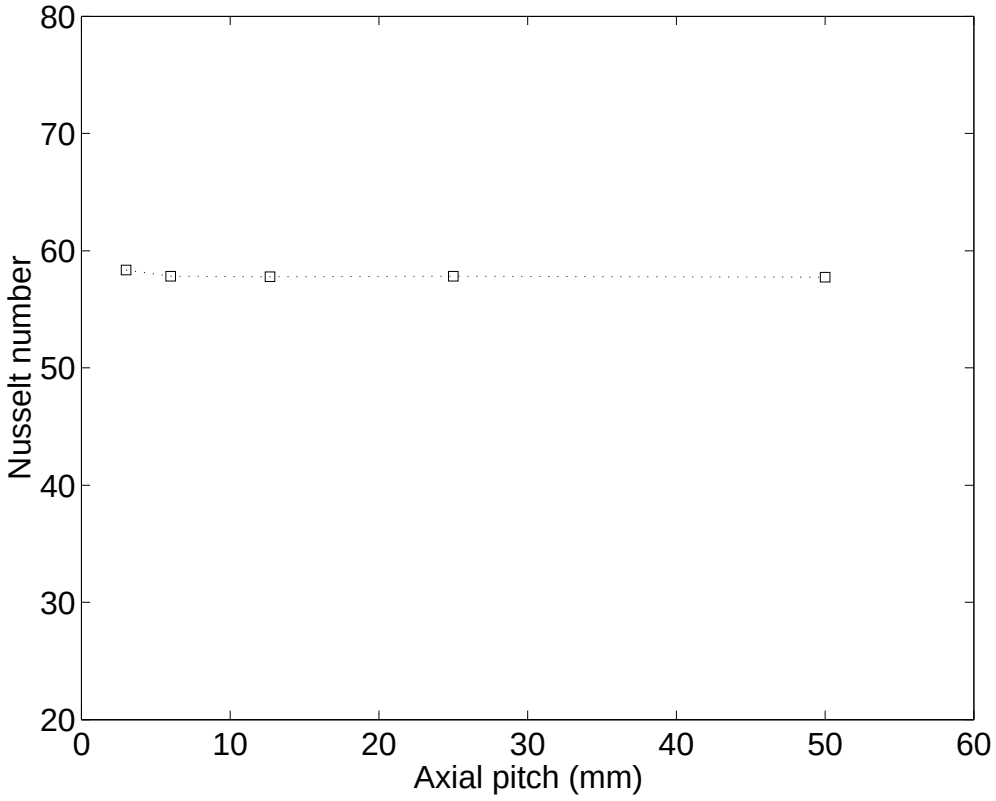

Figure 62 Effect of axial pitch on Nusselt number, airfoil-shaped pins

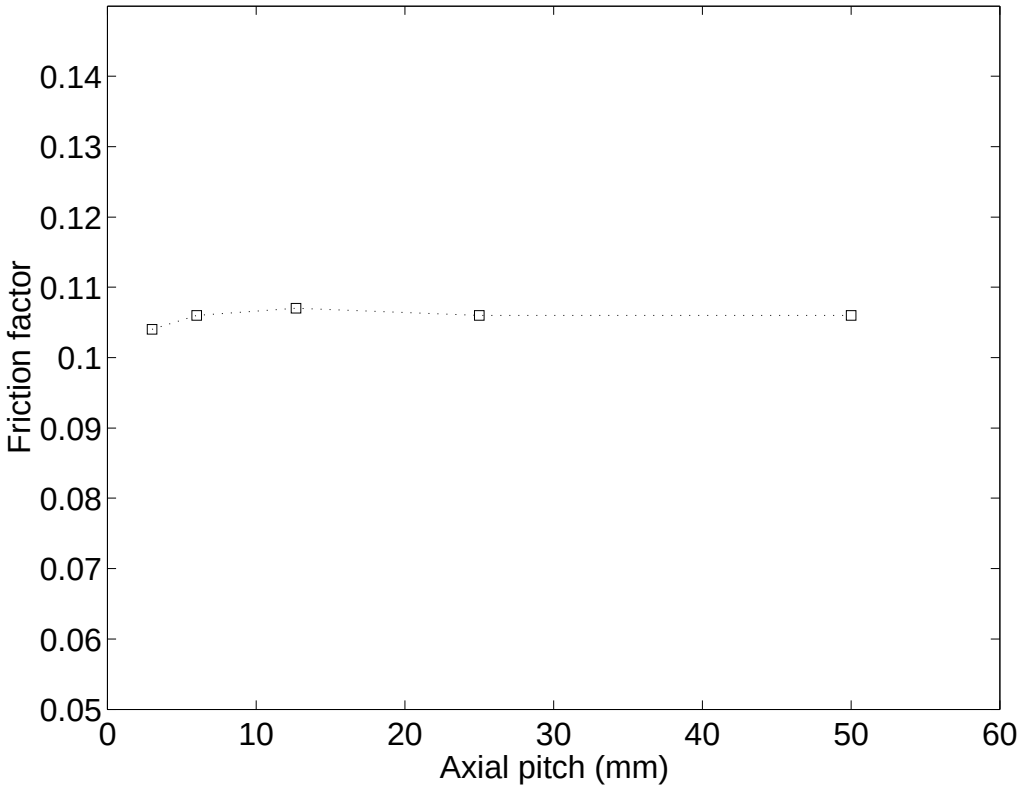

Figure 63 Effect of axial pitch on friction factor, airfoil-shaped pins

f. Optimization

While size reductions improve heat transfer rate, heat exchanger dimensions must include practical limits. Typically, turbine blade designers use a minimum passage size of 8 – 12 mils to prevent clogging from airborne particles. Using a minimum clearance of 0.3 mm one feasible configuration was $S/D = 2$, $H/D = 1$, $LR = 0.5$ and $AR = 6.2$ with an axial pitch of 3.75 mm. Area density for this configuration was 71.5 cm^2/cm^3. For this configuration, both passage height and interpin clearance was 0.3 mm. Another possible configuration would be $S/D = 2$, $H/D = 0.5$, $LR = 0.5$ and $AR = 6.2$ with an axial pitch of 7.5 mm yielding an area density of 63 cm^2/cm^3. To improve performance on a face area basis, the H/D could be raised to 4.0 for either case. Numerical simulations indicated that both configurations had nearly identical performance. Figure 64 shows an h vs. E plot for an optimum configuration based on wetted area. For the sake of comparison, a theoretical worst case, $S/D = 5$, $H/D = 4$, $LR = 0.9$ and $AR = 2.4$ is plotted to demonstrate the impact of a poor design. Finally, the

optimum and worst-case circular pin configurations from the previous section are included to illustrate the advantage gained by switching to the airfoil-shaped pins.

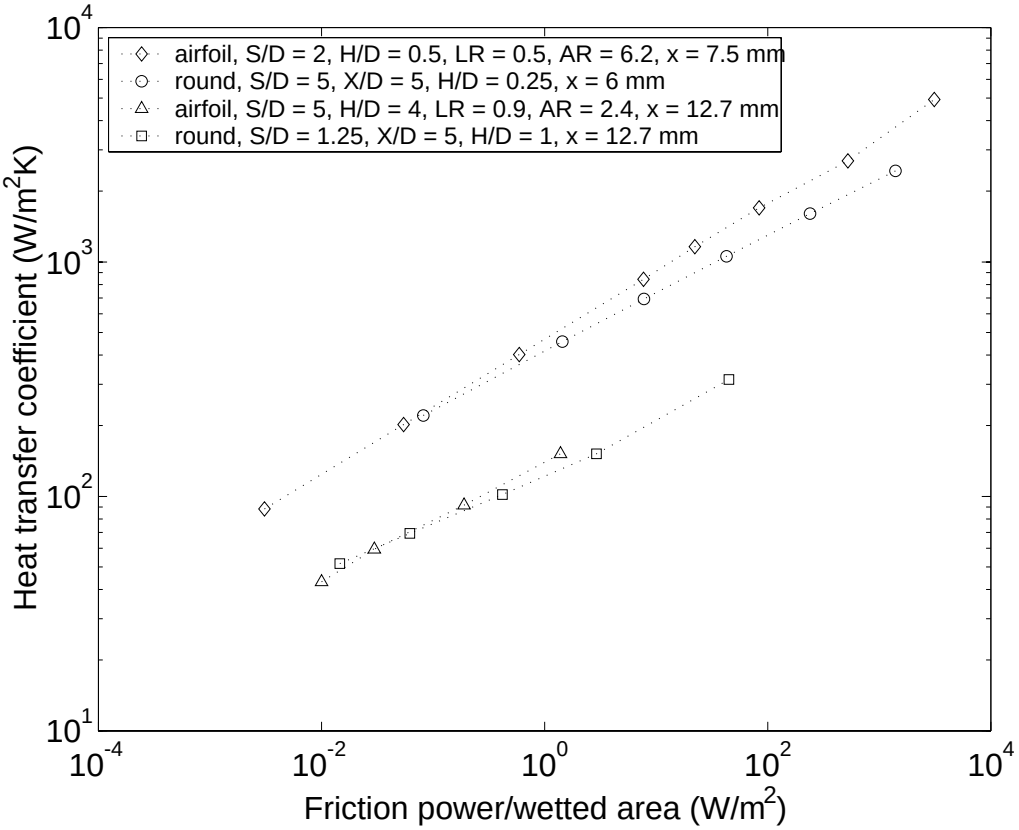

Figure 64 Optimum configuration comparison, airfoil-shaped pins vs. circular pins

Note that in both the best and worst cases, the airfoil-shaped pins provide greater performance advantage as Reynolds number is increased. This is likely due to the increased importance of the airfoil shape at higher Reynolds number. Figure 65 shows numerically obtained streamline plots for both the airfoil and circularly shaped pins. Both pins were in the second row of an array for operating at a Reynolds number of 20,000. The airfoil shape tends to minimize boundary layer separation thereby reducing pressure drag when compared to circular pins. Since the pressure drag on the pins increases proportionally to the square of the flow velocity, the difference in friction power associated with the circular pins grows exponentially.

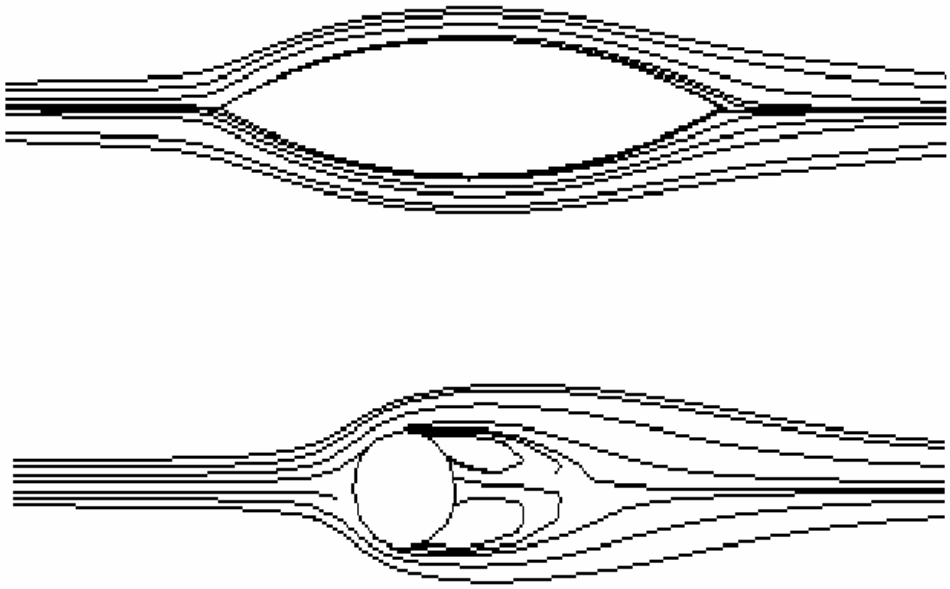

Figure 65 Numerical pin-fin streamline comparison, Re_{Dh} = 20,000

In addition to reducing pressure drag, the delayed boundary layer separation on the airfoil-shaped pins also provides a heat transfer advantage. Figure 66 shows a numerically generated comparison of normalized heat transfer coefficient on the surface of an airfoil-shaped pin and a circular pin. Note that the heat transfer coefficient drops off rapidly on the circular pin as the flow approaches 90 degrees on either side of pin. In contrast, the heat transfer coefficient on the airfoil-shaped pin maintains a higher value for an additional 30 – 40 degrees. Note also that the normalized heat transfer coefficient on the leading edge of the airfoil is significantly greater than it is for the circular pin. The actual value in this case was nearly 22 times the average heat transfer coefficient on the pin. This was likely due to the sharp leading edge. In this region, the boundary layer is extremely thin while the flow velocity is very high. These factors combine to yield extremely high local heat transfer coefficients. The graph was not scaled to include this portion in order to ensure adequate resolution for characterization of the separation point.

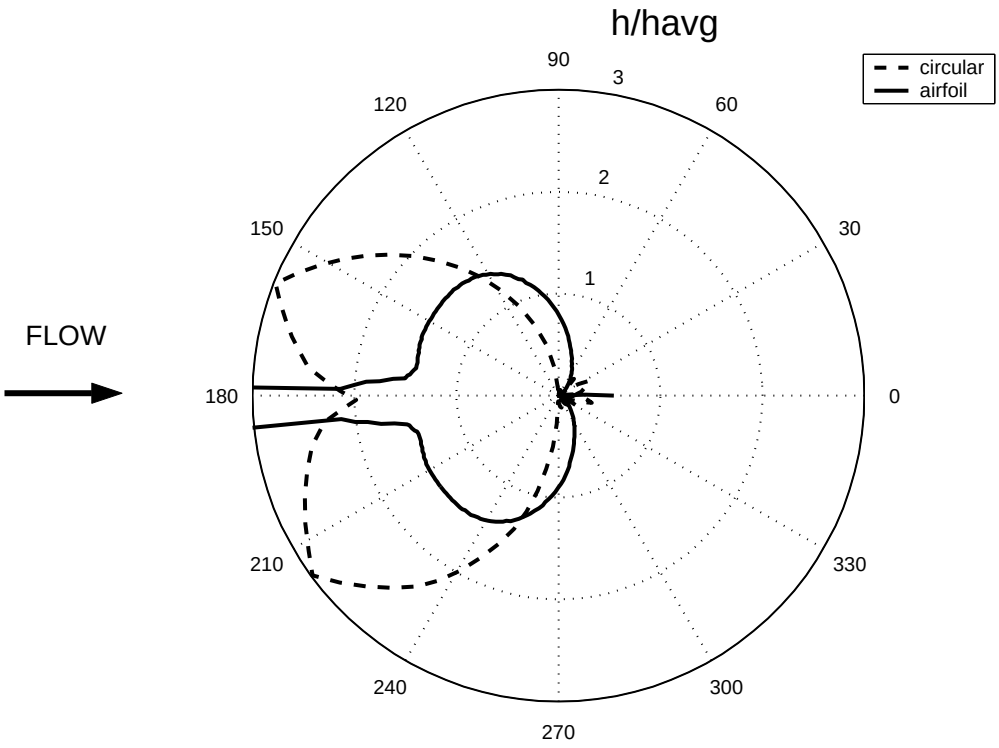

Figure 66 Local heat transfer coefficient comparison

The advantage gained by switching to the airfoil shape can be realized by comparing the frictional losses between the two optimum configurations of each pin shape for a desired heat transfer coefficient. Table 14 displays the comparison between the optimum airfoil-shaped pin array and the optimal circular pin-fin array that was defined as $S/D = 5$, $X/D = 5$, $H/D = 0.25$ and $X = 6$ mm. With an area density of 65.6 cm^2/cm^3, the circular pin-fin array closely matched the scale of the airfoil-shaped pin array. The second column in the table shows the heat transfer coefficient produced by both configurations. Finally the specific fluid friction power required by each configuration is compared. In all cases, the airfoil-shaped pin array requires less power to produce the desired heat transfer coefficient. Additionally, the relative gains afforded by the airfoil design increase at higher Reynolds number. Over the range tested, the advantage of switching to the airfoil shapes varies from 15 to 71%. At the highest

Reynolds number used in this comparison, the circular pin-fin array requires more than three times the fluid power to produce the same heat transfer coefficient as the airfoil-shaped pin array.

Table 14 Performance comparison between circular and airfoil-shaped pin-fin arrays

Re_{Dh} (airfoil)	h (W/m^{2}K)	$E_{circular}$ (W/m^2)	$E_{airfoil}$(W/m^2)	% decrease in E
330	220	0.082	0.070	15
900	450	1.45	0.085	41
1500	700	7.79	3.97	49
2700	1050	42.8	16.9	60
4650	1600	241	70.7	71

4. Conclusions

The objectives of this investigation were met by simulating various airfoil-shaped pin-fin heat exchanger configurations with an experimentally validated three-dimensional finite element model. The performance of the airfoil-shaped pin-fin array was found to be superior when compared to similarly scaled circular pin-fin arrays. This performance increase was mainly due to the streamlined nature of the airfoil shape which was shown to delay flow separation from the pins in the array. This not only reduced pressure drag, but also increased effective heat transfer surface area on the airfoil-shaped pins.

Four defining parameters of the airfoil-shaped pins, span wise width ratio, pin height ratio, pin length ratio and aspect ratio were varied with a numerical model and the effects on heat transfer and pressure drop were explored. The effects of these variations tended to follow basic geometric principles. That is, parameter changes that increased the area density of an array enhanced overall performance based on heat transfer coefficient and fluid friction power when compared to those changes that reduced area density. Specifically:

1. Decreasing *S/D* was found to increase both Nusselt number and friction

factor over the entire Reynolds number range tested. Although friction factor was increased, overall performance was enhanced by reducing span wise pin ratio.

2. Increasing *H/D* was found to have little effect on Nusselt number but significantly increased friction factor. The increase in friction factor was due to the geometry change as pin height ratio increased. That is, increasing *H/D* caused hydraulic diameter to increase significantly thereby reducing average velocity requirement for a given Reynolds number. Thus friction factor increased. The overall impact of changes in *H/D* depended on whether wetted area or face area was used as a performance basis. Reducing *H/D* improved performance on a wetted area basis. Conversely, increasing *H/D* enhanced performance based on face area which may be important for cooling electronic components.

3. As in the case of pin height ratio, changes in pin length ratio significantly affected hydraulic diameter and thus affected Nusselt number and friction factor. Reducing length ratio increased both Nusselt number and friction factor. Overall performance was also enhanced when length ratio was reduced.

4. Pin aspect ratio was the only parameter that had an opposite effect on area density and overall performance. When aspect ratio was increased, friction factor was reduced as the pins became more streamlined. No significant changes occurred in Nusselt number so overall performance was improved as aspect ratio was increased.

5. By combining the factors shown to improve performance into one design, an optimum configuration was developed. Sized to resist particulate contamination, the optimum configuration was S/D =2, H/D = 0.5, LR = 0.5, AR = 6.3 and X = 6 mm. Compared to a circular pin configuration with approximately the same area density, the airfoil-shaped pin-fin array much lower frictional losses to maintain a given heat transfer coefficient. The advantage of the airfoil-shaped pin array grew from 15 to 71% as Reynolds number was increased from 330 to 4650.

III. EXPERIMENTAL ANALYSIS

A. OVERVIEW

This section covers the experimental testing completed to support the numerical analysis presented in the previous sections. Up to this point, the numerical model had only been validated against historical data from Metzger et al. (Ref. 5) and Arora (Ref. 11). Based on these comparisons, the model was found to be in excellent agreement with experimental heat transfer data. Friction factor predictions were not as accurate but were considered useful for determining trends between various pin-fin array configurations. No experimental data were available to validate the airfoil-shaped pins. In this section, experimental testing of three circular and one airfoil-shaped pin-fin array will be discussed.

B. EXPERIMENTAL SETUP

1. Experimental Apparatus

The experimental rig consisted of a rectangular entrance duct, pin-fin test array, mixing chamber and exit duct. Airflow was driven by a two-stage regenerative blower mounted at the end of the exit duct. A schematic of the test apparatus layout is shown in Figure 67.

The entrance duct was constructed of plexiglass and measured three meters in length to ensure a fully developed velocity profile at the test section. The inner dimensions of the duct were 33 mm x 250 mm to match the test section. The duct was open to ambient air and was fitted with a screen to prevent debris from entering the test section and fouling the downstream blower. All duct joints were carefully constructed to maintain airtight integrity and present a smooth surface to the incoming air thereby preventing flow disturbances.

The test section was comprised of 10 separate sections of pins. Figure 68 shows test section construction detail. Each section or row consisted of aluminum pin-fins mounted with screws between two aluminum plates material measuring 12 mm x 50 mm x 250 mm.. Each section was thermally insulated from the adjacent section by 1 mm plexiglass strips to facilitate independent row-by-row heat transfer analysis. The adiabatic sidewalls were made of 12 mm thick plexiglass and permitted excellent

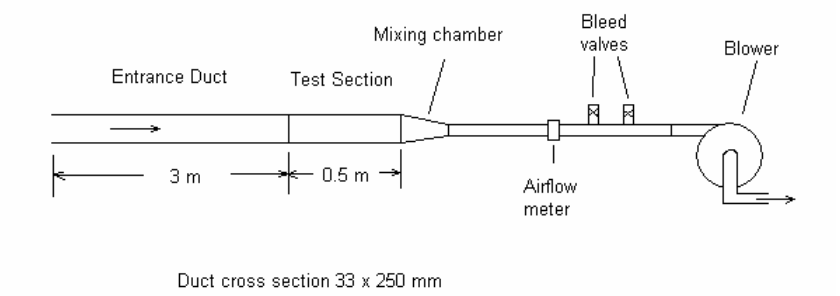

Figure 67 Experimental apparatus schematic

visibility into the test array. As with the entrance duct, care was taken to minimize flow disturbances caused by uneven endwall alignment. Additionally, rubber gasket material was used in all joints to prevent air leaks in the test array. Using a smoke generator, all leaks were revealed and subsequently corrected before testing was conducted.

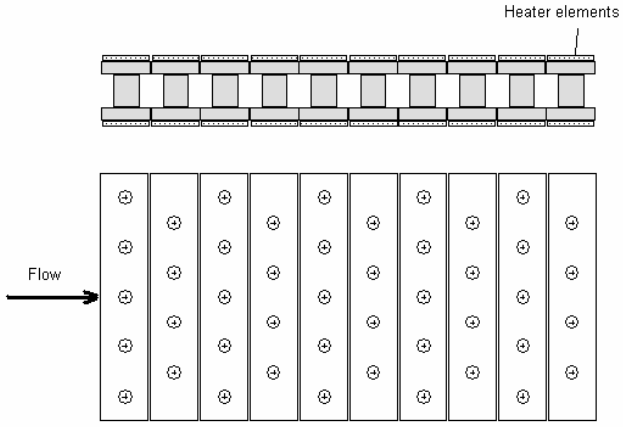

Figure 68 Test section detailed diagram

For some of the testing, two different mechanical turbulence generators were installed immediately prior to the test section. One consisted of wide metallic strips and the other was a standard screen mesh. Figure 69 shows photographs of these generators.

Flexible electric heating elements were bonded to the endwalls using a thermal adhesive. Rated at 50W each, these heaters were designed to meet the heating requirements for the entire Reynolds number range to be tested. A simple program was written to provide automatic on/off control of these heaters to maintain desired endwall temperature and to record total heat rate based on electrical energy requirements. As a

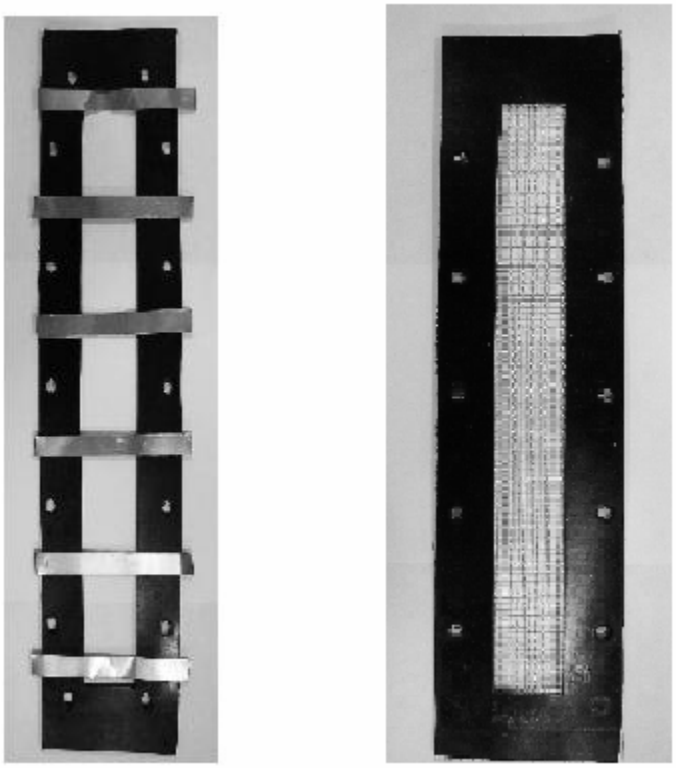

Figure 69 Turbulence generators, coarse (left) and fine (right)

backup means of measuring total heat flux, an in-line wattmeter was used to provide an additional source for measuring electrical power supplied to the strip heaters. Wall temperature of each section was indicated by thermocouples mounted in grooves machined into the endwalls. For this application, the thick aluminum plate served to provide adequate thermal inertia to promote an even temperature distribution spatially and temporally throughout the endwall.

Other instrumentation measured air temperature, pressure and velocity. Air temperature was recorded using a single thermocouple at the entry duct inlet and four thermocouples at the end of the insulated mixing chamber. Air pressure was recorded at the test section inlet and exit. Airflow was measured using a turbine flowmeter. Flow velocity was controlled using relief valves mounted between the blower and the airflow meter and by placing filters on the inlet. Further details of the experimental configuration can be found in Ref. 20, and photographs of some of the equipment are shown in Appendix D.

2. Experimental Method

Test procedures were consistently and methodically executed to ensure reliable data quality. At the start of each test period, ambient atmospheric pressure was recorded using NOAA data from a nearby airport located at the same altitude as the laboratory. Next, the strip heaters were energized and set to maintain desired wall temperature. Before turning on the blower, heater energy was measured to calculate heat losses to the environment. Finally the blower was activated and various bleed valve and entry filter combinations were used to achieve desired flow rates. Steady state conditions were achieved when heat exchanger outlet temperatures remained constant. Streaming data were recorded in a spreadsheet format and included individual wall temperatures, cooling air inlet temp, outlet air temperature and pressure, turbine flowmeter output and pressure drop across the array. Data were recorded for 20 minute periods to ensure sufficient data sampling.

a. Array Characteristic Length

For consistency, volume-based hydraulic diameter was used for the experimental testing as it had been for the numerical analysis.

b. Test Matrix

Several configurations of pin-fin arrays were chosen for testing as shown in Table 15. Both experimental and numerical runs were completed with each configuration. These configurations were chosen to provide a sample of data points applicable to each of the major numerical analysis categories previously completed. Additionally, pin dimensions were selected to ensure compatibility with the common test section and ducting to reduce setup time and cost. Each configuration was tested with a 6 and 12 degree C temperature difference between wall temperature and cooling air temperature and had an axial pitch of 50 mm. Finally, each configuration was also tested with and without turbulence generators installed immediately upstream of the test section to qualitatively characterize the effects of turbulence intensity on heat exchanger performance.

Table 15 Experimental and numerical test configurations, Re_{Dh} = 5,000 – 45,000

Circular Pin Configurations			
Diameter	*S/D*	*X/D*	*H/D*
33.0 mm	1.5	1.5	1.0
16.5 mm	3.0	3.0	2.0
10.0 mm	5.0	5.0	3.33
Airfoil Pin Configuration			
S/D	*H/D*	*LR*	*AR*
3.67	2.44	0.9	3.30

3. Data Reduction

Once the raw data were acquired, a MATLAB program was used to calculate desired output quantities. The following steps were followed to calculate the test array Nusselt number and friction factor.

a. Nusselt Number

Total heat transfer rate and mass flow rate were recorded directly from the instrumentation and data acquisition system.

Outlet bulk temperature was calculated from a simple energy balance as:

$$T_{out} = T_{in} + \frac{Q}{\dot{m}\ C_p} \qquad (26)$$

As a check, this outlet temperature was compared with the outlet bulk temperature obtained by averaging the results of the four thermocouples located in the mixing chamber. In most cases, the temperatures were identical. If the temperatures differed by more than 0.1 K, then the run was repeated. With output temperature resolved, the log mean temperature difference was calculated over the test array as follows:

$$\Delta T_{lm} = \frac{\left(T_{wall} - Tbulk_{in}\right) - \left(T_{wall} - Tbulk_{out}\right)}{\ln\left(\frac{T_{wall} - Tbulk_{in}}{T_{wall} - Tbulk_{out}}\right)}$$

The heat transfer coefficient was calculated using the following equation:

$$\overline{h}_{array} = \frac{Q}{A_{wetted}\ \Delta T_{lm}}$$

Finally, the Nusselt number for the array was determined using:

$$Nu_{D_h} = \frac{\overline{h}_{array} D_h}{k}$$

Additionally, due to the independent nature of the modular heated sections, row-by-row temperature profile was obtained through a simple energy balance. From this, row-by-row Nusselt number development was derived.

b. Friction Factor

The friction factor in the array was calculated using the following definition: $$f' = \frac{\Delta P_{array} D_h}{\frac{1}{2}\rho \overline{U}^2 L}$$

where L was the overall streamwise length of the array.

4. Uncertainty Analysis

Experimental uncertainty was estimated using the method of Kline and McClintock (Ref. 21) for Nusselt number, friction factor and Reynolds number. Due to the wide range of Reynolds numbers tested, the relative uncertainty values also cover a wide range. Table 16 shows these estimated values for each parameter. For Reynolds number and friction factor, the greatest uncertainty occurred at the lowest Reynolds number and the smallest uncertainty occurred at the high Reynolds numbers. Of particular note is the high uncertainty values for the airfoil-shaped pins. This was primarily due to the difficulty associated with measuring the extremely low pressure drop across the array at the lowest Reynolds number tested even with an inclined manometer. Details on the uncertainty analysis are provided in Appendix E.

Table 16 Experimental Uncertainty

Parameter	Relative Uncertainty (%)
Re_{Dh} (5,000 – 45,000)	4.9 – 1.9
Nu_{Dh} (ΔT = 6K)	8.3
Nu_{Dh} (ΔT = 12K)	4.2
Friction factor (33 mm pins)	3.3 - 0.62
Friction factor(16.5 mm pins)	3.4 – 0.64
Friction factor(10 mm pins)	20.0 – 0.68
Friction factor (airfoil pins)	25 - 0.78

C. EXPERIMENTAL RESULTS

Upon completion of the test runs, the experimental results were compared with data obtained from the numerical model. As discussed previously, the numerical models were used to develop Nusselt number and friction factor correlations as a function of Reynolds number. Additionally, heat transfer coefficient was plotted against fluid friction power as a key performance metric. In this section, results from each experimental configuration are matched with the corresponding numerical results to provide a means for evaluating the model validity.

1. Nusselt Number

Figure 70 shows Nusselt number results for each of the pin configurations. Note that in most cases there is excellent agreement between the numerical and experimental results for the mid to low range Reynolds numbers. However, for Reynolds numbers above 20,000, the numerical model tends to result in higher Nusselt number values when compared to the experimental data. The largest difference noted was 18%. There are at least two possible reasons for this difference.

The first cause may be due to contact resistance between the endwall and pin-fins in the experimental rig. In the numerical model, both the endwall and pin-fin surfaces were maintained at the same temperature for all runs. However, in the experimental rig, the pin-fins are heated indirectly by the strip heaters via conduction through the endwalls. At the lower Reynolds numbers, the pin-fins are able to maintain desired temperature as the heat flux requirement is relatively small. However, at the higher Reynolds numbers, the small yet finite contact resistance results in a slightly lower pin temperature when compared to the endwall. This difference in temperature can result in lower Nusselt numbers than predicted by the numerical model.

The second reason may be due to inaccuracies in the numerical solution at higher Reynolds numbers. Although turbulence models are generally more accurate at high Reynolds number, they often have difficulties characterizing regions of flow recirculation such as those that would form behind the pin-fins in the test array. Additionally, there may be problems in accurately depicting points of flow separation from the pins. It is reasonable to consider that inaccuracies arising from poor characterization of these regions would be magnified as flow velocity increased.

However, despite the differences noted, the agreement between the numerical model and the experimental results were considered satisfactory and within the bounds of experimental uncertainty.

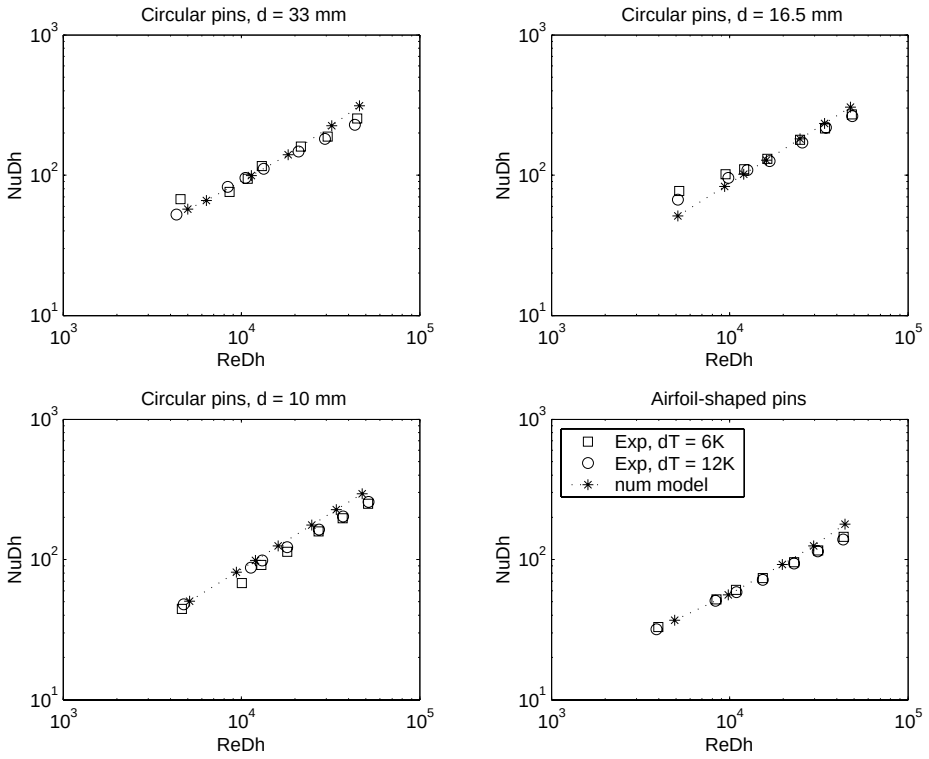

Figure 70 Model validation, Nusselt number

Due to the ability to heat each row independently, it is possible to resolve row-by-row local Nusselt number. Figure 71 and Figure 72 show local Nusselt number plotted for each row of pins. Both figures show the 33 mm pin configuration. In both cases, the Nusselt number quickly climbs to maximum value by the third row. However, Nusselt number decreases rapidly in Figure 71 similar to the heat transfer coefficient trends seen in the numerical case represented by Figure 23. However, in Figure 72, the Nusselt number remains high after the third row. This may be due to the increased turbulent energy present in the higher speed flow. The numerical model also showed this type of level Nusselt development curve at high flow velocities. These similarities increased confidence in the numerical model's ability to characterize the heat transfer characteristics of the pin-fin heat exchanger.

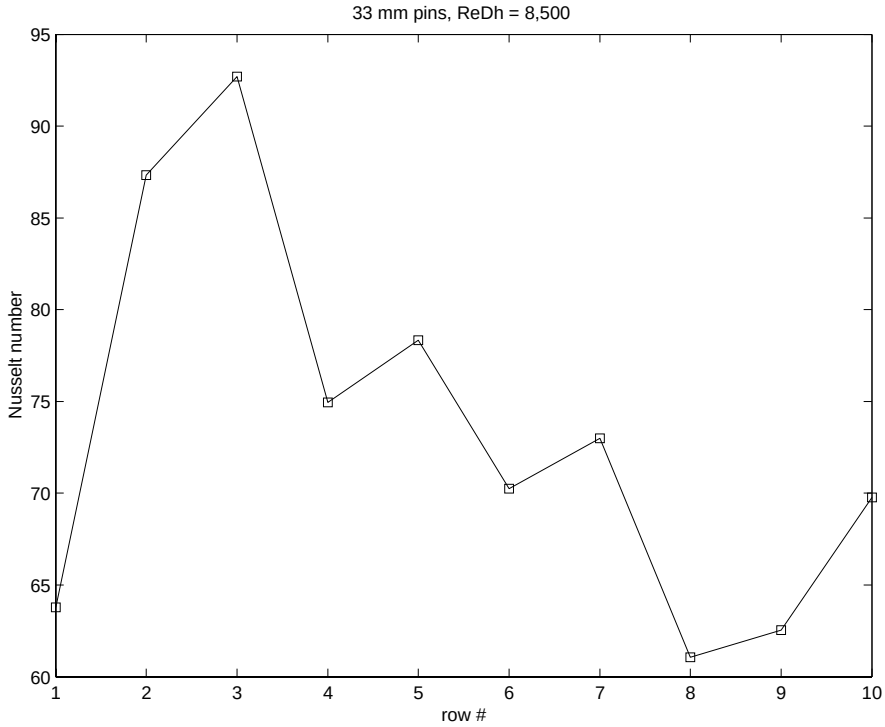

Figure 71 Nusselt number development, Re_{Dh} = 8,500

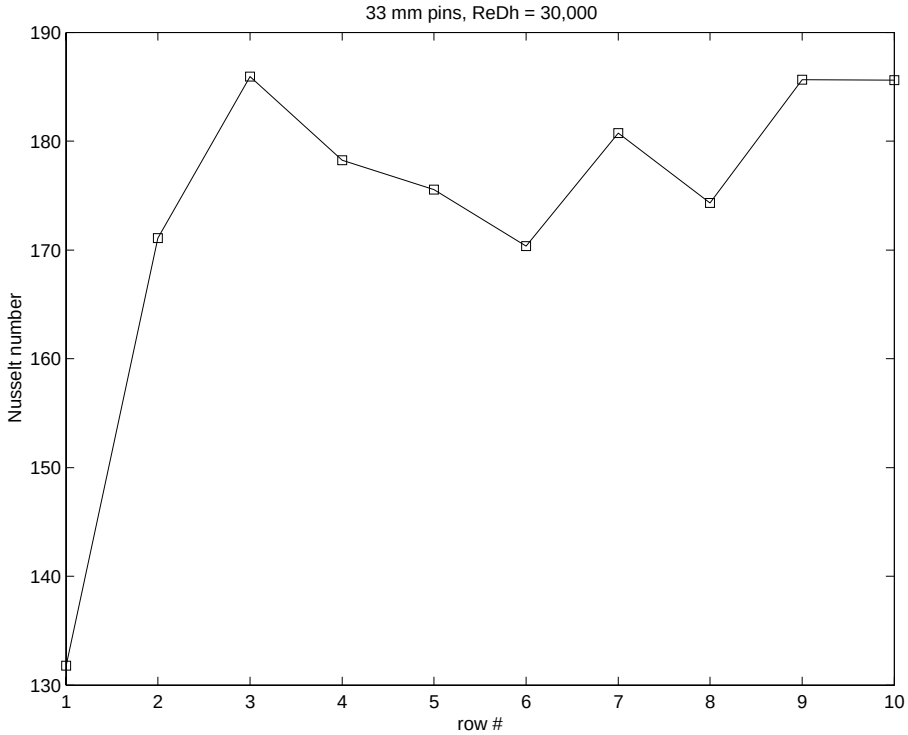

Figure 72 Nusselt number development, Re_{Dh} = 30,000

2. Friction Factor

Figure 73 shows the comparison between friction factor for the experimental and numerical runs for each configuration. For the 33 mm diameter circular pin-fin array, the numerical model overestimates the friction factor by up to 50%. In the case of the smaller circular pins and airfoil-shaped pins, the agreement is much better. However, in all cases except for the 10 mm pins, the numerical solution and experimental results appear to diverge as Reynolds number increases. This difference at high Reynolds number is consistent with the trends observed above with Nusselt number. Unlike the heat transfer solution however, only the aforementioned concern with the numerical modeling of the recirculation zone is relevant.

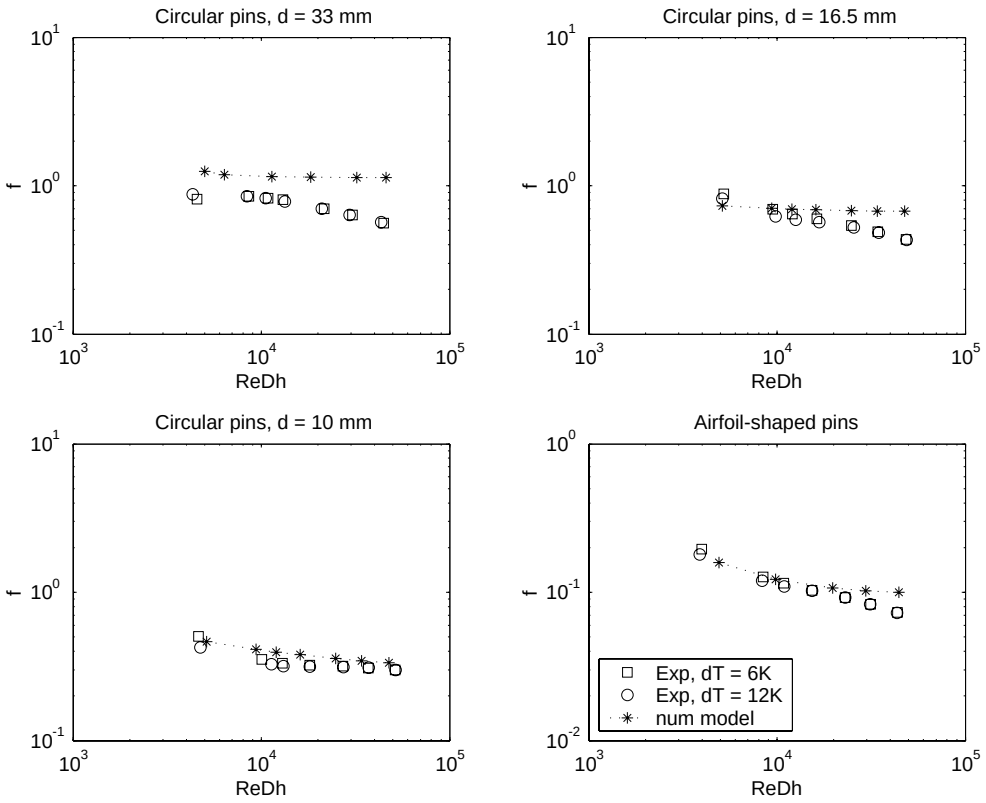

Figure 73 Model validation, friction factor

In fact, possible difficulties in numerically characterizing the recirculation zones or flow separation points are reasonable considering the trends observed with friction factor. The size of the recirculation zones relative to the open volume would be greater

for the larger pins than for the small circular or airfoil-shaped pins. Additionally, these zones would have a greater impact at higher Reynolds number for all configurations. These same trends were observed in the earlier comparison with the experimental results of Arora (Ref. 11).

Further evidence of premature flow separation can be seen in the numerical solution. In the previous section, a numerically derived plot of normalized heat transfer coefficient development on both a circular and airfoil-shaped pin-fin were shown as Figure 66. Here, the heat transfer coefficient appeared to drop off at 80 - 85 degrees from the leading edge of the circular pin which is indicative of flow separation. This separation point is significantly earlier than the typically accepted value for turbulent flow of approximately 110 - 120 degrees as found in elementary fluid mechanics textbooks such as White (Ref. 22). As a result of the earlier separation, the low pressure recirculation zone or wake is likely larger for the numerical solution than it is for the experimental case. This would cause higher pressure drop and subsequently higher friction factors for the circular pins.

For the airfoil-shaped pins, there is very little separation and the recirculation zone is not as significant as it was for the circular pin case. As this zone is relatively small, its contribution to the total pressure drop in the array is also small. As a result, errors associated with the numerical solution are also not very significant. As a result, there is significantly better corroboration with the experimental solution.

Despite the problems with accurately predicting the pressure drop for the large diameter circular pin array, the numerical model was still considered useful in showing trends between different configurations. In Figure 74, two plots of friction factors are shown for all configurations. One chart includes only numerical results and the other only shows experimental results. Although the numerical model overestimates the large pin friction factor, it can be seen that the experimental trends are properly predicted.

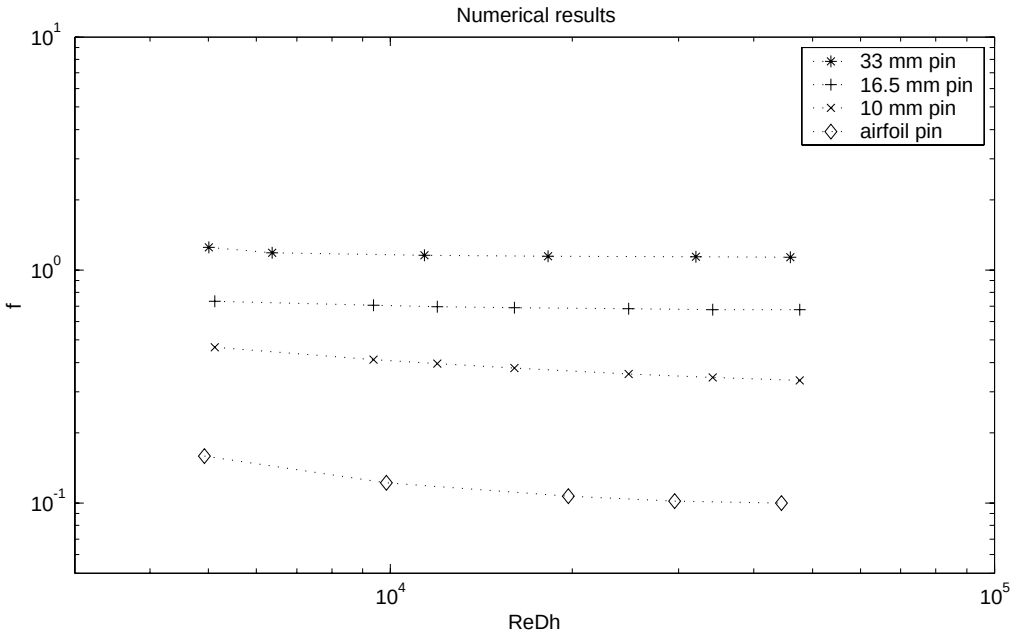

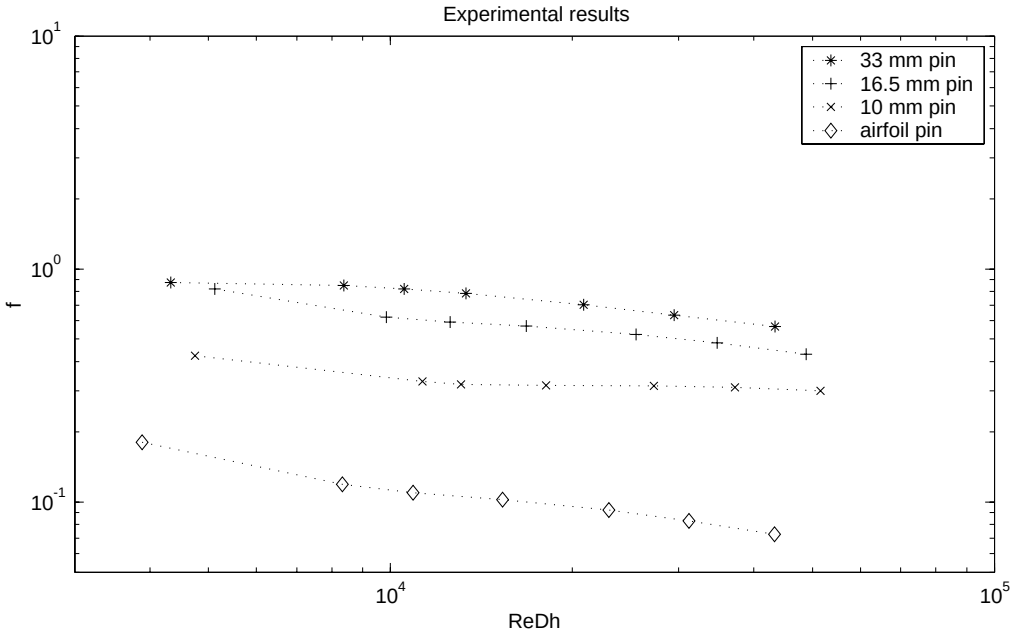

Figure 74 Friction factor trends between configurations

3. Performance Comparisons

Plots of heat transfer coefficient versus specific fluid friction power provide a very useful metric in determining the performance of heat exchanger. These charts illustrate the "cost" of a given configuration to transfer heat. Figure 75 shows these performance charts for each configuration using data from the numerical and experimental runs. Note that despite the previously identified differences in friction factor seen with the circular pins, the *h* vs. *E* curves show good agreement between numerical and experimental results. This is likely due to the fact that the model tends to overestimate both Nusselt number and pressure drop at the higher Reynolds numbers. These errors are effectively canceled since the higher heat transfer coefficient appears to "cost" more in terms of fluid friction power. This causes the numerical performance curve to shift slightly up and to the right compared to the experimental data for the same Reynolds number range. These slight differences did not impair the model's utility in comparing the relative performance between configurations.

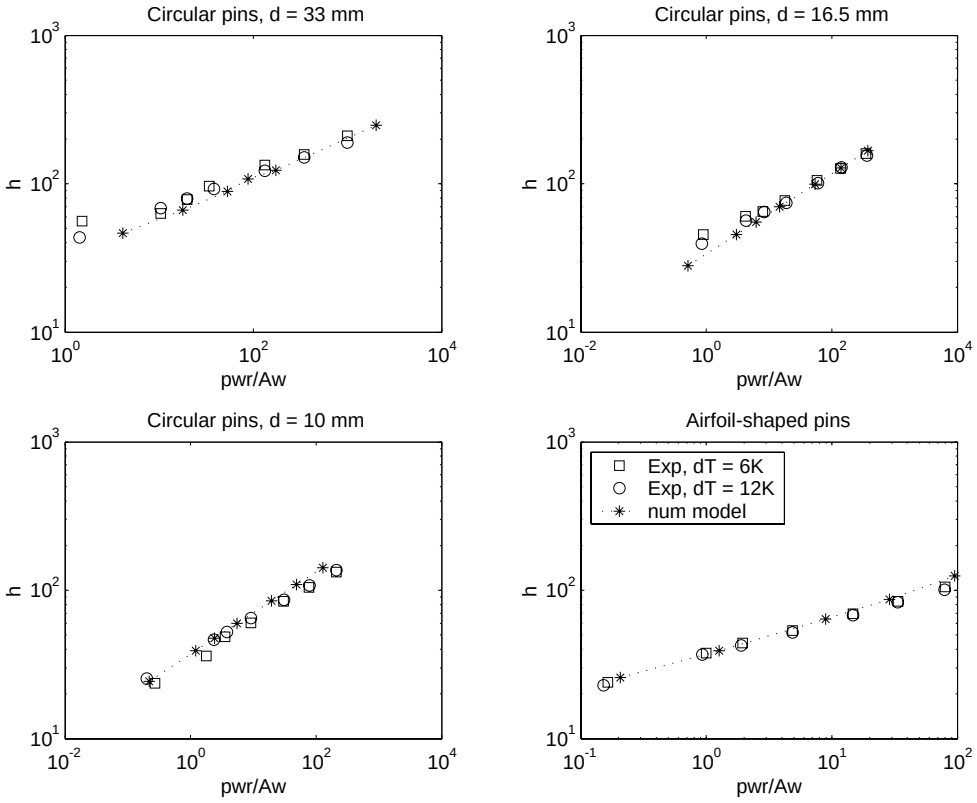

Figure 75 Model validation, overall performance

4. Effect of Turbulence Generators

A qualitative evaluation of the effect of turbulence generators was conducted and the results are shown in this section. Figure 76 shows the effects of the turbulence generators on each pin-fin type. For the circular pins, there was no noticeable difference in Nusselt number when the turbulence generators were installed. However, the turbulence generators increased Nusselt number in the airfoil-shaped pin-fin array by 35 – 50%. This difference is likely due to the difference in flow characteristics between these configurations. With the circular pins, there is already a high level of turbulence within the array once the flow gets past the first or second row. Therefore introducing additional turbulence upstream of the array has little effect on the already highly turbulent flow situation. However, in the case of the airfoil-shaped pins, the flow naturally has a lower turbulence level as the path is not as tortuous as it is in the circular

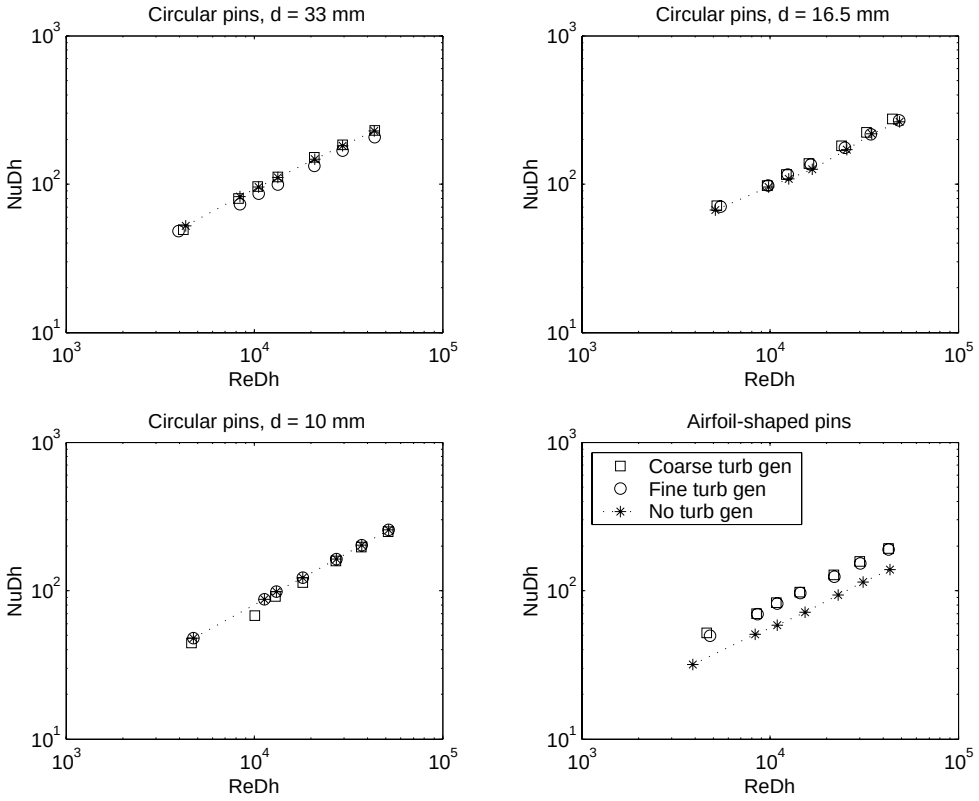

Figure 76 Effect of turbulence generators on Nusselt number

pin case. As a result, introducing upstream disturbances significantly increases turbulence intensity within the array yielding an enhanced heat transfer rate. It is interesting to note that there was little difference in Nusselt number between the coarse and fine turbulence generators for the airfoil-shaped pins. This suggests a turbulence threshold beyond which there is little benefit in creating larger flow disturbances.

While the introduction of the turbulence generators affected the experimental results, no similarities were observed in the numerical model. Increasing turbulence intensity in the numerical model had no significant effect on the heat transfer rate or pressure drop. This suggests one of two possibilities. First, like the circular pin experimental case, the background turbulence in the numerical airfoil-shaped pin model may have been sufficiently high such that increased turbulence intensity had little or no effect. Second, the level of turbulent intensity achieved numerically may have been much lower and not representative of the level attained by the turbulence generators in the experiment. In either case, the previous section detailing the numerical analysis of the airfoil-shaped pins covers a nominal situation in which the flow, although turbulent, is relatively undisturbed as it enters the array. In a representative application like turbine blade cooling, the flow would likely be much more disturbed. Based on the experimental impact of the turbulence generators, actual heat transfer rates for installed airfoil-shaped pin-fin arrays may be even greater than predicted by the results of this numerical work.

Unfortunately, due to the configuration of this experiment, no meaningful data could be obtained to evaluate the effects of turbulence generators on friction factor. This was because the turbulence generators were located between the entry pressure tap and the test array. Thus recorded pressure drop would have included the turbulence generators rather than just the test array.

D. CONCLUSIONS

The objectives of this phase of testing were met by comparing heat transfer and pressure drop results obtained by the numerical model with data recorded from various pin configurations mounted in an experimental rig. Several findings were:

1. The numerical simulation modeled the heat transfer characteristics of the circular and airfoil pin-fin arrays over a Reynolds number range of 5,000 to 45,000 to within 18%.

2. The numerical model overestimated friction factor by up to 50% for the 33 mm circular pin array but was much closer for the 16.5 mm and 10 mm circular pin and airfoil-shaped pin arrays. These differences may have been due to shortcomings in the simulation's ability to properly model flow separation and areas of recirculation. In most cases, the numerically obtained friction factor tended to diverge from the experimental results at higher Reynolds number.

3. Despite shortcomings in characterizing absolute friction factor, the numerical model was useful for discriminating between configurations since relative friction factor values were consistent.

4. Overall heat exchange performance based on heat transfer coefficient and fluid friction power was characterized closely by the numerical model for all configurations.

5. The introduction of turbulence generators in the experimental rig increased Nusselt number by 35-50% for the airfoil-shaped pin-fin array. No significant changes were noted for the circular pin arrays. This was likely due to the fact that the circular pin arrays were already operating at high turbulence intensity due to the tortuous nature of the flow around the pin-fins.

6. The numerical model was not affected by the introduction of additional turbulence. This suggests that the airfoil-shaped pin array may perform even better than predicted in a real-world environment.

IV. CONCLUSIONS

Due to the modular nature of this study, specific conclusions have already been discussed at the end of each major section/chapter. However, this section shall be used to review the significant findings of this work as an entity and capture the main concepts in summary form.

The major contributions of this study were to advance knowledge in the growing field of microscale heat exchanger technology and to develop innovative ways of improving heat transfer performance in the staggered cross pin-fin heat exchanger. The major objective of this work was met by successfully simulating the pin-fin heat exchanger with a 3-D numerical model and using it to investigate a wide range of configurations, Reynolds numbers, array sizes, pin height ratios and pin shapes. The model was validated with historical and current experimental data. It consistently predicted Nusselt number for all configurations tested within 18% but was found to have some shortcomings in predicting friction factor. Despite these shortcomings, it provided a reliable measure of overall heat exchanger performance.

The model demonstrated the advantages of reducing axial pitch to achieve superior heat exchanger performance within the limits of particulate contamination resistance. Using a porous medium type open flow volume based hydraulic diameter as the characteristic length, the model demonstrated that Nusselt number and friction factor were independent of actual heat exchanger size for all configurations, pin height ratios and pin shapes. This important finding permits microscale heat exchanger optimization to be performed on a more manageable macroscale basis since the dimensionless correlations can be directly transferred to the small scale.

Additionally, the model demonstrated that airfoil-shaped pin-fin arrays outperform similar sized circular pin-fin arrays. In the optimum airfoil-shaped pin array case modeled, the circular pin-fin array required three times the specific energy loss to produce the same heat transfer rate. In addition, experimental data have indicated that increased turbulence levels can improve heat transfer rates in airfoil pin arrays by 35-50% while having no benefit for the circular pin array. Thus the performance of the

airfoil-shaped pin array, already superior to the circular pin array, would be further enhanced in an installed configuration where turbulence was likely to be greater than in the laboratory or numerical environment.

Further, optimum pin configuration depends greatly on the desired application. In situations requiring large heat flux through a small face area, such as in electronic component cooling applications, increases in pin height ratio have a significant effect on performance. This is due to the magnification of wetted by pin-fin arrays thereby increasing effective heat transfer coefficient. Details on this area magnification and a sample application are presented in Appendix F. The trends observed in this study would be useful to provide the designer with initial guidance in producing the optimum heat exchanger design for a given application.

Finally, it is important to understand some limits to the applicability of the correlations presented in this work. First, since the effects of buoyancy and body forces were not investigated, results in a rotating reference frame may vary. As such, direct use of these correlations would be more suited to stator blades or fixed electronic component cooling applications. However, even for rotor blades, these correlations would provide the design engineer with a means of comparing the relative benefits of various pin-fin configurations. Secondly, even if concerns over particulate contamination could be eliminated, there is a limit in size reduction based on the mean free path of the gas. Beyond this limit, the gas would no longer obey the continuum hypothesis on which the Navier-Stokes equations are based and could violate the no-slip condition along rigid boundaries. Appendix G provides further details on this limitation.

APPENDIX A. MODEL DETAILS

GENERAL METHOD

All models were constructed by first creating a three-dimensional "block" to represent the cooling air in the test array. The pins were created by removing appropriately shaped volumes using Boolean subtraction from the initial block. This resulted in holes in the model that represented the pin-fins in the test array. Finally two additional 3-D blocks representing the adiabatic entry and exit duct were created and "glued" to the test array.

ROUND PIN MODELS

The round pins were constructed in ANSYS by simply creating circular volumes with the desired radius.

AIRFOIL-SHAPED PINS

The airfoil-shaped pins were created from the intersection of two circular volumes of radius, R, as shown in Figure 77. The horizontal component of radius, Rx, was defined as a fraction of axial pitch, X, by specifying the desired length ratio (2*Rx/X) from the test matrix. Then, slenderness ratio (Ry/Rx) was used to define Ry and achieve the desired aspect ratio (A/D). Finally, R was calculated and the circle centers were spaced 2Ry apart. The volume defined by the intersection of these circles was subtracted from the cooling air block and represented the airfoil-shaped pins.

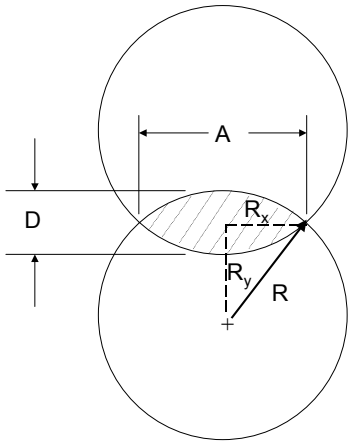

Figure 77 Airfoil construction details

ISOTHERMAL PIN BOUNDARY CONDITION JUSTIFICATION

As stated earlier, the pins were treated as isothermal entities through boundary condition selection. Calculations to justify this decision are present in this section. The configuration used for these calculations is: *S/D* = *X/D* = 1.5, *H/D* = 1, *X* = 50 mm. This was one of the experimental configurations.

The governing equations for this calculation are taken from Incropera and DeWitt (Ref. 18). Using an adiabatic tip assumption, they are:

$$\frac{\theta}{\theta_b} = \frac{T - T_\infty}{T_b - T_\infty} = \frac{\cosh m(L - x)}{\cosh(mL)}$$

where $m = \sqrt{\frac{hP}{kA_c}}$, T_∞ is the cooling air temperature, T_b is the pin base temperature, and *T* is the temperature along the pin at a distance *x* from the base. Also, *L* is half the pin height (0.033 m) in order to use the adiabatic assumption.

Perimeter, P = 0.1046 m, $k_{aluminum}$ = 177 (W/mK),

and cross sectional area, A_c = 8.7092e-4

For high Reynolds number (where this analysis is particularly important) *h* can be taken as approximately 150 W/m^{2}K, based on experimental results.

Substituting, m = 8.32

Thus, $T = T_\infty + (T_b - T_\infty)\frac{\cosh 8.32(0.0165 - x)}{\cosh(8.32 * 0.0165)}$

Assuming worst case conditions, $T_\infty = 300K$ and $T_b = 312K$

The midpin temperature is 311.89K. This is considered close enough to 312K to assume that the pin is isothermal.

APPENDIX B. SAMPLE ANSYS MACRO

In order to efficiently and systematically manage the large number of numerical models evaluated in this study macros were written for each heat exchanger type. Each macro performed the following basic tasks:

1. Provided easy input entry such as Reynolds number, pin spacing and height ratio, axial pitch, inlet air and wall temperature, reference pressure and mesh density.

2. Constructed and meshed the model.

3. Set ANSYS solution parameters to include solver type and iteration number.

4. Ran the solution.

In reviewing the following sample macro, the reader will notice that the solution is started three times. This is to accommodate the sensitive nature of the Collocated Galerkin (COLG) solver. For the initial solution, density is held constant and the MSU approach is used to discretize the momentum equations. No thermal analysis is conducted. This allows a rough flow solution to develop. For the next series of iterations, density is allowed to vary according to the equation of state and the energy equation is solved. For the third phase, COLG is used to discretize only the momentum equation. By this point, the solution is fairly robust and the final phase can be initiated. In the final phase, the COLG approach is used for all parameters. In some cases, if the preliminary steps are not completed, the solution will diverge. The sample macro is presented next:

```
/TITLE,Re=5000,X/D=1.5,S/D=1.5,Tw =306,h/v/p =7.8/15/2,SKE,COLG
adv,10atm,1.5inf
! creates an endless 1.5 pin fin array with 10 rows
! unheated entry and exit regions
! L.J. Hamilton 7 NOV 02
!****************************************
!Enter Reference pressure in Pa
Pref = 101350

!Enter your Reynold's Number (VanFossen definition)
Re=5000

!Enter your X/D (cylinder spacing in the flow direction)
xd=1.5

!Enter your S/D (spanwise (perp to flow)
sd=1.5

!Enter your H/D (Pin height/diameter ratio)
hd=1.0

!Enter xy (h)/and z (v) grid scaling
h = 7.8
v = 15
!Enter pin factor
p = 2


!Enter axial pitch (Absolute distance between pin centers)
x=.0127

!Enter your Twall
Twall=306
Tfilm = (Twall+300)/2


! calculates pin diameter
d=x/xd

!Calculate kinematic viscosity using Sutherland Law
rho = Pref/(287*Tfilm)
rho300 = Pref/(287*300)
!mu = 1.86e-5
mu = 383.4/(Tfilm+110.4)*1.71e-005*(Tfilm/273)**(3/2)
nu = mu/rho
!calculated for a unit cell (s*2x)
```

```
Varray = 2*sd*xd*hd*d**3
Vpin = 3.14159*hd*d**3/4
Vopen = Varray - 2*Vpin
Awpin = 3.14159*hd*d**2
Afeet = 3.14159*d**2/4
Awall = 2*sd*xd*d**2 - 2*Afeet
Aw = 2*Awpin + 2*Awall
Abar = Vopen/(2*x)
Aduct = sd*hd*d**2
Dprime = 4*Vopen/Aw


!******************Inlet Velocity Calculation*********

Vin = Re*mu*Abar/(Dprime*rho300*Aduct)

!******************Determine length of pin section*****
!Pin center to pin center streamwise distance
ddx=d*xd
!Pin center to pin center spanwise distance
ssy=d*sd
!Pin Height
Ht = hd*d

!Calculate entry length for FD turb flow
EntryDh = 2*Ht
EntryRe = Vin*EntryDh/nu
entry = EntryDh*4.4*EntryRe**(1/6)
entryinit = entry

!Enter exit length (after the pins. Metz:7.62cm, to
!                  prevent feedback in the ANSYS
!                  soln: 12.5cm)[m]
exit = 0.125

!Total length of pin section with (xd/2)*d before the
!leading edge and (xd/2)*d following the trailing edge
!of the last row of pins.
xlength= (ddx*10)
!Total width of ANSYS model, insulated wall to sym plane.
ylength= (ssy*1.5)
!*********setup/overhead*******************************
! ****************THIS MODULES SETS FLOTRAN PARMS*********
!***********selects operating preference***************
/NOPR
```

```
/PMETH,OFF,0
KEYW,PR_SET,1
KEYW,PR_STRUC,0
KEYW,PR_THERM,1
KEYW,PR_FLUID,0
KEYW,PR_ELMAG,0
KEYW,MAGNOD,0
KEYW,MAGEDG,0
KEYW,MAGHFE,0
KEYW,MAGELC,0
KEYW,PR_MULTI,1
KEYW,PR_CFD,1
/GO
!*
/COM,
/COM,Preferences for GUI filtering have been set to display:
/COM,  Thermal
/COM,  FLOTRAN CFD
!*
/UNITS,SI
/PREP7
!*
!selects element type
ET,1,FLUID142
!*
!*****************INITIAL SOLN OPTIONS*************
FLDATA1,SOLU,TRAN,0
FLDATA1,SOLU,FLOW,1
FLDATA1,SOLU,TEMP,0
FLDATA1,SOLU,TURB,1
FLDATA1,SOLU,COMP,0
FLDATA1,SOLU,VOF,0
FLDATA1,SOLU,SFTS,0
FLDATA1,SOLU,IVSH,0
FLDATA1,SOLU,SWRL,0
FLDATA1,SOLU,SPEC,0
FLDATA1,SOLU,ALE,0
!******************INITIAL EXECUTION CONTROL********
/COM,,Steady State Analysis,0
FLDATA2,ITER,EXEC,30,
FLDATA2,ITER,OVER,0,
FLDATA2,ITER,APPE,0,
FLDATA3,TERM,VX,0.01,
FLDATA3,TERM,VY,0.01,
FLDATA3,TERM,VZ,0.01,
```

```
FLDATA3,TERM,PRES,1e-008,
FLDATA3,TERM,TEMP,1e-008,
FLDATA3,TERM,ENKE,0.01,
FLDATA3,TERM,ENDS,0.01,
FLDATA5,OUTP,SUMF,10,
FLDATA5,OUTP,YPLU,T
!*****************ADDED TO MAKE DENSITY AN OUTPUT
FLDATA5,OUTP,DENS,T,
!*
/PREP7
FINISH
/PREP7
!************INITIAL FLUID PROPERTIES (CONSTANT DENSITY)*************
FLDATA12,PROP,DENS,4
FLDATA13,VARY,DENS,0
FLDATA12,PROP,VISC,4
FLDATA13,VARY,VISC,1
FLDATA12,PROP,COND,4
FLDATA13,VARY,COND,1
FLDATA12,PROP,SPHT,4
FLDATA13,VARY,SPHT,1
!*
FLDATA7,PROT,DENS,AIR-SI
FLDATA8,NOMI,DENS,-1
FLDATA9,COF1,DENS,0
FLDATA10,COF2,DENS,0
FLDATA11,COF3,DENS,0
FLDATA7,PROT,VISC,AIR-SI
FLDATA8,NOMI,VISC,-1
FLDATA9,COF1,VISC,0
FLDATA10,COF2,VISC,0
FLDATA11,COF3,VISC,0
FLDATA12,PROP,IVIS
FLDATA7,PROT,COND,AIR-SI
FLDATA8,NOMI,COND,-1
FLDATA9,COF1,COND,0
FLDATA10,COF2,COND,0
FLDATA11,COF3,COND,0
FLDATA7,PROT,SPHT,AIR-SI
FLDATA8,NOMI,SPHT,-1
FLDATA9,COF1,SPHT,0
FLDATA10,COF2,SPHT,0
FLDATA11,COF3,SPHT,0
!***Select ref temp = 300K*************
FLDATA14,TEMP,NOMI,300
```

```
FLDATA14,TEMP,TTOT,300
FLDATA14,TEMP,BULK,300
FLDATA15,PRES,REFE,Pref
!*
!***PLACEHOLDER FOR TURBULENCE MODEL INPUTS**************
!SKE=1(Default),ZETM=2,RNG=3,NKE=4,GIR=5,SZL=6
!FLDATA24,TURB,MODL,1
!*************TEMP CFD SOLVER IS PGMR********************
FLDATA18,METH,TEMP,4
FLDATA22,MAXI,TEMP,1000,
FLDATA20,SRCH,TEMP,12,
FLDATA20A,PGMR,FILL,6,
FLDATA20A,PGMR,MODP,0,
FLDATA21,CONV,TEMP,1e-12,
FLDATA23,DELT,TEMP,1e-010,
!*
!***********ADVECTION PARMS***************
FLDATA,ADVM,MOME,MSU
FLDATA,ADVM,TURB,MSU
FLDATA,ADVM,PRES,MSU
FLDATA,ADVM,TEMP,MSU
!*
!************************BLOCK & PINS*********************
/prep7
!Creates initial block with extra 0.01 length

!Start in middle of first row
xloc=entry + ddx/2
start=entry
*do,i,1,5
Block,entry,entry+ddx,0,ylength,0,Ht/2
cyl4,xloc,ssy/2,d/2,,,,Ht/2
cyl4,xloc,(ssy*1.5),d/2,,,,Ht/2
Block,entry+ddx,entry+2*ddx,0,ylength,0,Ht/2
cyl4,(xloc+ddx),0,d/2,,,,Ht/2
cyl4,(xloc+ddx),ssy,d/2,,,,Ht/2
xloc=xloc + (ddx*2)
entry=entry + (ddx*2)

*enddo

!***************SUBTRACT PINS********************
FLST,2,10,6,ORDE,10
FITEM,2,1
FITEM,2,4
```

```
FITEM,2,7
FITEM,2,10
FITEM,2,13
FITEM,2,16
FITEM,2,19
FITEM,2,22
FITEM,2,25
FITEM,2,28
FLST,3,20,6,ORDE,20
FITEM,3,2
FITEM,3,-3
FITEM,3,5
FITEM,3,-6
FITEM,3,8
FITEM,3,-9
FITEM,3,11
FITEM,3,-12
FITEM,3,14
FITEM,3,-15
FITEM,3,17
FITEM,3,-18
FITEM,3,20
FITEM,3,-21
FITEM,3,23
FITEM,3,-24
FITEM,3,26
FITEM,3,-27
FITEM,3,29
FITEM,3,-30
VSBV,P51X,P51X
!***********ADD ENTRY BLOCK******************
Block,0,start,0,ylength,0,Ht/2
!***********ADD EXIT BLOCK*******************
Block,start+xlength,start +xlength+exit,0,ylength,0,Ht/2
!need to glue entry and exit!
FLST,2,12,6,ORDE,4
FITEM,2,1
FITEM,2,-2
FITEM,2,31
FITEM,2,-40
VGLUE,P51X
!***Model is now built
!
!******************change the view to isometric********
```

```
/VIEW, 1 ,1,1,1
/ANG, 1
/REP,FAST
/AUTO, 1
/REP
VPLOT
/color,pbak,off
/REPLOT

!***********PINS*****************************
!1/n 1/n 1/n 1/n 1/n 1/n 1/n 1/n 1/n 1/n 1/n 1/n

!***********Cylinders (1/n)
lsel,s,line,,16

*do,i,0,1
*do,k,0,4
!Cylinders exit/upper side
lsel,a,line,,16 + 1*i + 64*k
!Cylinders inlet/lower side
lsel,a,line,,56 + 5*i + 64*k
*enddo
*enddo


*do,i,0,1
*do,j,0,1
*do,k,0,4
!Cylinders exit/upper side
lsel,a,line,,48 + 1*i + 10*j + 64*k
!Cylinders inlet/lower wall side
lsel,a,line,,14 + 5*i + 10*j + 64*k
*enddo
*enddo
*enddo

LESIZE,all,,,3*h/xd,1/p,,,,1

!nnnnnnnnnnnnnnnnnnnnnnnnnnnnnnnnnnnnnnnnnnnnnnnnn
!***********************Cylinders (n)
lsel,s,line,,15
*do,i,0,1
*do,k,0,4
!Cylinders inlet/upper side
lsel,a,line,,15 + 3*i + 64*k
```

```
!Cylinders exit/lower wall side
lsel,a,line,,55 + 7*i + 64*k
*enddo
*enddo

*do,i,0,1
*do,j,0,1
*do,k,0,4
!Cylinders inlet/upper side
lsel,a,line,,47 + 3*i + 10*j + 64*k
!Cylinders exit/lower wall side
lsel,a,line,,13 + 7*i + 10*j + 64*k
*enddo
*enddo
*enddo

LESIZE,all,,,3*h/xd,1/p,,,,1

!************Test Section Symmetry lines, short****************
lsel,s,line,,321
lsel,a,line,,322
lsel,a,line,,219
lsel,a,line,,220
lsel,a,line,,228
lsel,a,line,,229
lsel,a,line,,281
lsel,a,line,,282
lsel,a,line,,301
lsel,a,line,,302
lsel,a,line,,307
lsel,a,line,,308
lsel,a,line,,365
lsel,a,line,,366
lsel,a,line,,194
lsel,a,line,,199
lsel,a,line,,173
lsel,a,line,,174

*do,i,0,3
lsel,a,line,,153 + i
lsel,a,line,,327 + i
lsel,a,line,,335 + i
lsel,a,line,,343 + i
lsel,a,line,,351 + i
*enddo
```

```
LESIZE,all,,,h*xd/3,,,,,1

!*****************Test Section Symmetry Lines, Long***************
lsel,s,line,,130
lsel,a,line,,135
lsel,a,line,,164
lsel,a,line,,165
lsel,a,line,,217
lsel,a,line,,218
lsel,a,line,,237
lsel,a,line,,238
lsel,a,line,,243
lsel,a,line,,244
lsel,a,line,,283
lsel,a,line,,284
lsel,a,line,,292
lsel,a,line,,293
lsel,a,line,,361
lsel,a,line,,362
lsel,a,line,,363
lsel,a,line,,364
lsel,a,line,,179
lsel,a,line,,180

LESIZE,all,,,3*h,,,,,1

!****************Entry/Exit Symmetry Lines********************
lsel,s,line,,7
lsel,a,line,,36
lsel,a,line,,90
lsel,a,line,,91

LESIZE,all,,,15*h,2,,,,1

!********Entry/Exit Symmetry Lines for proper spacing**********
lsel,s,line,,71
lsel,a,line,,100
lsel,a,line,,26
lsel,a,line,,27

LESIZE,all,,,15*h,1/2,,,,1

!**************Inlet and Exit Lines*******************
```

```
!**************Inlet and Exit Lines*******************
lsel,s,line,,2
lsel,a,line,,37
lsel,a,line,,89
lsel,a,line,,92

LESIZE,all,,,3*h*sd/xd,,,,,1

!***************Glue Lines************************
lsel,s,line,,25
lsel,a,line,,28
lsel,a,line,,3
lsel,a,line,,6
lsel,a,line,,35
lsel,a,line,,38
lsel,a,line,,67
lsel,a,line,,70
lsel,a,line,,99
lsel,a,line,,102
lsel,a,line,,131
lsel,a,line,,134
lsel,a,line,,163
lsel,a,line,,166
lsel,a,line,,195
lsel,a,line,,198
lsel,a,line,,227
lsel,a,line,,230
lsel,a,line,,259
lsel,a,line,,262
lsel,a,line,,66
lsel,a,line,,101

LESIZE,all,,,3*h*sd/xd,,,,,1

!*****Vertical Lines Entry + those needed to ensure proper mesh***********
lsel,s,line,,52
lsel,a,line,,45
lsel,a,line,,109
lsel,a,line,,116

LESIZE,all,,,v,1/5,,,,1
!***********Vertical Lines, Test Section + Exit***
lsel,s,line,,110
lsel,a,line,,115
lsel,a,line,,51
```

```
lsel,a,line,,46

*do,i,0,1
*do,k,0,8
lsel,a,line,,10 + 1*i + 32*k
*enddo
*enddo

!*****************vertical lines (pins)*****
*do,i,0,1
*do,j,0,1
*do,k,0,4
lsel,a,line,,21 + 1*i + 10*j + 64*k
lsel,a,line,,53 + 1*i + 10*j + 64*k
*enddo
*enddo
*enddo

LESIZE,all,,,v,5,,,,1


lsel,all
asel,all

!****************Boundary Conditions*************
!
!*****************Pins vx=vy=vz=0, T=Twall*******
asel,s,area,,9

*do,k,0,4
*do,i,0,1
asel,a,area,,9 + i + 28*k
asel,a,area,,27 + i + 28*k
*enddo
asel,a,area,,14 +  28*k
asel,a,area,,23 +  28*k
*enddo



DA,all,vx,0,1
DA,all,vy,0,1
DA,all,vz,0,1
DA,all,TEMP,Twall,1
```

```
!*********************Entry/Exit endwalls vx=vy=vz=HFLU=0**********
asel,s,area,,1
asel,a,area,,12

DA,all,vx,0,1
DA,all,vy,0,1
DA,all,vz,0,1
SFA,ALL,,HFLUX,0

!*********************Endwall, vx=vy=vz=0, T=Twall*****
asel,s,area,,25
asel,a,area,,32
asel,a,area,,49
asel,a,area,,54
asel,a,area,,69
asel,a,area,,77
asel,a,area,,63
asel,a,area,,82
asel,a,area,,91
asel,a,area,,41
DA,all,vx,0,1
DA,all,vy,0,1
DA,all,vz,0,1
DA,all,TEMP,Twall,1

!*******symmetry (side) vy=0, HFLU=0
asel,s,area,,7
asel,a,area,,24
asel,a,area,,141
asel,a,area,,30
asel,a,area,,45
asel,a,area,,149
asel,a,area,,53
asel,a,area,,60
asel,a,area,,157
asel,a,area,,68
asel,a,area,,73
asel,a,area,,165
asel,a,area,,81
asel,a,area,,88
asel,a,area,,173
asel,a,area,,39
asel,a,area,,16
asel,a,area,,15
asel,a,area,,36
```

```
asel,a,area,,40
asel,a,area,,86
asel,a,area,,170
asel,a,area,,80
asel,a,area,,72
asel,a,area,,162
asel,a,area,,67
asel,a,area,,58
asel,a,area,,154
asel,a,area,,52
asel,a,area,,44
asel,a,area,,146
asel,a,area,,29
asel,a,area,,22
asel,a,area,,4

DA,all,vy,0,1
SFA,ALL,,HFLUX,0

!**********symmetry (middle) vz=0, HFLU=0******
asel,s,area,,2
asel,a,area,,26
asel,a,area,,35
asel,a,area,,50
asel,a,area,,57
asel,a,area,,64
asel,a,area,,71
asel,a,area,,78
asel,a,area,,85
asel,a,area,,92
asel,a,area,,43
asel,a,area,,13
DA,all,vz,0,1
SFA,ALL,,HFLUX,0

!************Inlet vx=Vin vy=vz=0, T=300K*********
asel,s,area,,8
DA,all,vx,Vin,1
DA,all,vy,0,1
DA,all,vz,0,1
DA,all,TEMP,300,0

!************Exit pdof=0***********
asel,s,area,,21
DA,all,pres,0,0
```

```
asel,all
!***************mesh*****************************
FLST,5,12,6,ORDE,2
FITEM,5,1
FITEM,5,-12
CM,_Y,VOLU
VSEL, , , ,P51X
CM,_Y1,VOLU
CHKMSH,'VOLU'
CMSEL,S,_Y
!*
VSWEEP,_Y1
!*
CMDELE,_Y
CMDELE,_Y1
CMDELE,_Y2
!*
/UI,MESH,OFF
!***********run FIRST (0-30 iter) solution***************
/SOLU
FINISH
/SOLU
SOLVE
!*********SECOND SOLN (30-60 iter) OPTIONS*************
FLDATA1,SOLU,TRAN,0
FLDATA1,SOLU,FLOW,1
FLDATA1,SOLU,TEMP,1
FLDATA1,SOLU,TURB,1
FLDATA1,SOLU,COMP,0
FLDATA1,SOLU,VOF,0
FLDATA1,SOLU,SFTS,0
FLDATA1,SOLU,IVSH,0
FLDATA1,SOLU,SWRL,0
FLDATA1,SOLU,SPEC,0
FLDATA1,SOLU,ALE,0
!*
!*********SECOND EXECUTION CONTROLS*************
/COM,,Steady State Analysis,0
FLDATA2,ITER,EXEC,30,
FLDATA2,ITER,OVER,0,
FLDATA2,ITER,APPE,0,
FLDATA3,TERM,VX,0.01,
FLDATA3,TERM,VY,0.01,
```

```
FLDATA3,TERM,VZ,0.01,
FLDATA3,TERM,PRES,1e-08,
FLDATA3,TERM,TEMP,1e-08,
FLDATA3,TERM,ENKE,0.01,
FLDATA3,TERM,ENDS,0.01,
FLDATA5,OUTP,SUMF,10,
FLDATA5,OUTP,YPLU,T
!******************ADDED TO MAKE DENSITY AN OUTPUT
FLDATA5,OUTP,DENS,T,
!*
!************SECOND FLUID PROPERTIES ***************
FLDATA12,PROP,DENS,4
FLDATA13,VARY,DENS,1
FLDATA12,PROP,VISC,4
FLDATA13,VARY,VISC,1
FLDATA12,PROP,COND,4
FLDATA13,VARY,COND,1
FLDATA12,PROP,SPHT,4
FLDATA13,VARY,SPHT,1
!*
FLDATA7,PROT,DENS,AIR-SI
FLDATA8,NOMI,DENS,-1
FLDATA9,COF1,DENS,0
FLDATA10,COF2,DENS,0
FLDATA11,COF3,DENS,0
FLDATA7,PROT,VISC,AIR-SI
FLDATA8,NOMI,VISC,-1
FLDATA9,COF1,VISC,0
FLDATA10,COF2,VISC,0
FLDATA11,COF3,VISC,0
FLDATA12,PROP,IVIS
FLDATA7,PROT,COND,AIR-SI
FLDATA8,NOMI,COND,-1
FLDATA9,COF1,COND,0
FLDATA10,COF2,COND,0
FLDATA11,COF3,COND,0
FLDATA7,PROT,SPHT,AIR-SI
FLDATA8,NOMI,SPHT,-1
FLDATA9,COF1,SPHT,0
FLDATA10,COF2,SPHT,0
FLDATA11,COF3,SPHT,0
!*
!***********SECOND ADVECTION PARMS***************
FLDATA,ADVM,MOME,MSU
FLDATA,ADVM,TURB,MSU
```

```
FLDATA,ADVM,PRES,MSU
FLDATA,ADVM,TEMP,MSU
!*
!*******run SECOND (30-60 iter) solution************
/SOLU
FINISH
/SOLU
SOLVE
!*******BEGIN THIRD solution (60-90 iter) options*****************
!*********THIRD SOLN OPTIONS*************
FLDATA1,SOLU,TRAN,0
FLDATA1,SOLU,FLOW,1
FLDATA1,SOLU,TEMP,1
FLDATA1,SOLU,TURB,1
FLDATA1,SOLU,COMP,0
FLDATA1,SOLU,VOF,0
FLDATA1,SOLU,SFTS,0
FLDATA1,SOLU,IVSH,0
FLDATA1,SOLU,SWRL,0
FLDATA1,SOLU,SPEC,0
FLDATA1,SOLU,ALE,0
!*
!*********THIRD EXECUTION CONTROLS*************
/COM,,Steady State Analysis,0
FLDATA2,ITER,EXEC,30,
FLDATA2,ITER,OVER,0,
FLDATA2,ITER,APPE,0,
FLDATA3,TERM,VX,0.01,
FLDATA3,TERM,VY,0.01,
FLDATA3,TERM,VZ,0.01,
FLDATA3,TERM,PRES,1e-08,
FLDATA3,TERM,TEMP,1e-08,
FLDATA3,TERM,ENKE,0.01,
FLDATA3,TERM,ENDS,0.01,
FLDATA5,OUTP,SUMF,10,
FLDATA5,OUTP,YPLU,T
!*****************ADDED TO MAKE DENSITY AN OUTPUT
FLDATA5,OUTP,DENS,T,
!*
!************THIRD FLUID PROPERTIES *************
FLDATA12,PROP,DENS,4
FLDATA13,VARY,DENS,1
FLDATA12,PROP,VISC,4
FLDATA13,VARY,VISC,1
FLDATA12,PROP,COND,4
```

```
FLDATA13,VARY,COND,1
FLDATA12,PROP,SPHT,4
FLDATA13,VARY,SPHT,1
!*
FLDATA7,PROT,DENS,AIR-SI
FLDATA8,NOMI,DENS,-1
FLDATA9,COF1,DENS,0
FLDATA10,COF2,DENS,0
FLDATA11,COF3,DENS,0
FLDATA7,PROT,VISC,AIR-SI
FLDATA8,NOMI,VISC,-1
FLDATA9,COF1,VISC,0
FLDATA10,COF2,VISC,0
FLDATA11,COF3,VISC,0
FLDATA12,PROP,IVIS
FLDATA7,PROT,COND,AIR-SI
FLDATA8,NOMI,COND,-1
FLDATA9,COF1,COND,0
FLDATA10,COF2,COND,0
FLDATA11,COF3,COND,0
FLDATA7,PROT,SPHT,AIR-SI
FLDATA8,NOMI,SPHT,-1
FLDATA9,COF1,SPHT,0
FLDATA10,COF2,SPHT,0
FLDATA11,COF3,SPHT,0
!*
!***********THIRD ADVECTION PARMS***************
FLDATA,ADVM,MOME,COLG
FLDATA,ADVM,TURB,MSU
FLDATA,ADVM,PRES,MSU
FLDATA,ADVM,TEMP,MSU
!*
!*******run THIRD (60-90 iter) solution***********
/SOLU
FINISH
/SOLU
SOLVE
!************FINAL (90 - max iter) solution******
!*********FINAL SOLN OPTIONS*************
FLDATA1,SOLU,TRAN,0
FLDATA1,SOLU,FLOW,1
FLDATA1,SOLU,TEMP,1
FLDATA1,SOLU,TURB,1
FLDATA1,SOLU,COMP,0
FLDATA1,SOLU,VOF,0
```

```
FLDATA1,SOLU,SFTS,0
FLDATA1,SOLU,IVSH,0
FLDATA1,SOLU,SWRL,0
FLDATA1,SOLU,SPEC,0
FLDATA1,SOLU,ALE,0
!*
!*********FINAL EXECUTION CONTROLS*************
/COM,,Steady State Analysis,0
FLDATA2,ITER,EXEC,120,
FLDATA2,ITER,OVER,0,
FLDATA2,ITER,APPE,0,
FLDATA3,TERM,VX,0.01,
FLDATA3,TERM,VY,0.01,
FLDATA3,TERM,VZ,0.01,
FLDATA3,TERM,PRES,1e-08,
FLDATA3,TERM,TEMP,1e-08,
FLDATA3,TERM,ENKE,0.01,
FLDATA3,TERM,ENDS,0.01,
FLDATA5,OUTP,SUMF,10,
FLDATA5,OUTP,YPLU,T
!*****************ADDED TO MAKE DENSITY AN OUTPUT
FLDATA5,OUTP,DENS,T,
!*
!************FINAL FLUID PROPERTIES *********************************
FLDATA12,PROP,DENS,4
FLDATA13,VARY,DENS,1
FLDATA12,PROP,VISC,4
FLDATA13,VARY,VISC,1
FLDATA12,PROP,COND,4
FLDATA13,VARY,COND,1
FLDATA12,PROP,SPHT,4
FLDATA13,VARY,SPHT,1
!*
FLDATA7,PROT,DENS,AIR-SI
FLDATA8,NOMI,DENS,-1
FLDATA9,COF1,DENS,0
FLDATA10,COF2,DENS,0
FLDATA11,COF3,DENS,0
FLDATA7,PROT,VISC,AIR-SI
FLDATA8,NOMI,VISC,-1
FLDATA9,COF1,VISC,0
FLDATA10,COF2,VISC,0
FLDATA11,COF3,VISC,0
FLDATA12,PROP,IVIS
FLDATA7,PROT,COND,AIR-SI
```

```
FLDATA8,NOMI,COND,-1
FLDATA9,COF1,COND,0
FLDATA10,COF2,COND,0
FLDATA11,COF3,COND,0
FLDATA7,PROT,SPHT,AIR-SI
FLDATA8,NOMI,SPHT,-1
FLDATA9,COF1,SPHT,0
FLDATA10,COF2,SPHT,0
FLDATA11,COF3,SPHT,0
!*
!**********FINAL ADVECTION PARMS***************
FLDATA,ADVM,MOME,COLG
FLDATA,ADVM,TURB,COLG
FLDATA,ADVM,PRES,COLG
FLDATA,ADVM,TEMP,COLG
!*
!*********************run FINAL (90- max iter)
solution*********************************
/SOLU
FINISH
/SOLU
SOLVE
!*********************make it go to last set************************
/POST1
FINISH
/POST1
SET,LAST

/post1
```

APPENDIX C. DISCUSSION OF ANSYS SOLVERS

The text in this appendix was taken from the ANSYS Theory reference manual (Ref. 17) to provide the reader with deeper insight into the algorithms used by FLOTRAN. The equation numbers in this section refer to equations from that reference and are not intended to be in numerical sequence with the equations in the body of the dissertation.

DERIVATION OF FLUID FLOW MATRICES

A segregated, sequential solution algorithm is used. This means that element matrices are formed, assembled and the resulting system solved for each degree of freedom separately. Development of the matrices proceeds in two parts. In the first, the form of the equations is achieved and an approach taken towards evaluating all the terms. Next, the segregated solution algorithm is outlined and the element matrices are developed from the equations.

Discretization of the Equations

The momentum, energy, species transport, and turbulence equations all have the form of a scalar transport equation. There are four types of terms: transient, advection, diffusion, and source. For the purposes of describing the discretization methods, let us refer to the variable considered as ϕ. The form of the scalar transport equation is:

Equation 7.68.

$$\frac{\partial}{\partial t}\left(\rho C_\phi \phi\right)+\frac{\partial}{\partial x}\left(\rho v_x C_\phi \phi\right)+\frac{\partial}{\partial y}\left(\rho v_y C_\phi \phi\right)+\frac{\partial}{\partial z}\left(\rho v_z C_\phi \phi\right)=$$
$$\frac{\partial}{\partial x}\left(\Gamma_\phi \frac{\partial \phi}{\partial x}\right)+\frac{\partial}{\partial y}\left(\Gamma_\phi \frac{\partial \phi}{\partial y}\right)+\frac{\partial}{\partial z}\left(\Gamma_\phi \frac{\partial \phi}{\partial z}\right)+S_\phi$$

where:

C_ϕ= transient and advection coefficient

Γ_ϕ= diffusion coefficient

S_ϕ= source terms

Transport Equation Representation below shows what the variables, coefficients, and source terms are for the transport equations. The pressure equation is derived using the continuity equation. Its form will unfold during the discussion of the segregated solver. The terms are defined in the previous section.

Since the approach is the same for each equation, only the generic transport equation need be treated. Each of the four types of terms will be outlined in turn. Since the complete derivation of the discretization method would require too much space, the methods will be outlined and the reader referred to more detailed expositions on the subjects.

Transport Equation Representation

ϕ	Meaning	DOF	C_ϕ	Γ_ϕ	S_ϕ
v_x	x-velocity	VX	1	μ_e	$\rho g_x - \partial p/\partial x + R_x$
v_y	y-velocity	VY	1	μ_e	$\rho g_y - \partial p/\partial y + R_y$
v_z	z-velocity	VZ	1	μ_e	$\rho g_z - \partial p/\partial z + R_z$
T	temperature	TEMP	Cp	K	$Q_v + E^k + W^v + \mu \Phi + \partial$

					p/∂t
k	kinematic energy	ENKE	1	μ_t / σ_k	***
ε	dissipation rate	ENDS	1	μ_t / ***	***
Y_i	species mass fraction	SP01-06	1	ρ Dm_i	0

The discretization process, therefore, consists of deriving the element matrices to put together the matrix equation:

Equation 7.69.

$$\left(\left[A_e^{transient}\right] + \left[A_e^{advection}\right] + \left[A_e^{diffusion}\right]\right)\{\phi_e\} = \left\{S_e^{\phi}\right\}$$

Galerkin's method of weighted residuals is used to form the element integrals. Denote by W^e the weighting function for the element, which is also the shape function.

Transient Term

The first of the element matrix contributions is from the transient term. The general form is simply:

Equation 7.70.

$$\left[A_e^{transient}\right] = \int W^e \frac{\partial\left(\rho C_\phi \phi\right)^e}{\partial t} d(vol)$$

A lumped mass approximation is used so that

Equation 7.71.

$$\int W^e \frac{\partial(\rho C_\phi \phi)}{\partial t} d(vol) = \frac{\partial(\rho C_\phi \phi)}{\partial t} \int W^e d(vol)$$

A backward difference scheme is used to evaluate the transient derivative. On a nodal basis, the following implicit formulation is used. The current time step is the nth time step and the expression involves the previous two time step results.

Equation 7.72.

$$\frac{\partial(\rho\phi)}{\partial t} = \frac{(\rho\phi)_{n-2}}{2\Delta t} - \frac{4(\rho\phi)_{n-1}}{2\Delta t} + \frac{3(\rho\phi)_n}{2\Delta t}$$

For a Volume of Fluid (VOF) analysis, the above equation is modified as only the results at one previous time step are needed:

Equation 7.73.

$$\frac{\partial(\rho\phi)}{\partial t} = \frac{(\rho\phi)_n}{\Delta t} - \frac{(\rho\phi)_{n-1}}{\Delta t}$$

The above first-order time difference scheme is chosen to be consistent with the current VOF advection algorithm.

The nth time step produces a contribution to the diagonal of the element matrix, while the derivatives from the previous time step form contributions to the source term.

Advection Term

Currently Flotran has three approaches to discretize the advection term. The monotone streamline upwind (MSU) approach is first order accurate and tends to produce smooth and monotone solutions. The streamline upwind/Petro-Galerkin (SUPG) approach and the collocated Galerkin (COLG) approach are second order accurate and tend to produce oscillatory solutions.

Monotone Streamline Upwind Approach (MSU)

The advection term is handled through a monotone streamline approach based on the idea that pure advection transport is along characteristic lines. It is useful to think of the advection transport formulation in terms of a quantity being transported in a known velocity field. See Streamline Upwind Approach.

Figure 7.1. Streamline Upwind Approach

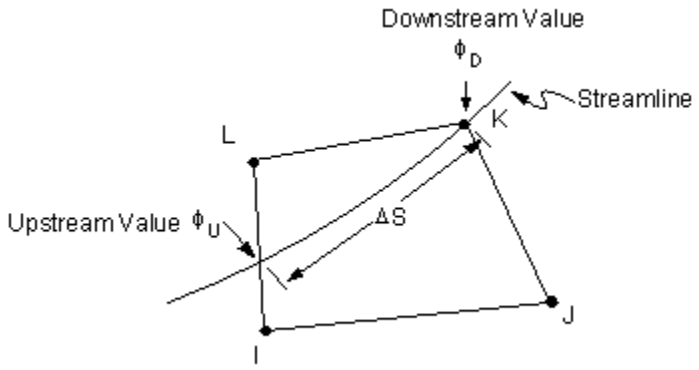

The velocity field itself can be envisioned as a set of streamlines everywhere tangent to the velocity vectors. The advection terms can therefore be expressed in terms of the streamline velocities.

In pure advection transport, one assumes that no transfer occurs across characteristic lines, i.e. all transfer occurs along streamlines. Therefore one may assume that the advection term,

Equation 7.74.

$$\frac{\partial\left(\rho C_\phi v_x \phi\right)}{\partial x} + \frac{\partial\left(\rho C_\phi v_y \phi\right)}{\partial y} + \frac{\partial\left(\rho C_\phi v_z \phi\right)}{\partial z} = \frac{\partial\left(\rho C_\phi v_s \phi\right)}{\partial s}$$

when expressed along a streamline, is constant through out an element:

Equation 7.75.

$$\left[A_e^{advection}\right] = \frac{d\left(\rho C_\phi v_s \phi\right)}{ds} \int W^e d(vol)$$

This formulation is made for every element, each of which will have only one node which gets contributions from inside the element. The derivative is calculated using a simple difference:

Equation 7.76.

$$\frac{d\left(\rho C_\phi v_s\right)}{ds} = \frac{\left(\rho C_\phi v_s \phi\right)_U - \left(\rho C_\phi v_s \phi\right)_D}{Ds}$$

where:

D = subscript for value at the downstream node

U = subscript for value taken at the location at which the streamline through the downwind node enters the element

Δs = distance from the upstream point to the downstream node

The value at the upstream location is unknown but can be expressed in terms of the unknown nodal values it is between. See Streamline Upwind Approach again.

The process consists of cycling through all the elements and identifying the downwind nodes. A calculation is made based on the velocities to see where the streamline through the downwind node came from. Weighting factors are calculated based on the proximity of the upwind location to the neighboring nodes.

Additional details are provided by Rice and Schnipke (Ref. 23).

Streamline Upwind/Petro-Galerkin Approach (SUPG)

The SUPG approach consists of a Galerkin discretization of the advection term and an additional diffusion-like perturbation term which acts only in the advection direction.

Equation 7.77.

$$\left[A_e^{advection}\right] = \int W^e \left\{\frac{\partial\left(\rho v_x C_\phi \phi\right)}{\partial x} + \frac{\partial\left(\rho v_y C_\phi \phi\right)}{\partial y} + \frac{\partial\left(\rho v_z C_\phi \phi\right)}{\partial z}\right\} d(vol) +$$

$$C_{2\tau} \int \frac{zh}{2U_{mag}} \left\{\frac{v_x \partial W^e}{\partial x} + \frac{v_y \partial W^e}{\partial y} + \frac{v_z \partial W^e}{\partial z}\right\}$$

$$\left\{\frac{v_x \partial\left(\rho C_\phi \phi\right)}{\partial x} + \frac{v_y \partial\left(\rho C_\phi \phi\right)}{\partial y} + \frac{v_z \partial\left(\rho C_\phi \phi\right)}{\partial z}\right\} d(vol)$$

where:

$C_{2\tau}$ = global coefficient set to 1.0

h = element length along advection direction

$$U_{mag} = \sqrt{v_x^2 + v_y^2 + v_z^2}$$

$$z = \begin{cases} 1 & \text{if } 0 \le Pe \le 3 \\ Pe/3 & \text{if } Pe \ge 3 \end{cases}$$

$$Pe = \frac{\rho C_\phi U_{mag} h}{2\Gamma_\phi} = \text{Peclet number}$$

It is clear from the SUPG approach that as the mesh is refined, the perturbation terms goes to zero and the Galerkin formulation approaches second order accuracy. The perturbation term provides the necessary stability which is missing in the pure Galerkin discretization. Additional details are provided by Brooks and Hughes (Ref. 24).

Collocated Galerkin Approach (COLG)

The COLG approach uses the same discretization scheme with the SUPG approach with a collocated concept. In this scheme, a second set of velocities, namely, the element-based nodal velocities are introduced. The element-based nodal velocities are made to satisfy the continuity equation, whereas the traditional velocities are made to satisfy the momentum equations.

$$\left[A_e^{advection}\right] = \int W^e \left\{\frac{\partial\left(\rho v_x^e C_\phi \phi\right)}{\partial x} + \frac{\partial\left(\rho v_y^e C_\phi \phi\right)}{\partial y} + \frac{\partial\left(\rho v_z^e C_\phi \phi\right)}{\partial z}\right\} d(vol) +$$
$$C_{2\tau} \int \frac{zh}{2U_{mag}^e} \left\{\frac{v_x^e \partial W^e}{\partial x} + \frac{v_y^e \partial W^e}{\partial y} + \frac{v_z^e \partial W^e}{\partial z}\right\}$$
$$\left\{\frac{v_x^e \partial\left(\rho C_\phi \phi\right)}{\partial x} + \frac{v_y^e \partial\left(\rho C_\phi \phi\right)}{\partial y} + \frac{v_z^e \partial\left(\rho C_\phi \phi\right)}{\partial z}\right\} d(vol)$$

Where all the parameters are defined similar to those in the SUPG approach.

In this approach, the pressure equation is derived from the element-based nodal velocities, and it is generally asymmetric even for incompressible flow problems. The collocated Galerkin approach is formulated in such a way that, for steady-state incompressible flows, exact conservation is preserved even on coarse meshes upon the convergence of the overall system.

Diffusion Terms

The expression for the diffusion terms comes from an integration over the problem domain after the multiplication by the weighting function.

Equation 7.79.

$$\text{Diffusion contribution} = \int W^e \frac{\partial}{\partial x}\left(\Gamma_\phi \frac{\partial \phi}{\partial x}\right) d(\text{vol}) + \int W^e \frac{\partial}{\partial y}\left(\Gamma_\phi \frac{\partial \phi}{\partial y}\right) d(\text{vol})$$
$$\int W^e \frac{\partial}{\partial z}\left(\Gamma_\phi \frac{\partial \phi}{\partial z}\right) d(\text{vol})$$

The x, y and z terms are all treated in similar fashion. Therefore, the illustration is with the term in the x direction. An integration by parts is applied:

Equation 7.80.

$$\int W^e \frac{\partial}{\partial x}\left(\Gamma_\phi \frac{\partial \phi}{\partial x}\right) d(\text{vol}) = \int \frac{\partial W^e}{\partial x} \Gamma_\phi \frac{\partial \phi}{\partial x} d(\text{vol})$$

Once the derivative of ϕ is replaced by the nodal values and the derivatives of the weighting function, the nodal values will be removed from the integrals

Equation 7.81.

$$\frac{\partial \phi}{\partial x} = W_x^e \phi$$

Equation 7.82.

$$W_x^e = \frac{\partial W^e}{\partial x}$$

The diffusion matrix may now be expressed as:

Equation 7.83.

$$\left[A_e^{\text{diffusion}}\right] = \int W_x^e \Gamma_\phi W_x^e + W_y^e \Gamma_\phi W_y^e + W_z^e \Gamma_\phi W_z^e \, d(\text{vol})$$

Source Terms

The evaluation of the source terms consists of merely multiplying the source terms as depicted in Streamline Upwind Approach by the weighting function and integrating over the volume.

Equation 7.84.

$$S_{\phi}^{e} = \int W^{e} S_{\phi} d(vol)$$

Segregated Solution Algorithm

Each degree of freedom is solved in sequential fashion. The equations are coupled, so that each equation is solved with intermediate values of the other degrees of freedom. The process of solving all the equations in turn and then updating the properties is called a global iteration. Before showing the entire global iteration structure, it is necessary to see how each equation is formed.

The preceding section outlined the approach for every equation except the pressure equation, which comes from the segregated velocity-pressure solution algorithm. In this approach, the momentum equation is used to generate an expression for the velocity in terms of the pressure gradient. This is used in the continuity equation after it has been integrated by parts. This nonlinear solution procedure used in FLOTRAN belongs to a general class of Semi-Implicit Method for Pressure Linked Equations (SIMPLE). There are currently two segregated solution algorithms available. One is the original SIMPLEF algorithm, and the other is the enhanced SIMPLEN algorithm.

The incompressible algorithm is a special case of the compressible algorithm. The change in the product of density and velocity from iteration to the next is approximating by considering the changes separately through a linearization process. Denoting by the superscript * values from the previous iteration, in the x direction, for example, results:

Equation 7.85.

$$\rho v_x = \rho v_x^* + \rho^* v_x - \rho^* v_x^*$$

The continuity equation becomes:

Equation 7.86.

$$\frac{\partial \rho}{\partial t} + \frac{\partial\left(\rho^* v_x\right)}{\partial x} + \frac{\partial\left(\rho v_x^*\right)}{\partial x} + \frac{\partial\left(\rho^* v_y\right)}{\partial y} + \frac{\partial\left(\rho v_y^*\right)}{\partial y} + \frac{\partial\left(\rho^* v_z\right)}{\partial z} + \frac{\partial\left(\rho v_z^*\right)}{\partial z} - \frac{\partial\left(\rho^* v_x^*\right)}{\partial x} - \frac{\partial\left(\rho^* v_y^*\right)}{\partial y} - \frac{\partial\left(\rho^* v_z^*\right)}{\partial z} = 0$$

The transient term in the continuity equation can be expressed in terms of pressure immediately by employing the ideal gas relationship:

Equation 7.87.

$$\int W^e \frac{\partial \rho}{\partial t} d(vol) = \frac{\partial}{\partial t} \int W^e \frac{P}{RT} d(vol)$$

The backward differencing process is then applied directly to this term.

Application of Galerkin's method to the remaining terms yields:

Equation 7.88.

$$\int W\left[\frac{\partial\left(\rho^{*}v_{x}\right)}{\partial x}+\frac{\partial\left(\rho^{*}v_{y}\right)}{\partial y}+\frac{\partial\left(\rho^{*}v_{z}\right)}{\partial z}\right]d(vol)$$
$$+\int W\left[\frac{\partial\left(\rho v_{x}^{*}\right)}{\partial x}+\frac{\partial\left(\rho v_{y}^{*}\right)}{\partial y}+\frac{\partial\left(\rho v_{z}^{*}\right)}{\partial z}\right]d(vol)$$
$$-\int W\left[\frac{\partial\left(\rho^{*}v_{x}^{*}\right)}{\partial x}+\frac{\partial\left(\rho^{*}v_{y}^{*}\right)}{\partial y}+\frac{\partial\left(\rho^{*}v_{z}^{*}\right)}{\partial z}\right]d(vol)$$

There are thus three groups of terms. In the first group, terms with the derivatives of the unknown new velocities must be integrated by parts to remove the derivative. The integration by parts of just these terms becomes:

Equation 7.89.

$$\int W\left[\frac{\partial\left(\rho^{*}v_{x}\right)}{\partial x}+\frac{\partial\left(\rho^{*}v_{y}\right)}{\partial y}+\frac{\partial\left(\rho^{*}v_{z}\right)}{\partial z}\right]d(vol)$$
$$=\int W\left[\rho^{*}v_{x}+\rho^{*}v_{y}+\rho^{*}v_{z}\right]d(area)$$
$$-\int\left[\left(\rho^{*}v_{x}\right)\frac{\partial W}{\partial x}+\left(\rho^{*}v_{y}\right)\frac{\partial W}{\partial y}+\left(\rho^{*}v_{z}\right)\frac{\partial W}{\partial z}\right]d(vol)$$

Illustrating with the x direction, the unknown densities in the second group expressed in terms of the pressures are:

Equation 7.90.

$$\int W\frac{\partial}{\partial x}\left(\rho v_{x}^{*}\right)d(vol)=\int\frac{W}{R}\frac{\partial}{\partial x}\left(v_{x}^{*}\frac{P}{T}\right)d(vol)$$

In the third group, the values from the previous iteration are used to evaluate the integrals.

The next step is the derivation of an expression for the velocities in terms of the pressure gradient. When the momentum equations are solved, it is with a previous value of pressure. Write the algebraic expressions of the momentum equations assuming that the coefficient matrices consist of the transient, advection and diffusion contributions as before, and all the source terms are evaluated except the pressure gradient term.

Equation 7.91.

$$Av_x = s_\phi - \sum_{e=1}^{E} W \left(\frac{\partial P}{\partial x} \right)^e d(vol)$$

Equation 7.92.

$$Av_y = s_\phi - \sum_{e=1}^{E} W \left(\frac{\partial P}{\partial y} \right)^e d(vol)$$

Equation 7.93.

$$Av_z = s_\phi - \sum_{e=1}^{E} W \left(\frac{\partial P}{\partial z} \right)^e d(vol)$$

Each of these sets represents a system of N algebraic equations for N unknown velocities. It is possible, after the summation of all the element quantities, to show an expression for each velocity component at each node in terms of the velocities of its neighbors, the source terms which have been evaluated, and the pressure drop. Using the subscript "i" to denote the nodal equation, for i = 1 to N, where N is the number of fluid nodes and subscript "j" to denote its neighboring node:

For SIMPLEF algorithm:

Equation 7.94.

$$v_{x_i} = \hat{v}_{x_i} - \frac{1}{a_{ii}^x} \int W \left(\frac{\partial p}{\partial x} \right) d(vol)$$

Equation 7.95.

$$v_{y_i} = \hat{v}_{y_i} - \frac{1}{a_{ii}^y} \int W \left(\frac{\partial p}{\partial y} \right) d(vol)$$

Equation 7.96.

$$v_{z_i} = \hat{v}_{z_i} - \frac{1}{a_{ii}^z} \int W \left(\frac{\partial p}{\partial z} \right) d(vol)$$

For SIMPLEN algorithm:

$$v_{x_i} = \hat{v}_{x_i} - \frac{1}{\frac{a_{ii}^x}{r^x} + \sum_j^{j \neq i} a_{ij}^x} \int_\Omega W \left(\frac{\partial p}{\partial x} \right) d(vol)$$

$$v_{y_i} = \hat{v}_{y_i} - \frac{1}{\frac{a_{ii}^y}{r^y} + \sum_j^{j \neq i} a_{ij}^y} \int_\Omega W \left(\frac{\partial p}{\partial y} \right) d(vol)$$

$$v_{z_i} = \hat{v}_{z_i} - \frac{1}{\frac{a_{ii}^z}{r^z} + \sum_j^{j \neq i} a_{ij}^z} \int_\Omega W \left(\frac{\partial p}{\partial z} \right) d(vol)$$

where for SIMPLEF algorithm:

Equation 7.100.

$$\hat{v}_{x_i} = \frac{-\sum_{j}^{j\neq i} a_{ij}^{x} v_{x_j} + S_x}{a_{ii}^{x}}$$

Equation 7.101.

$$\hat{v}_{y_i} = \frac{-\sum_{j}^{j\neq i} a_{ij}^{y} v_{y_j} + S_y}{a_{ii}^{y}}$$

Equation 7.102.

$$\hat{v}_{z_i} = \frac{-\sum_{j}^{j\neq i} a_{ij}^{z} v_{z_j} + S_z}{a_{ii}^{z}}$$

and or SIMPLEN algorithm:

$$\hat{v}_{x_i} = \frac{-\sum_{j}^{j\neq i} a_{ij}^{x} (v_{x_j} - v_{x_i}) + b_i^{x}}{\frac{a_{ii}^{x}}{r^{x}} + \sum_{j}^{j\neq i} a_{ij}^{x}}$$

$$\hat{v}_{y_i} = \frac{-\sum_{j}^{j\neq i} a_{ij}^{y} (v_{y_j} - v_{y_i}) + b_i^{y}}{\frac{a_{ii}^{y}}{r^{y}} + \sum_{j}^{j\neq i} a_{ij}^{y}}$$

$$\hat{v}_{z_i} = \frac{-\sum_{j}^{j\neq i} a_{ij}^{z}\left(v_{z_j} - v_{z_i}\right) + b_i^z}{\frac{a_{ii}^{z}}{r^{z}} + \sum_{j}^{j\neq i} a_{ij}^{z}}$$

Here the a_{ij} represent the values in the x,y and z coefficient matrices for the three momentum equations, r is the relaxation factor, and b_i is the modified source term taking into effect the relaxation factors.

For the purposes of this expression, the neighboring velocities for each node are considered as being known from the momentum equation solution. At this point, the assumption is made that the pressure gradient is constant over the element, allowing it to be removed from the integral. This means that only the weighting function is left in the integral, allowing a pressure coefficient to be defined in terms of the main diagonal of the momentum equations and the integral of the weighting function:

For SIMPLEF algorithm:

Equation 7.106.

$$M_x = \frac{1}{a_{ii}^{x}} \sum_{e=1}^{N} W\, d(vol)$$

Equation 7.107.

$$M_y = \frac{1}{a_{ii}^{y}} \sum_{e=1}^{N} W\, d(vol)$$

Equation 7.108.

$$M_z = \frac{1}{a_{ii}^{z}} \sum_{e=1}^{N} W\, d(vol)$$

For SIMPLEN algorithm:

$$M_x = \frac{1}{\frac{a_{ii}^x}{r^x} + \sum_{j}^{j \neq i} a_{ij}^x} \sum_{e=1}^{N} W\, d(vol)$$

$$M_y = \frac{1}{\frac{a_{ii}^y}{r^y} + \sum_{j}^{j \neq i} a_{ij}^y} \sum_{e=1}^{N} W\, d(vol)$$

$$M_z = \frac{1}{\frac{a_{ii}^z}{r^z} + \sum_{j}^{j \neq i} a_{ij}^z} \sum_{e=1}^{N} W\, d(vol)$$

Therefore, expressions for unknown nodal velocities have been obtained in terms of the pressure drop and a pressure coefficient.

Equation 7.112.

$$v_x = \hat{v}_x - M_x \frac{\partial P}{\partial x}$$

Equation 7.113.

$$v_y = \hat{v}_y - M_y \frac{\partial P}{\partial y}$$

Equation 7.114.

$$v_z = \hat{v}_z - M_z \frac{\partial P}{\partial z}$$

These expressions are used to replace the unknown velocities in the continuity equation to convert it into a pressure equation. The terms coming from the unknown velocities

(replaced with the pressure gradient term) and with the unknown density (expressed in terms of the pressure) contribute to the coefficient matrix of the pressure equation while all the remaining terms will contribute to the forcing function.

The entire pressure equation can be written on an element basis, replacing the pressure gradient by the nodal pressures and the derivatives of the weighting function, putting all the pressure terms on the left hand side and the remaining terms on the right hand side (equation 7.115).

Equation 7.115.

$$
\begin{aligned}
&[P]^e \int \left[\frac{\partial W}{\partial x} \rho^* M_x \frac{\partial W}{\partial x} + \frac{\partial W}{\partial y} \rho^* M_y \frac{\partial W}{\partial y} + \frac{\partial W}{\partial z} \rho^* M_z \frac{\partial W}{\partial z} \right] d(vol)^e \\
&\quad + \int \frac{W}{R} \left[\frac{\partial}{\partial x} \left(v_x^* \frac{P}{T} \right) + \frac{\partial}{\partial y} \left(v_y^* \frac{P}{T} \right) + \frac{\partial}{\partial z} \left(v_z^* \frac{P}{T} \right) \right] d(vol)^e \\
&\quad = \int \left[\frac{\partial W}{\partial x} \rho^* \hat{v}_x + \frac{\partial W}{\partial y} \rho^* \hat{v}_y + \frac{\partial W}{\partial z} \rho^* \hat{v}_z \right] d(vol)^e \\
&\quad + \int W \left[\frac{\partial}{\partial x} \left(\rho^* v_x^* \right) + \frac{\partial}{\partial y} \left(\rho^* v_y^* \right) + \frac{\partial}{\partial z} \left(\rho^* v_z^* \right) \right] d(vol)^e \\
&\quad - \int W \left[\rho^* v_x \right]^s d(area)^s - \int W \left[\rho^* v_y \right]^s d(area)^s - \int W \left[\rho^* v_z \right]^s d(area)^s
\end{aligned}
$$

It is in the development of the forcing function that the solution to the momentum equation comes into play: the "hat" velocities contribute to the source term of the pressure equation.

In the incompressible case, the second and fourth lines of the above equation disappear because the linearization defined in equation (7.85) is unnecessary. The second line is treated with the same advection routines that are used for the momentum equation.

The final step is the velocity update. After the solution for pressure equation, the known pressures are used to evaluate the pressure gradients. In order to ensure that a velocity

field exists which conserves mass, the pressure term is added back into the "hat" velocities:

For SIMPLEF algorithm:

Equation 7.116.

$$v_x = \hat{v}_x - \frac{1}{a_{ii}^x}\int\left(W\frac{\partial W}{\partial x}\right)d(vol)^e\,[P]^e$$

Equation 7.117.

$$v_y = \hat{v}_y - \frac{1}{a_{ii}^y}\int\left(W\frac{\partial W}{\partial y}\right)d(vol)^e\,[P]^e$$

Equation 7.118.

$$v_z = \hat{v}_z - \frac{1}{a_{ii}^z}\int\left(W\frac{\partial W}{\partial z}\right)d(vol)^e\,[P]^e$$

For SIMPLEN algorithm:

$$v_x = \hat{v}_x - \frac{1}{\frac{a_{ii}^x}{r^x} + \sum_{j}^{j\neq i} a_{ij}^x}\int\left(W\frac{\partial W}{\partial x}\right)d(vol)^e\,[P]^e$$

$$v_y = \hat{v}_y - \frac{1}{\frac{a_{ii}^y}{r^y} + \sum_{j}^{j\neq i} a_{ij}^y}\int\left(W\frac{\partial W}{\partial y}\right)d(vol)^e\,[P]^e$$

$$v_z = \hat{v}_z - \frac{1}{\frac{a_{ii}^z}{r^z} + \sum_{j}^{j \neq i} a_{ij}^z} \int \left(W \frac{\partial W}{\partial z} \right) d(vol)^e [P]^e$$

The global iterative procedure is summarized below.

- Formulate and solve $\hat{v}_x$ equation approximately
- Formulate and solve $\hat{v}_y$ equation approximately
- Formulate and solve $\hat{v}_z$ equation approximately
- Formulate pressure equation using $\hat{v}_x$, $\hat{v}_y$, and $\hat{v}_z$
- Solve pressure equation for P
- Update velocities based on $\hat{v}_x$, $\hat{v}_y$, $\hat{v}_z$, and P
- Formulate and solve energy equation for T
- Solve species transport equations
- Update temperature dependent properties
- Solve turbulence equations for k and ε
- Update effective properties based on turbulence solution
- Check rate of change of the solution (convergence monitors)
- End of global iteration

APPENDIX D. EXPERIMENTAL DETAILS

EXPERIMENTAL RIG OVERVIEW

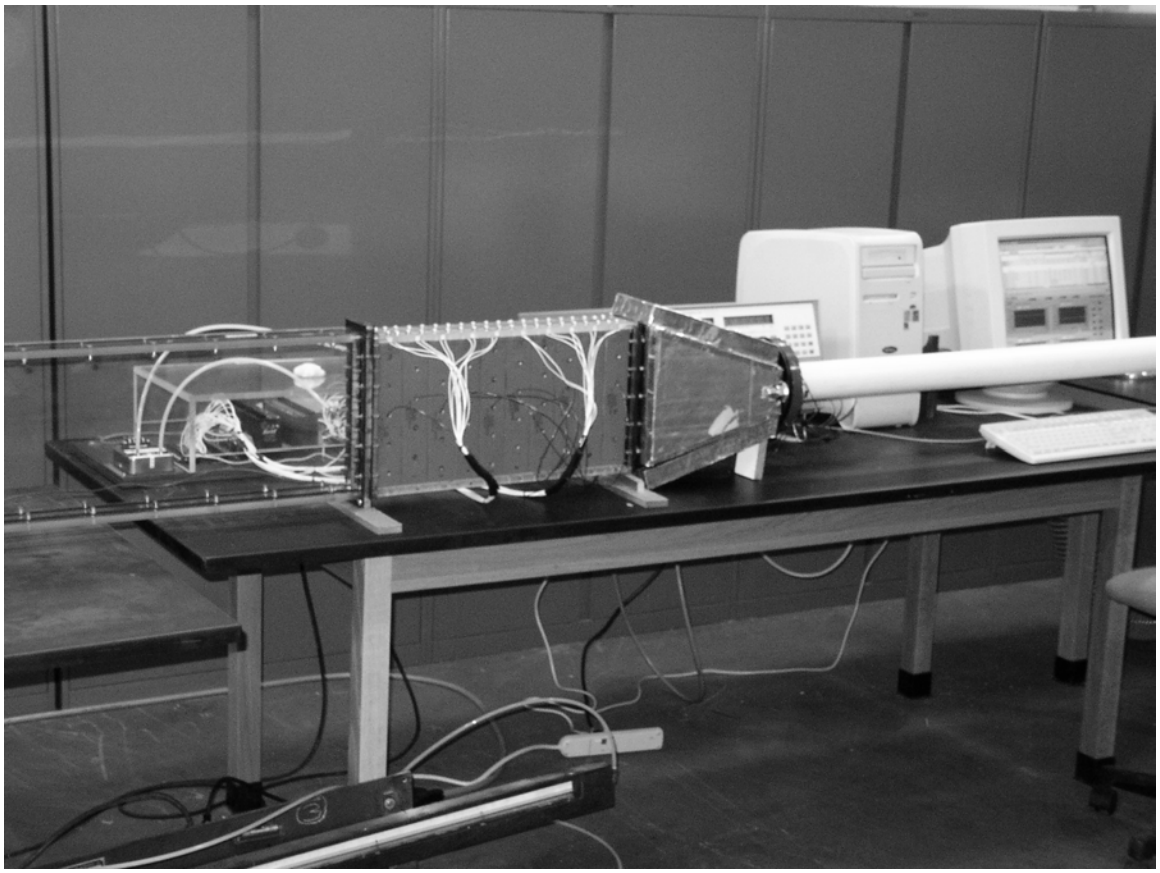

This photograph shows the test section installed between the plexiglass inlet duct and the exit chamber. Note the insulation on the chamber to minimize hat loss to the room. The white PVC pipe extending from the exit chamber leads to the flowmeter (not pictured here). Although not visible, the thermocouples measuring the outlet air temperature are located at the junction of the exit chamber and the PVC pipe. Behind the apparatus (from left to right) are the relay board, relay controller and data acquisition computer. The inclined manometer can be seen at the lower edge of this photo.

TEST SECTION DETAIL

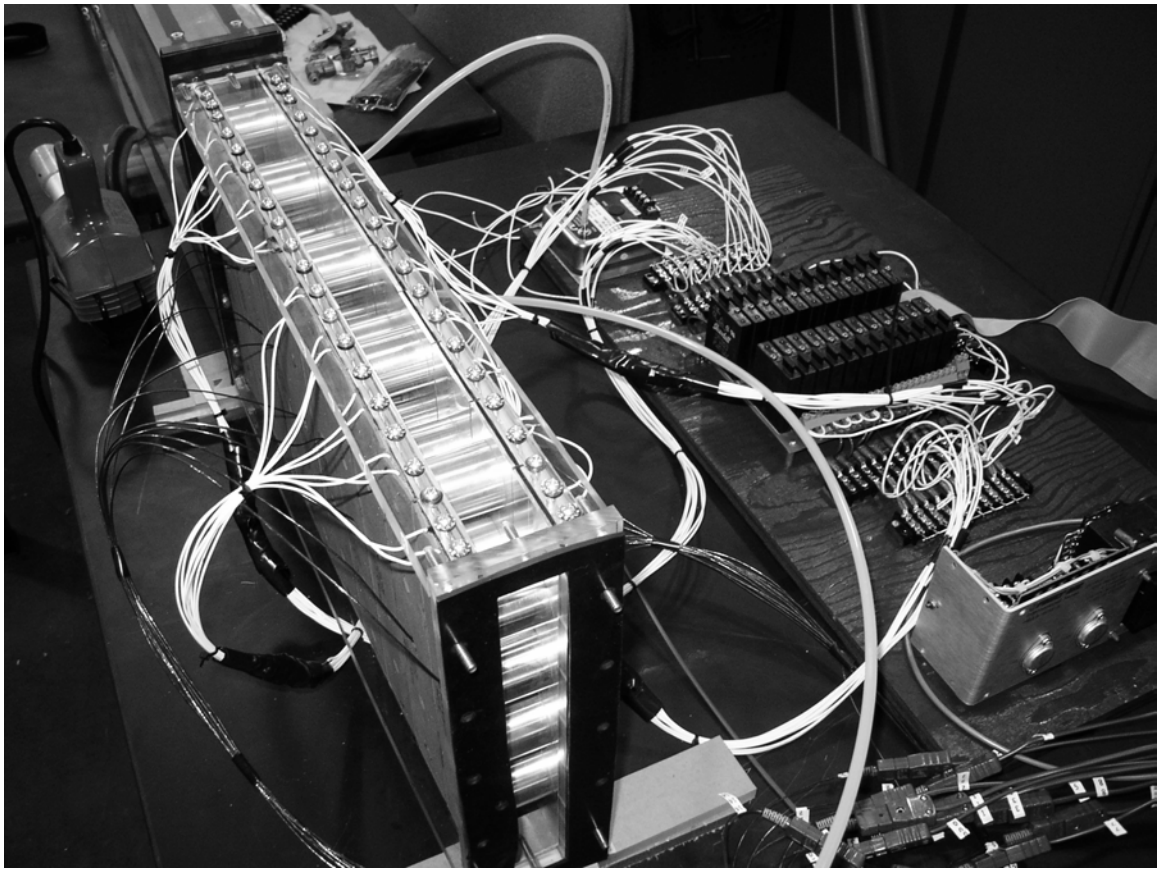

This photo shows the test section disconnected from the inlet and outlet ducts. To the right of the test section is the relay board. On this board are mounted the 20 independent relays to energize the strip heaters. During normal operation this board is covered by a plexiglass cover to prevent inadvertent contact with the electrical leads.

THERMOCOUPLE PLACEMENT AT TEST ARRAY OUTLET

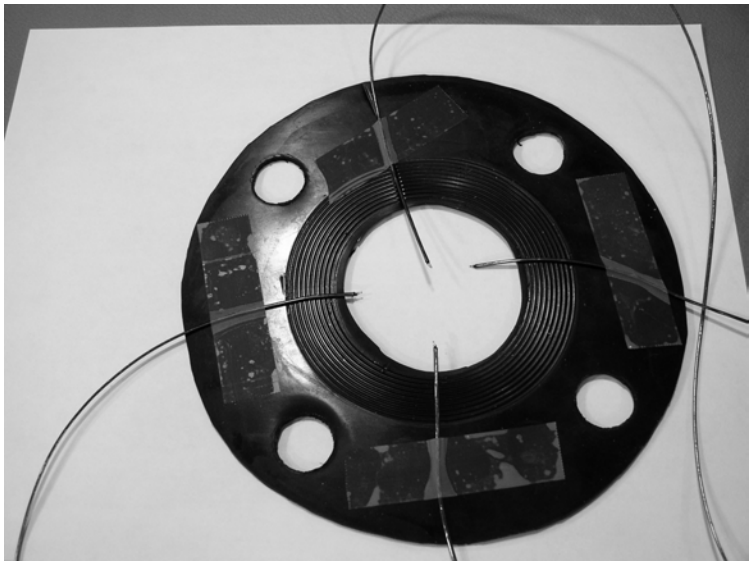

This photo shows the placement of the four thermocouples used to find the average outlet temperature. The thermocouples are taped to the gasket and placed between the exit duct and PVC pipe that leads to the flowmeter. Although the flow is expected to be well mixed by this point care was taken to capture various points in the flow. As such the thermocouples are placed to measure four different radii (R) in the pipe entrance. As seen in the photo, these locations are approximately equal to R, R/2, R/4 and R/8.

FLOWMETER INTERIOR VIEW

This photo shows the interior of the turbine flowmeter.

REYNOLDS NUMBER CONTROL

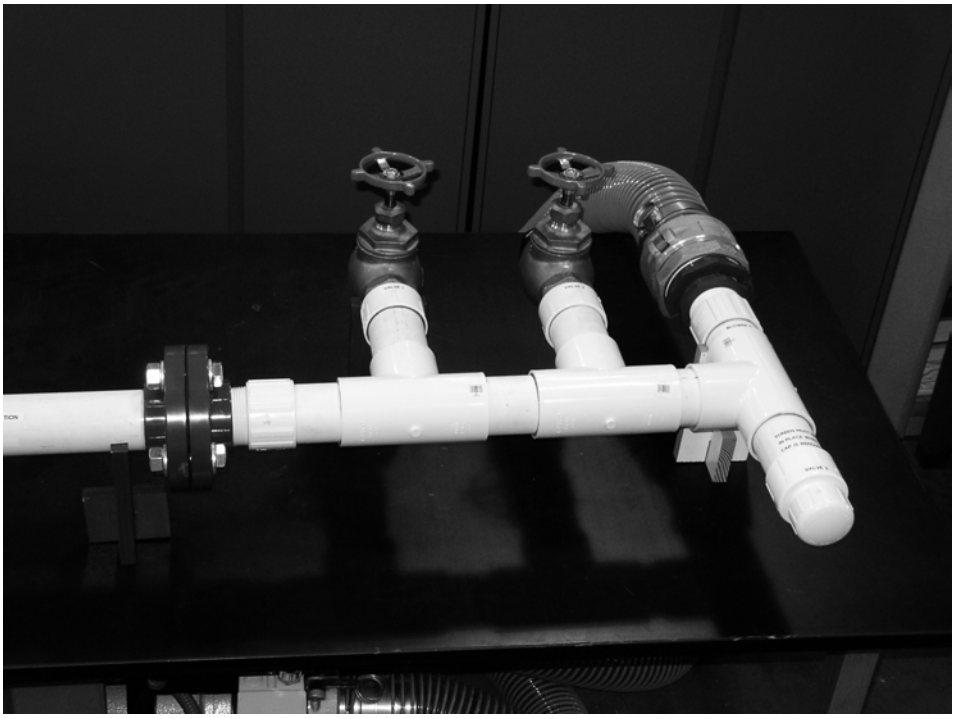

These bleed valves were used in conjunction with inlet filters to control the mass flow rate through the test array. In this way the blower (below the lab table) was operated at constant velocity for all runs. This provided consistency and repeatability between runs.

APPENDIX E. UNCERTAINTY ANALYSIS

The uncertainty analysis was conducted using the following general governing equation taken from Ref. 21:

$$w_R = \left[\left(\frac{\partial R}{\partial x_1} w_1 \right)^2 + \left(\frac{\partial R}{\partial x_2} w_2 \right)^2 + \cdots + \left(\frac{\partial R}{\partial x_n} w_n \right)^2 \right]^{1/2}$$

where R is a given function of the independent variables $x_1, x_2, \ldots x_n$

and w_R is the uncertainty.

Using this method, the uncertainty was calculated for Reynolds number, Nusselt number and friction factor.

REYNOLDS NUMBER UNCERTAINTY CALCULATION:

Given that $\mathrm{Re}_{Dh} = \dfrac{\rho \bar{U} D_h}{\mu}$,

and $\dfrac{w_{\mathrm{Re}_{Dh}}}{\mathrm{Re}_{Dh}} = \left[\left(\dfrac{w_\rho}{\rho} \right)^2 + \left(\dfrac{w_{\bar{U}}}{\bar{U}} \right)^2 + \left(\dfrac{w_{Dh}}{D_h} \right)^2 \right]^{1/2}$ (note that w_μ is assumed to be zero)

it is necessary to find the uncertainty for each variable.

Density: $\rho = \dfrac{p}{RT}$ therefore, $\dfrac{\partial \rho}{\partial p} = \dfrac{1}{RT}$ and $\dfrac{\partial \rho}{\partial T} = -\dfrac{1}{RT^2}$

Then, $\dfrac{w_\rho}{\rho} = \left[\left(\dfrac{w_p}{p} \right)^2 + \left(\dfrac{w_T}{T} \right)^2 \right]^{1/2} = \left[\left(\dfrac{1.25}{101350} \right)^2 + \left(\dfrac{0.5}{300} \right)^2 \right]^{1/2} = 0.0017$

Velocity: To find the uncertainty in velocity, the uncertainty in volumetric flow rate and average area must be known since $\bar{U} = \dfrac{\dot{\forall}}{\bar{A}}$ and $\dfrac{w_{\bar{U}}}{\bar{U}} = \left[\left(\dfrac{w_{\dot{\forall}}}{\dot{\forall}} \right)^2 + \left(\dfrac{w_{\bar{A}}}{\bar{A}} \right)^2 \right]^{1/2}$

Volumetric flow rate: $\dot{\forall} = \frac{V_f}{k_f}$ where V_f is the flowmeter voltage output and k_f is the flowmeter constant (pulses/ft^3).

From the manufacturer's calibration sheet, $w_v = 0.03$ volts and $w_k = 1.2$ pulses/ft^3 and $k_f = 132$ pulses/ft^3. Therefore:

$$\frac{w_{\dot{\forall}}}{\dot{\forall}} = \left[\left(\frac{w_V}{V_f}\right)^2 + \left(\frac{w_k}{k_f}\right)^2\right]^{1/2} \approx \frac{w_V}{V_f} = \frac{0.03}{V_f}$$

Average area: $\bar{A} = \frac{V_{open}}{L}$ where L is the array length

$$\frac{w_{\bar{A}}}{\bar{A}} = \left[\left(\frac{w_{Vopen}}{V_{open}}\right)^2 + \left(\frac{w_L}{L}\right)^2\right]^{1/2}$$

$$\frac{w_{Vopen}}{V_{open}} = \left[\left(\frac{w_x}{x}\right)^2 + \left(\frac{w_y}{y}\right)^2 + \left(\frac{w_z}{z}\right)^2\right]^{1/2} = \left[\left(\frac{3}{500}\right)^2 + \left(\frac{1}{250}\right)^2 + \left(\frac{0.5}{33}\right)^2\right]^{1/2} = 0.017$$

where *x, y* and *z* are dimensions (in mm) in all three axes.

$$\frac{w_L}{L} = \frac{3}{500} = 0.006$$

so, $\frac{w_{\bar{A}}}{\bar{A}} = \left[(0.017)^2 + (0.006)^2\right]^{1/2} = 0.018$

therefore,

$$\frac{w_{\bar{U}}}{\bar{U}} = \left[\left(\frac{w_{\dot{\forall}}}{\dot{\forall}}\right)^2 + \left(\frac{w_{\bar{A}}}{\bar{A}}\right)^2\right]^{1/2} = \left[\left(\frac{0.03}{V_f}\right)^2 + (0.018)^2\right]^{1/2} \approx \frac{0.03}{V_f}$$

For hydraulic diameter: $D_h = \frac{4V_{open}}{A_w}$ and $\frac{w_{Dh}}{D_h} = \left[\left(\frac{w_{Vopen}}{V_{open}}\right)^2 + \left(\frac{w_{Aw}}{A_w}\right)^2\right]^{1/2}$

Where $\frac{w_{Aw}}{A_w} = \left[\left(\frac{w_x}{x}\right)^2 + \left(\frac{w_y}{y}\right)^2\right]^{1/2} = \left[\left(\frac{3}{500}\right)^2 + \left(\frac{1}{250}\right)^2\right]^{1/2} = 0.007$

So $\frac{w_{Dh}}{D_h} = \left[\left(\frac{w_{Vopen}}{V_{open}}\right)^2 + \left(\frac{w_{Aw}}{A_w}\right)^2\right]^{1/2} = \left[(0.017)^2 + (0.007)^2\right]^{1/2} = 0.018$

Substituting:

$$\frac{w_{\mathrm{Re}_{Dh}}}{\mathrm{Re}_{Dh}} = \left[\left(\frac{w_\rho}{\rho}\right)^2 + \left(\frac{w_{\bar{U}}}{\bar{U}}\right)^2 + \left(\frac{w_{Dh}}{D_h}\right)^2\right]^{1/2} = \left[(0.0017)^2 + \left(\frac{0.03}{V_f}\right)^2 + (0.018)^2\right]^{1/2}$$

So the relative Reynolds number uncertainty decreases as flowmeter voltage increases corresponding to higher Reynolds number values. The following table shows the range of Reynolds numbers and associated uncertainty values.

Re_{Dh}	Flowmeter voltage	Relative uncertainty
5,000	0.66	4.9%
45,000	6.30	1.9%

NUSSELT NUMBER UNCERTAINTY CALCULATIONS:

Given $Nu_{Dh} = \frac{hD_h}{k}$, $\frac{w_{Nu_{Dh}}}{Nu_{Dh}} = \left[\left(\frac{w_h}{h}\right)^2 + \left(\frac{w_{Dh}}{D_h}\right)^2\right]^{1/2}$ since k is considered constant.

Also, $h = \frac{Q}{A_w \Delta T_{lm}}$ and $\frac{w_h}{h} = \left[\left(\frac{w_Q}{Q}\right)^2 + \left(\frac{w_{Aw}}{A_w}\right)^2 + \left(\frac{w_{\Delta T_{lm}}}{\Delta T_{lm}}\right)^2\right]^{1/2}$

So uncertainty values must be found for Q, A_w and ΔT_{lm}.

Since Q is based on the time that the strip heaters are energized, the relative uncertainty is approximately equal to the smallest increment of "on" time, or 8.547 seconds, divided by total run time. For all experimental runs, total run time was 20 minutes.

Therefore, $\frac{w_Q}{Q} = \frac{8.547}{1200} = 0.007$

For uncertainty in temperature measurements, both the 6 and 12 degree temperature difference cases must be considered. With an advertised uncertainty of 0.5K for each thermocouple, the relative uncertainty is approximately 0.083 for the 6 degree case and 0.042 for the 12 degree case.

Since these values are much larger than the relative uncertainty values for heat flux and wetted area, the relative uncertainty for heat transfer coefficient can be reduced to: $\frac{w_h}{h} = \left[\left(\frac{w_Q}{Q}\right)^2 + \left(\frac{w_{Aw}}{A_w}\right)^2 + \left(\frac{w_{\Delta T_{lm}}}{\Delta T_{lm}}\right)^2\right]^{1/2} \approx \left[\left(\frac{w_{\Delta T_{lm}}}{\Delta T_{lm}}\right)^2\right]^{1/2}$

The same argument holds true for Nusselt number uncertainty so, for the 6 and 12 degree temperature difference cases, $\frac{w_{Nu_{Dh}}}{Nu_{Dh}}$ = 8.3 and 4.2 % respectively.

FRICTION FACTOR UNCERTAINTY CALCULATIONS:

For $f = \frac{2\Delta p D_h}{\rho \bar{U}^2 L}$,

$$\frac{w_f}{f} = \left[\left(\frac{w_{\Delta p}}{\Delta p}\right)^2 + \left(\frac{w_{Dh}}{D_h}\right)^2 + \left(\frac{w_\rho}{\rho}\right)^2 + \left(\frac{w_L}{L}\right)^2\right]^{1/2}$$

In the above equation, all uncertainties have been found while calculating uncertainties for Reynolds number and Nusselt number with the exception of pressure drop. Using the inclined manometer, pressure drop uncertainty is constant and is approximately 1.25 Pa as the column was graduated in 0.01 inches of water. Therefore, the relative uncertainty for pressure drop is dependent on absolute pressure drop as shown in the following equation:

$$\frac{w_f}{f} = \left[\left(\frac{w_{\Delta p}}{\Delta p}\right)^2 + \left(\frac{w_{Dh}}{D_h}\right)^2 + \left(\frac{w_\rho}{\rho}\right)^2 + \left(\frac{w_L}{L}\right)^2\right]^{1/2} = \left[\left(\frac{1.25Pa}{\Delta p}\right)^2 + (0.018)^2 + (0.0017)^2 + \left(\frac{3}{500}\right)^2\right]^{1/2}$$

The following table provides relative uncertainty values for friction factor for various pin configurations at each Reynolds number limit.

Pin type	ReDh	Δp (Pa)	Relative uncertainty
33 mm round	5000 - 45000	40 - 2500	3.3 - 0.62%
16.5 mm round	5000 - 45000	38 - 840	3.4 - 0.64%
10 mm round	5000 - 45000	6.4 - 480	20.0 – 0.68%
airfoil	5000 - 45000	4.5 - 200	25 - 0.78%

THIS PAGE INTENTIONALLY LEFT BLANK

APPENDIX F. SAMPLE APPLICATION

WETTED AREA MAGNIFICATION

One way of characterizing pin-fin heat exchanger utility is by thinking of the array as a wetted area multiplier. Consider a requirement to transfer heat across a specific area via forced convection such as in an electronic component cooling application. Without a pin-fin array, this would dictate a specific heat transfer coefficient that may not be attainable depending on the heat flux requirement. By employing a pin-fin array, the wetted area can be magnified to the extent that a reasonable average heat transfer coefficient would satisfy the cooling requirement. Geometrically, this wetted area magnification factor can be resolved on a unit cell basis.

First, consider the definition of area density or α:

$$\alpha = \frac{A_{wetted}}{V_{total}}$$

and $V_{total} = A_{face} * H$

where A_{face} is the heat exchanger "footprint" with a specified heat flux requirement and H is the heat exchanger height.

Thus the magnification factor would be:

$$\alpha H = \frac{A_{wetted}}{A_{face}}$$

AIRFOIL-SHAPED PIN-FIN CONFIGURATION

The diagram below shows a unit cell for an airfoil-shaped pin-fin array. Note that there are two pins in the cell. It is "*S*" wide, "2*X*" long and "*H*" high.

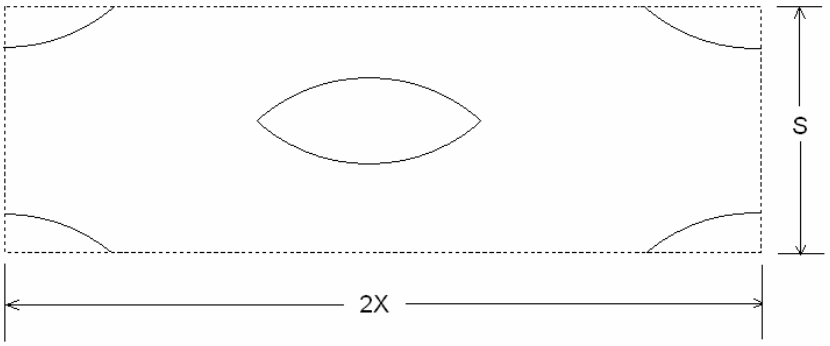

Using the airfoil dimensions shown below, it is possible to derive an expression for the area magnification factor, αH . Although this is derived for an airfoil-shaped pin array, the relationship can also be applied to a circular pin-fin array by letting $R_y = 0$.

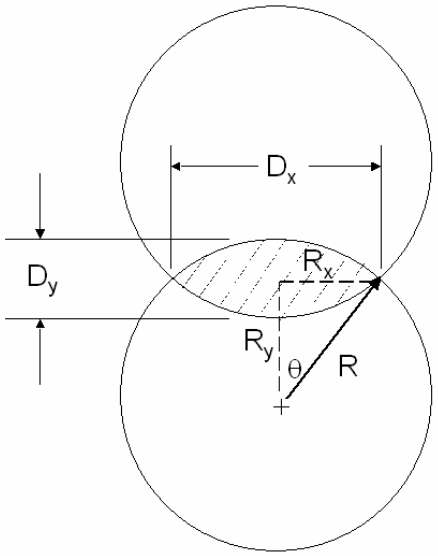

Wetted area calculation:

$$A_{wetted} = 2 * A_{endwall} - 4 * A_{pf} + 2 * A_{pinsides}$$

where $A_{endwall} = 2XS$

pin footprint, $A_{pf} = 2R^2\theta - 2R_xR_y$

where $\theta = \tan^{-1}\left(\frac{R_x}{R_y}\right)$

(note that for a circular pin, A_{pf} reduces to πR^2)

and the surface area of the pin sides, $A_{pinsides} = 4HR\theta$

(for the circular pin, $A_{pinsides}$ reduces to $2\pi R$)

Thus,

$$\alpha H = \frac{4XS - 4\left(2 * R^2\theta - R_xR_y\right) + 2\left(4HR\theta\right)}{2XS}$$

But, $LR = \frac{D_X}{X}$, $AR = \frac{D_x}{D_y} = \frac{Rx}{R - R_y}$, and $R = \frac{R_x}{\sin\theta}$

Substituting,

$$\alpha H = 2 - \frac{\frac{2\theta AR^2}{\sin^2\theta} - AR\left(AR^2 - 1\right) - \frac{4\theta AR}{\sin\theta}\left(\frac{H}{D_y}\right)}{\frac{2AR}{LR}\left(\frac{S}{D_y}\right)}$$

where $D_y = D$ for the airfoil-shaped pin-fin

and $\theta = \tan^{-1}\left[\frac{4}{D_y\left(AR^2 - 1\right)}\right]$

While this equation looks imposing, it can be used to evaluate the trends in magnification factor when *S/D, H/D, LR* and *AR* are varied. Table 17 shows the changes in area magnification factor as these basic parameters are changed. Magnification factor increases as *S/D* and *LR* are decreases and *H/D* and *AR* are increased.

Table 17 Magnification factor trends, airfoil-shaped pins

S/D	*H/D*	*LR*	*AR*	αH
2	1	0.7	6.2	2.24
5	1	0.7	6.2	2.10
5	4	0.7	6.2	2.95
5	4	0.5	6.2	2.68
5	4	0.9	6.2	3.22
5	4	0.9	2.4	3.35
3	4	0.7	4.24	3.40
2	4	0.9	2.4	5.38
2	16	0.9	2.4	13.85
2	32	0.9	2.4	26.17

CIRCULAR PIN-FIN CONFIGURATION

For the circular pin case, with $R_y = 0$,

$$\alpha H = 2 + \frac{\pi}{(X/D)(S/D)}\left(\frac{H}{D} - \frac{1}{2}\right)$$

Here, it can be seen that the magnification factor can be increased by increasing *H/D* and decreasing *X/D* and *S/D*. However, as shown previously, better performance in terms of *h* vs. *E* can be achieved with wide spacing pin ratios. Therefore, the best practical solution will likely be a tradeoff between desired heat transfer and allowable pressure drop. By programming the magnification factor equation and Nusselt number and friction factor correlations into a spreadsheet such a trade study could be accomplished for a given application.

SAMPLE APPLICATION

Consider an example where the heat flux requirement is 1.6 W/cm^2 with a 40 degree log mean temperature difference. This defines an effective heat transfer coefficient or h_{eff}, requirement of 400 W/m^{2}K.

The required heat transfer coefficient, $h = \frac{h_{eff}}{\alpha H}$

Three different pin spacings and 2 pin height ratios can be compared to evaluate the best configuration for this application. These six combinations are presented in Table 18. The fifth column in the table shows the required heat transfer coefficient based on the effects of the area magnification factor. The next column shows resulting energy loss for each array for a unit face area as calculated from the previously developed correlations for Nusselt number and friction factor. The final column shows heat transfer coefficient divided by specific fluid friction energy thereby providing a measure of array efficiency.

Table 18 Possible sample application solutions

X/D	*S/D*	*H/D*	αH	*h* (W/m^{2}K)	*E* (W/m^2)	*h/E* (1/K)
1.5	1.5	1	2.70	148.3	29.2	5.1
3	3	1	2.17	183.9	44.4	4.1
5	5	1	2.06	193.9	26.6	7.3
1.5	1.5	4	6.89	58.1	3.1	19.0
3	3	4	3.22	124.2	37.2	3.3
5	5	4	2.44	163.9	60.8	2.7

Due to the effects of the magnification factor, the configuration *X/D* = 1.5, *S/D* = 1.5, *H/D* = 4.0 would be the best solution for this application out of the options considered. By way of comparison, an airfoil-shaped pin-fin array with S/D = 3, H/D = 4, LR = 0.7 and AR = 4.24 met this cooling requirement with an *h/E* = 48.8. This highlights once again the superior performance of the airfoil-shaped pin array.

THIS PAGE INTENTIONALLY LEFT BLANK

APPENDIX G. LIMITS ON AXIAL PITCH

SIZE LIMITATIONS BASED ON KNUDSEN NUMBER

Previously in this work, the minimum heat exchanger hydraulic diameter was limited by concerns regarding particulate contamination. To avoid clogging, minimum passage dimensions were set at 0.3 mm or 300 microns. This determined the dimensions for the optimum practical circular pin case, *S/D* = *X/D* = 5.0, H/D = 0.25 and *X* = 6 mm, resulting in a hydraulic diameter equal to 0.6 mm. In a highly filtered environment where particle sizes could be on the order of 1 micron or smaller, such as in electronic component cooling applications in clean room environments, the heat exchanger could be further reduced in scale to improve performance. However, in such a situation flow under rarefied conditions of a gas could become a limiting factor. This topic will be discussed briefly in this Appendix. The following information on the role of the Knudsen number and the Mach number in determining rarefied flow regimes is taken from Ref. 25. and Ref. 26.

KNUDSEN NUMBER

The Knudsen number, *Kn*, is defined as the ratio of the mean free path of the gas and the flow characteristic diameter. Thus:

$$Kn = \frac{\lambda}{D_h}$$

λ is the mean free path and is defined by:

$$\lambda = \frac{kT}{\sqrt{2}\pi p \sigma_c^2}$$

where k is Boltzmann's constant, 1.380662e-23 J/K

T = temperature (K)

p = pressure (N/m^2) and

σ_c = collision diameter of the gas (m)

For T = 300K, p = 101350 N/m^2 and σ_c taken to be 3 x 10^{-10} m, $\lambda \approx 1e-7$ m

For values of $Kn \leq 0.001$, the continuum hypothesis is considered valid and the flow can be analyzed using Navier-Stokes equations with no-slip boundary conditions. For $Kn > 0.001$, rarefaction effects start to become significant and the flow enters the slip regime. In this range the continuum solution validity begins to breakdown. To remain in the continuum regime in the current study, the minimum hydraulic diameter should be 0.1 mm or 100 microns.

APPLIED LIMIT

As shown above, the minimum hydraulic diameter must be 0.1 mm to avoid rarefaction effects of flow such as slip at the rigid boundaries. In terms of the optimum circular pin-fin array, mentioned above, an axial pitch of 1 mm would yield a hydraulic diameter of 0.1 mm. This reduction in hydraulic diameter from 6 to 1 mm would result in an increase in area density from 65 to 328 cm^2/cm^3.

MACH NUMBER CONSIDERATIONS

In addition to using Knudsen number as a flow regime check, Mach number can be used to further define the region of gas dynamics. From Ref. 26, one accepted boundary for large Reynolds number flows is determined by the ratio $\frac{Ma}{\sqrt{\mathrm{Re}}}$. If this ratio exceeds 0.01, then a slip-flow analysis must be used. Using various inlet velocities, this ratio can be evaluated for several pin-fin configurations to see if the slip-flow regime is encountered. Table 19 shows various circular pin and airfoil-shaped pin arrays each with a hydraulic diameter of 100 microns. In each case, Reynolds number has been maximized until $\frac{Ma}{\sqrt{\mathrm{Re}}} = 0.01$. Using an inlet flow temperature of 300K, the speed of sound is taken as 350 m/s.

The Reynolds numbers shown indicate a limit below which the slip-flow region would be encountered. Note that especially for the circular pin arrays, the limiting Reynolds number is higher than what would normally be considered practical based on

the high average flow velocity. From this table it is clear that Mach number considerations pose no additional limit beyond the Knudsen number limits described above.

Table 19 Flow regime boundaries based on Mach number

Circular Pins ($X/D = S/D = 5.0$)				
H/D	X (m)	Re_{Dh}	$\bar{U}$ (m/s)	$\frac{Ma}{\sqrt{\mathrm{Re}_{Dh}}}$
0.25	1.00e-3	500	80.9	0.01
16	3.20e-5	500	79.2	0.01
Airfoil-shaped Pins (S/D = 2.0, LR = 0.5, AR = 6.2)				
H/D	X (m)	Re_{Dh}	$\bar{U}$ (m/s)	$\frac{Ma}{\sqrt{\mathrm{Re}_{Dh}}}$
0.25	2.70e-3	45	7.0	0.01
16	2.30e-4	45	7.0	0.01

THIS PAGE INTENTIONALLY LEFT BLANK

LIST OF REFERENCES

Ref. 1 Han, J.C., Dutta, S., and Ekkad, S., *Gas Turbine Heat Transfer and Cooling Technology*, Taylor and Francis, 2000.

Ref. 2 Stephens, L.S., Kelly, K.W., Kountouris, D., and McLean, J., "A Pin Fin Microheat Sink for Cooling Macroscale Conformal Surfaces Under the Influence of Thrust and Frictional Forces," *Journal of Microelectromechanical Systems,* Vol. 10, No. 2, pp. 222 – 231, 2001.

Ref. 3 VanFossen, G.J., "Heat Transfer Coefficient for Staggered Arrays of Short Pin Fins," ASME *J. of Engineering for Power*, Vol. 104, pp. 268-274, 1982.

Ref. 4 Sparrow, E.M., Stahl, T.J., and Traub, P., "Heat Transfer Adjacent to the attached end of a Cylinder in Crossflow," *Int. J. of Heat and Mass Transfer*, Vol. 25, pp. 233-242, 1984.

Ref. 5 Metzger, D.E., Berry, R.A., Bronson, J.P., "Developing Heat Transfer in Rectangular Ducts With Staggered Arrays of Short Pin Fins", ASME *J. of Heat Transfer*, Vol. 104, pp. 700-706, 1982.

Ref. 6 Chyu, M.K., "Heat Transfer and Pressure Drop for Short Pin-Fin Arrays with Pin-Endwall Fillet," ASME *J. of Heat Transfer*, Vol. 112, pp. 926-932, 1990.

Ref. 7 Chyu, M.K., and Goldstein, R.J., "Influence of Cylindrical Elements on Local Mass Transfer From a Flat Surface," *Int. J. Heat Mass Transfer*, Vol. 34, pp. 2175-2186, 1991.

Ref. 8 Li, Q., Chen, Z., Flechtner, U., Warnecke, H.-J., "Heat Transfer and Pressure Drop Characteristics in Rectangular Channels with Elliptic Pin Fins," *Int. J. of Heat and Fluid Flow*, Vol 19, pp. 245-250, 1998.

Ref. 9 Jubran, B.A., Hamdan, M.A., Abdualh, R.M., "Enhanced Heat Transfer, Missing Pin, and Optimization for Cylindrical Pin Fin Arrays", ASME *J. of Heat Transfer*, Vol. 115, pp. 576-583, 1993.

Ref. 10 Metzger, D.E., Fan, C.S., and Haley, S. W., "Effects of Pin Shape and Array Orientation on Heat Transfer and Pressure Loss in Pin Fin Arrays," *ASME J. of Engineering for Gas Turbines and Power*, Vol. 106, pp. 252-257, 1984.

Ref. 11 Arora, S.C., and Abdel-Messeh, W., "Pressure Drop and Heat Transfer Characteristics of Circular and Oblong Low Aspect Ratio Pin Fins," AGARD *Conference Proceedings*, pp.4-1-4-15, 1985.

Ref. 12 Chen, Z., Li, Q., Meier, D., and Warnecke, H.J., "Convective heat transfer and pressure loss in rectangular ducts with drop-shaped pin fins," *Heat and Mass transfer*, Vol. 33, pp. 219 - 224, 1997.

Ref. 13 Al Dabagh, A. M., and Andrews, G.E., "Pin-Fin Heat Transfer: Contributions of the Wall and the Pin to the Overall Heat Transfer," ASME Paper No. 92-GT-242, 1992.

Ref. 14 Chyu, M.K., Hsing, Y.C., Shih, T. I.-P., and Natarajan, V., "Heat Transfer Contributions of Pins and Endwall in Pin-Fin Arrays: Effects of Thermal Boundary Condition Modeling," *ASME J. of Turbomachinery*, Vol. 121, pp. 257-263, 1998.

Ref. 15 Shah, R.K., Heikal, M.R., Thonon, B., and Thonon, P., "Progress in the Numerical Analysis of Compact Heat Exchanger Surfaces," *Advances in Heat Transfer*, Vol. 34, Academic Press, pp. 363-443, 2001.

Ref. 16 Donahoo, E.E., Camci, C., Kulkarni, A.K., and Belegundu, A.D., "Determination of Optimal Row Spacing for a Staggered Cross-Pin Array in a Turbine Blade Cooling Passage," *Enhanced Heat Transfer*, Vol. 8, pp. 41-53, 2001.

Ref. 17 "ANSYS Theory Reference," [http://www1.ansys.com/customer/content/documentation/60/ch07s02.html], Sep 2002.

Ref. 18 Incropera, F.P. and DeWitt, D.P., *Introduction to Heat Transfer*, 3rd Ed., Wiley, New York, 1996.

Ref. 19 Kays, W.M. and London, A.L., *Compact Heat Exchangers*, 3rd Ed., McGraw-Hill, New York, 1984.

Ref. 20 Ramthun, D., *An Experimental Study of a pin-fin heat exchanger,* Master's thesis, Naval Postgraduate School, Monterey, CA, June 2003.

Ref. 21 Kline, S.J. and McClintock, F.A., "Describing Uncertainties in Single Sample Experiments," *Mechanical Engineering*, Vol. 75, pp. 3 - 8, 1953.

Ref. 22 White, F.M., *Fluid Mechanics*, 4th Ed., p. 455, McGraw-Hill, 1999.

Ref. 23 Rice, J.G., Schnipke, R.J.,"A Monotone Streamline Upwind Finite Element Method for Convection-Dominated Flows," *Computer Methods in Applied Mechanics and Engineering*, Vol. 48, pp.313-327, 1985.

Ref. 24 Brooks, A.N. and Hughes, T.J.R., "Streamline Upwind/Petro-Galkerin Formulation for Convection Dominated Flows with Particular Emphasis on the Incompressible Navier-Stokes Equations," *Computer Methods in Applied Mechanics and Engineering*, Vol. 32, pp. 199-259, 1982.

Ref. 25 Barber, R.W. and Emerson, D.R., "The influence of Knudsen number on the hydrodynamic development length within parallel plate micro-channels," *Advances in Fluid Mechanics IV,* pp. 207-216, 2002.

Ref. 26 Eckert, E.RG., *Heat and Mass Transfer,* TMH Ed., pp. 272-280, McGraw-Hill, 1974.

INITIAL DISTRIBUTION LIST

1. Defense Technical Information Center
   Ft. Belvoir, Virginia

2. Dudley Knox Library
   Naval Postgraduate School
   Monterey, California

3. Chairman and Associate Professor Ashok Gopinath
   Naval Postgraduate School
   Monterey, California

4. Professor Garth Hobson
   Naval Postgraduate School
   Monterey, California

5. Professor Terry McNelley
   Naval Postgraduate School
   Monterey, California

6. Professor Knox Millsaps
   Naval Postgraduate School
   Monterey, California

7. Professor Raymond Shreeve
   Naval Postgraduate School
   Monterey, California

8. Dr. Aram Kevorkian
   Space and Naval Warfare Systems Command
   San Diego, California

9. Mr. Lew Schmidt
   Naval Air Systems Command
   Patuxent River, Maryland

10. CDR Leonard J. Hamilton, USN
    Naval Postgraduate School
    Monterey, California